國 立 交 通 大 學

電子工程學系 電子研究所碩士班

碩 士 論 文

LTE 隨機存取訊號於可能具有宏大都卜勒位移之

多徑通道中之檢測

Detection of LTE Random Access Signals in Multipath

Channels with Possibly Large Doppler Shifts

研 究 生： 梁晉源

指導教授： 林大衛 博士

中 華 民 國 一〇二 年 十 月

LTE 隨機存取訊號於可能具有宏大都卜勒位移之多徑通道中之檢測

Detection of LTE Random Access Signals in Multipath Channels with Possibly Large Doppler Shifts

研 究 生: 梁晉源　　　　　Student: Chin-Yuan Liang

指導教授: 林大衛　　　　　Advisor: Dr. David W. Lin

國 立 交 通 大 學

電子工程學系　　電子研究所碩士班

碩 士 論 文

中 華 民 國 一○二 年 十 月

LTE 隨機存取訊號於可能具有宏大都卜勒位移之多徑通道中之檢測

研究生：梁晉源　　　　　　　　指導教授：林大衛 博士

國立交通大學

電子工程學系 電子研究所碩士班

摘要

　　本篇論文研究了在於LTE-A的環境下隨機存取偵測的系統，在隨機存取偵測的過程，基地台必須決定是否使用者傳送了隨機存取前置符元(preamble)。

　　在論文中，我們建立了傳送系統模型，而當中我們考慮了符元時間偏移、載波偏移、多徑通道。然後我們把問題制定成多重假說試驗和二元假說試驗，基於多重假說試驗的實行計算複雜度太高，我們著眼於二元假說試驗。我們使用了普遍化相似度比率檢驗(generalized ratio likelihood testing, GLRT)當成偵測的準據來解決問題，而當中我們需要去解出符元時間偏移、載波偏移、多徑通道的最大可能性估計(maximum likelihood estimate, MLE)。在推導中，我們也提出了一個減低普遍化相似度比率檢驗的計算複雜度的近似。

　　在模擬中，在不同載波偏移和多徑通道下，我們驗證了我們提出的普遍化相似度比率檢驗檢測器的效能。對於多徑通道模型，我們考慮了可加性白色高斯雜訊(additive white Gaussian noise, AWGN)和史丹佛大學暫定(Standford University Interim, SUI)的模型。

Detection of LTE Random Access Signals in Multipath Channels with Possibly Large Doppler Shifts

Student: Chin-Yuan Liang   Advisor: Dr. David W. Lin

Department of Electronics Engineering
& Institute of Electronics
National Chiao Tung University

Abstract

The thesis studies the random access detection schemes in LTE-A system. In random access detection procedure, the base station needs to determine whether random access preambles are transmitted by the users.

In this thesis, we first develop transmission system model, in which we consider the symbol timing offset (STO), carrier frequency offset (CFO), and multipath channels. Then we formulate the problem by the multiple hypothesis and binary hypothesis testing. Due to high computational complexity for implementation of multiple hypothesis testing, we focus on the binary hypothesis testing formulation. We use the generalized likelihood testing technique (GLRT) as a detection criterion to solve the problem, in which we need to get the maximum likelihood estimate (MLE) of the STO, CFO, and channel. In the derivation, we also propose an approximation of the GLRT to further reduce the computational complexity.

In the simulation we verify our proposed GLRT detector performance with difference values of CFO and different kind of channel model including AWGN and Standford University Interim (SUI).

誌謝

這篇論文可以完成，首先我要特別感謝我的指導教授林大衛老師，在學術上，林老師的指導常常讓我如醍醐灌醒般的破解研究上的疑難雜症，此外老師樹立的風格典範也是我學習的目標，如果沒有林老師，我的研究所生涯可真不知該何去從，是我生命中的貴人。

此外，還要特別感謝馮智豪老師，因為他的督促，使得我專業知識功力大增，另外，感謝所有Commlab的老師、杭學鳴教授、簡鳳村教授、桑梓賢教授、王聖智教授，因著您們的指導，讓我獲益良多。還有感謝在交大我修過課的所有老師，因著您們慷慨的相授，讓我學習到莫大的知識。

還要感謝，翁郁婷學姐、王柏森學長、洪朝雄學長、林鴻志學長、黃盈叡學長、江清德學長、柯俊言學長、詹曉盈學長還有其他Commlab的所有學長姐，給予我在研究過程上的指導與建議，還要感謝政憲、基峰、維哲、義文、士傑、柔綾、以及所有的成員，因著有你們一起走過，讓我充滿了快樂的回憶。還要特別感謝男鑫，在論文上的事情上受了你不少的幫忙。

要感謝我電資的好友們，跟你們在一起總是充滿了歡樂，讓我有能量去面對研究所的任何事情，感謝說說銘，時常和你一起念書做研究，給了我很多的建議與幫助。要感謝的人太多了，無法一一細數，實感抱歉。

最後我要感謝我生命中的主，若不是祢，我還在黑暗的幽谷，感謝祢每天的陪伴及指引。

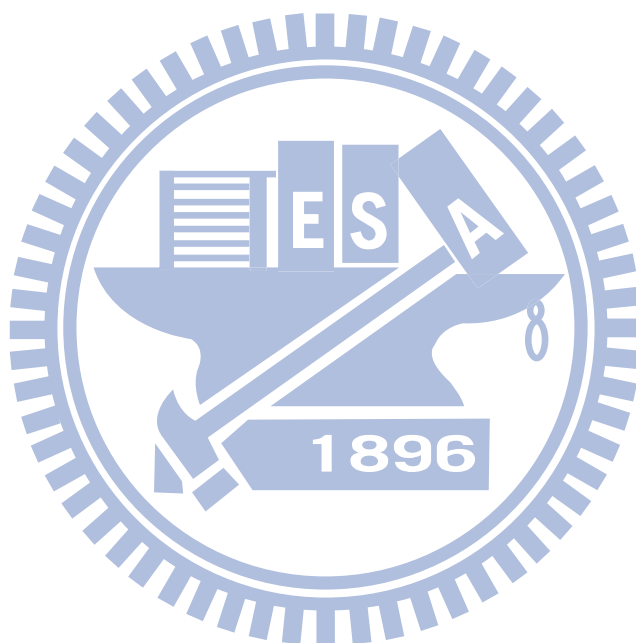在此，將此篇論文獻給所有陪伴我走過這一段歲月、幫助過我的貴人們。

梁晉源

民國一百零二年 於新竹

Contents

Appendix   80

List of Figures

List of Tables

Chapter 1

Introduction

Single-carrier frequency-division multiple access (SC-FDMA) is the chosen multiple access scheme for the uplink in the 3rd Generation Partnership Project (3GPP) Long Term Evolution (LTE), one of the latest standards for cellular mobile communication [1]. The LTE standard is constantly evolving, of which a more recent addition is LTE Advanced (LTE-A), a standard designed to increase the capacity and speed of mobile telephone networks and compliant with IMT-Advanced requirement. LTE Advanced is backwards compatible with LTE and uses the same frequency bands, while LTE is not backwards compatible with the earlier 3G systems. LTE is first introduced in 3GPP release 8. Much of 3GPP release 8 focuses on adopting expected 4G mobile communication technologies, including an all-IP flat networking architecture.

Random access (RA) is generally performed when the user equipment (UE) turns on from sleep mode, performs handoff from one cell to another or when it loses uplink timing synchronization. At the time of random access, it is assumed that the UE is time-synchronized with the eNB (the LTE term for base station) on the downlink. Therefore, when a UE turns on from sleep mode, it first needs to acquire downlink timing synchronization. After acquiring downlink timing synchronization and receiving system information including information on parameters specific to random access, the UE can perform random access by

transmitting RA preamble. The random access process allows the eNB to estimate and, if needed, adjust the UE uplink transmission timing to within a fraction of the cyclic prefix. After the uplink transmission timing of the UE is synchronized, the UE can be scheduled for uplink transmission.

Our study focuses on LTE-A uplink random access signal detection schemes. Based on 3GPP TS.211 release 10 [3], we construct the random access transmission structure and propose a generalized likelihood ratio test (GLRT) detector which considers both a multipath channel model and carrier frequency offset (CFO). The proposed techniques is different from existing receiver schemes [1, 6]. We will discuss the benefits of assuming a multipath channel model and taking CFO into consideration in the thesis.

The following is a summary of each chapter.

- In chapter 2, we introduce the uplink specifications in the LTE release 10 uplink standard based on [1, 2, 3, 4].

- In chapter 3, we introduce the random access specification in the LTE release 10 uplink standard based on [1, 3].

- In chapter 4, we construct the transmission system structure in terms of a mathematical model based on on [3] and introduce the proposed GLRT receiver scheme.

- In chapter 5, we evaluate our proposed GLRT receiver scheme performance and compare to the method in [5].

- In chapter 6, we give the conclusion and indicate some items of potential future work.

Chapter 2

Introduction to LTE-A Release 10 Uplink Specifications

The goal of LTE is to provide a high-data-rate, low-latency and packet-optimized radio access technology supporting flexible bandwidth deployments [1]. In parallel, new network architecture is designed with the goal to support packet-switched traffic with seamless mobility, quality of service and minimal latency.

Some air-interface attributes of the LTE system are summarized in Table 2.1. The system supports flexible bandwidths thanks to SC-FDMA and orthogonal frequency-division multiple access (OFDMA) schemes. In addition to FDD (frequency division duplexing) and TDD (time division duplexing), half duplex FDD is allowed to support low cost UEs. Unlike FDD, in half-duplex FDD operation a UE is not required to transmit and receive at the same time. This avoids the need for a costly duplexer in the UE.

The system is primarily optimized for low speeds up to 15 km/h. However, the system specifications allow mobility support in excess of 350 km/h with some performance degradation. The uplink access based on SC-FDMA promises increased uplink coverage due to low peak-to-average power ratio (PAPR) relative to OFDMA.

As part of LTE-Advanced, several enhancements including support for a larger than 20

3

Table 2.1: LTE System Attributes [1, Table 1.1]

Bandwidth		1.25–20 MHz
Duplexing		FDD, TDD, half-duplex FDD
Mobility		350 km/h
Multiple access	Downlink	OFDMA
	Uplink	SC-FDMA
MIMO	Downlink	2×2, 4×2, 4×4
	Uplink	1×2, 1×4
Peak data rate in 20 MHz	Downlink	173 and 326 Mb/s for 2×2, 4×4 MIMO, respectively
	Uplink	86 Mb/s with 1×2 antenna configuration
Modulation		QPSK, 16-QAM and 64-QAM
Channel coding		Turbo code
Other techniques		Channel sensitive scheduling, link adaptation, power control, ICIC and hybrid ARQ

MHz bandwidth and higher-order MIMO have been standardized to meet the IMT-advanced requirements.

In this chapter, we introduce the physical channel structure in the LTE-A specifications, focusing on the pplink (UL) part especially.

2.1 Channel Bandwidth

The contents of this section are mainly taken from [2].

Requirements are specified for the channel bandwidths as listed in Table 2.2. Figure 2.1 shows the relation between the channel bandwidth ($BW_{Channel}$) and the transmission bandwidth configuration (N_{RB}). The channel edges are defined as the lowest and highest frequencies of the carrier separated by the channel bandwidth, i.e. at $F_C \pm BW_{Channel}/2$.

Table 2.2: Transmission Bandwidth Configuration N_{RB} in E-UTRA Channel Bandwidths [2, Table 5.6-1]

Channel bandwidth $BW_{Channel}$ (MHz)	1.4	3	5	10	15	20
Transmission bandwidth configuration N_{RB}	6	15	25	50	75	100
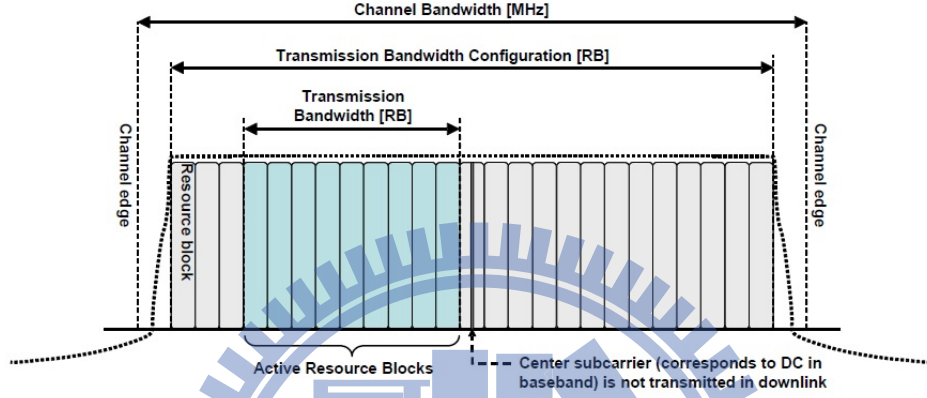
Figure 2.1: Definition of channel bandwidth and transmission bandwidth configuration for one E-UTRA carrier [2, Figure 5.6-1].

2.2 Frame Structure

The contents of this section are mainly taken from [3].

Throughout the specifications, the size of various fields in the time domain is usually expressed in number of time units $T_s = 1/(15000 \times 2048)$ seconds.

Downlink and uplink transmissions are organized into radio frames with $T_f = 307200 \times T_s = 10$ ms duration. Two radio frame structures are supported:

- Type 1, applicable to FDD,

- Type 2, applicable to TDD.

Transmissions in multiple cells can be aggregated where up to four secondary cells can be used
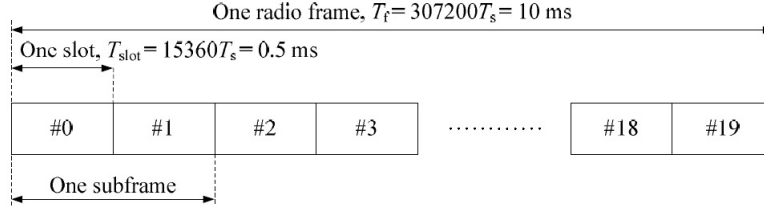
Figure 2.2: Frame structure type 1 [3, Figure 4.1-1].

in addition to the primary cell. Unless otherwise noted, the description in the specifications applies to each of the up to five serving cells. In case of multi-cell aggregation, the UE may assume the same frame structure is used in all the serving cells.

2.2.1 Frame Structure Type 1

Frame structure type 1 is shown in Figure 2.2. It is applicable to both full duplex and half duplex FDD. Each radio frame is $T_f = 307200 \times T_s = 10$ ms long and consists of 20 slots of length $T_{slot} = 15360 \times T_s = 0.5$ ms, numbered from 0 to 19. A subframe is defined as two consecutive slots where subframe i consists of slots $2i$ and $2i + 1$.

For FDD, 10 subframes are available for downlink transmission and 10 subframes are available for uplink transmissions in each 10 ms interval. Uplink and downlink transmissions are separated in the frequency domain. In half-duplex FDD operation, the UE cannot transmit and receive at the same time while there are no such restrictions in full-duplex FDD.

2.2.2 Frame Structure Type 2

Frame structure type 2 is shown in Figure 2.3. It is applicable to TDD. Each radio frame of length $T_f = 307200 \times T_s = 10$ ms consists of two half-frames of length $153600 \times T_s = 5$ ms each. Each half-frame consists of five subframes of length $30720 \cdot T_s = 1$ ms . The

6
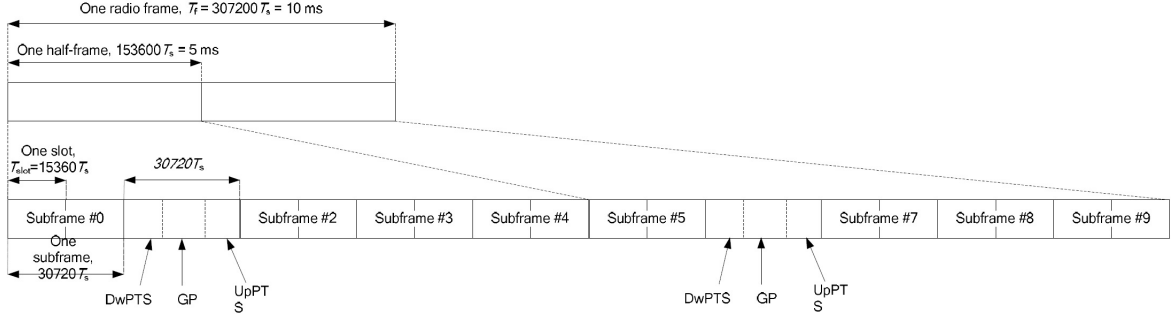
Figure 2.3: Frame structure type 2 (for 5 ms switch-point periodicity) [3, Figure 4.2-1].

supported uplink-downlink configurations are listed in Table 2.3 where, for each subframe in a radio frame, "D" denotes the subframe is reserved for downlink transmissions, "U" denotes the subframe is reserved for uplink transmissions and "S" denotes a special subframe with the three fields DwPTS, GP and UpPTS. The lengths of DwPTS and UpPTS are given in Table 2.4 subject to the total length of DwPTS, GP and UpPTS being equal to $30720 \times T_s = 1$ ms. Each subframe i is defined as two slots, $2i$ and $2i+1$ of length $T_{slot} = 15360 \times T_s = 0.5$ ms in each subframe. Uplink-downlink configurations with both 5 ms and 10 ms downlink-to-uplink switch-point periodicity are supported. In case of 5 ms downlink-to-uplink switch-point periodicity, the special subframe exists in both half-frames. In case of 10 ms downlink-to-uplink switch-point periodicity, the special subframe exists in the first half-frame only. Subframes 0 and 5 and DwPTS are always reserved for downlink transmission. UpPTS and the subframe immediately following the special subframe are always reserved for uplink transmission. In case multiple cells are aggregated, the UE may assume that the guard period of the special subframe in the different cells have an overlap of at least $1456 \cdot T_s$.

Table 2.3: Uplink-Downlink Configurations [3, Table 4.2-2]

Uplink-downlink configuration	Downlink-to-uplink switch-point periodicity	Subframe number									
		0	1	2	3	4	5	6	7	8	9
0	5 ms	D	S	U	U	U	D	S	U	U	U
1	5 ms	D	S	U	U	D	D	S	U	U	D
2	5 ms	D	S	U	D	D	D	S	U	D	D
3	10 ms	D	S	U	U	U	D	D	D	D	D
4	10 ms	D	S	U	U	D	D	D	D	D	D
5	10 ms	D	S	U	D	D	D	D	D	D	D
6	5 ms	D	S	U	U	U	D	S	U	U	D

Table 2.4: Configuration of Special Subframe (Lengths of DwPTS/GP/UpPTS) [3, Table 4.2-1]

Special subframe configuration	Normal cyclic prefix in downlink			Extended cyclic prefix in downlink		
	DwPTS	UpPTS		DwPTS	UpPTS	
		Normal cyclic prefix in uplink	Extended cyclic prefix in uplink		Normal cyclic prefix in uplink	Extended cyclic prefix in uplink
0	$6592 \cdot T_s$			$6592 \cdot T_s$		
1	$19760 \cdot T_s$			$20480 \cdot T_s$		
2	$21952 \cdot T_s$	$2192 \cdot T_s$	$2560 \cdot T_s$	$23040 \cdot T_s$	$2192 \cdot T_s$	$2560 \cdot T_s$
3	$24144 \cdot T_s$			$25600 \cdot T_s$		
4	$26336 \cdot T_s$			$7680 \cdot T_s$		
5	$6592 \cdot T_s$			$20480 \cdot T_s$		
6	$19760 \cdot T_s$			$23040 \cdot T_s$	$4384 \cdot T_s$	$5120 \cdot T_s$
7	$21952 \cdot T_s$	$4384 \cdot T_s$	$5120 \cdot T_s$	$12800 \cdot T_s$		
8	$24144 \cdot T_s$			-	-	-
9	$13168 \cdot T_s$			-	-	-

2.3 Slot Structure and Physical Resources

The contents of this section are mainly taken from [3].

Table 2.5: Resource Block Parameters [3, Table 5.2.3-1]

Configuration	N_{sc}^{RB}	N_{symb}^{UL}
Normal cyclic prefix	12	7
Extended cyclic prefix	12	6

2.3.1 Resource grid

The transmitted signal in each slot is described by one or several resource grids of $N_{RB}^{UL} N_{sc}^{RB}$ subcarriers and N_{symb}^{UL} SC-FDMA symbols. The resource grid is illustrated in Figure 2.4. The quantity N_{NB}^{UL} depends on the uplink transmission bandwidth configured in the cell and shall fulfill

$$N_{RB}^{min,UL} \leqslant N_{RB}^{UL} \leqslant N_{RB}^{max,UL} \tag{2.1}$$

where $N_{RB}^{min,UL} = 6$ and $N_{RB}^{max,UL} = 110$ are the smallest and largest uplink bandwidths, respectively, supported by the current version of the LTE specifications. The set of allowed values for N_{RB}^{UL} is given in [4]. The number of SC-FDMA symbols in a slot depends on the cyclic prefix length configured by the higher layer parameter *UL-CyclicPrefixLength* and is given in Table 2.5.

2.3.2 Resource elements

Each element in the resource grid is called a resource element and is uniquely defined by the index pair (k, l) in a slot where $k = 0, ..., N_{RB}^{UL} N_{sc}^{RB} - 1$ and $l = 0, ..., N_{symb}^{UL}$ are the indices in the frequency and time domains, respectively. Resource elements that are not used for transmission of a physical channel or a physical signal in a slot shall be set to zero.
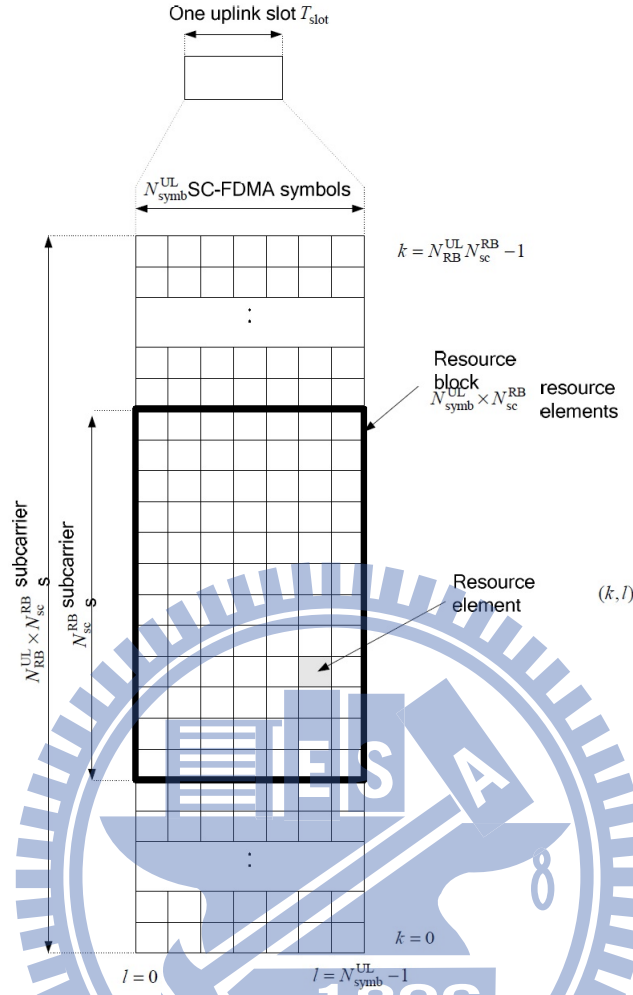
Figure 2.4: Uplink resource grid [3, Figure 5.2.1-1].

2.3.3 Resource blocks

A physical resource block is defined as N_{symb}^{UL} consecutive SC-FDMA symbols in the time domain and N_{sc}^{RB} consecutive subcarriers in the frequency domain, where N_{symb}^{UL} and N_{sc}^{RB} are given by Table 2.5. A physical resource block in the uplink thus consists of $N_{symb}^{UL} \times N_{sc}^{RB}$ resource elements, corresponding to one slot in the time domain and 180 kHz in the frequency domain.

The relation between the physical resource block number n_{PRB} in the frequency domain

and resource elements (k, l) in a slot is given by

$$n_{PRB} = \left\lfloor \frac{k}{N_{sc}^{RB}} \right\rfloor. \tag{2.2}$$

2.4 Zadoff-Chu Sequences

The content of this section are mainly taken from [1]. Zadoff-Chu (ZC) sequences are used extensively in the LTE system, for example, in primary synchronization signals, uplink reference signal, physical uplink shared channel and random access channel [1]. A ZC sequence of length N_{ZC} is defined as

$$x_u(m) = \begin{cases} e^{-j\frac{\pi u m^2}{N_{ZC}}}, & \text{when } N_{ZC} \text{ is even,} \\ e^{-j\frac{\pi u m(m+1)}{N_{ZC}}}, & \text{when } N_{ZC} \text{ is odd,} \end{cases} \tag{2.3}$$

with $m = 0, 1, ..., (N_{ZC} - 1)$, where u the sequence index, which is relatively prime with N_{ZC}.

For a fixed u, the periodic autocorrelation of a ZC sequence is zero for all time shifts other than zero. For different u values, ZC sequences are not orthogonal, but exhibit low crosscorrelation. If the sequence length N_{ZC} is a prime number, then there are $(N_{ZC} - 1)$ different sequences with periodic cross-correlation of $1/\sqrt{N_{ZC}}$ between any two sequences regardless of time shift.

Chapter 3

Physical Random Access Channel (PRACH)

3.1 Time and Frequency Structure

The contents of this section are mainly taken from [3].

The physical layer random access preamble, illustrated in Figure 3.1, consists of a cyclic prefix of length T_{CP} and a sequence part of length T_{SEQ}. The parameter values are listed in Table 3.1 and depend on the frame structure and the random access configuration. Higher layers control the preamble format.

The transmission of a random access preamble, if triggered by the MAC layer, is restricted to certain time and frequency resources. These resources are enumerated in increasing order of the subframe number within the radio frame and the physical resource blocks in the frequency domain such that index 0 correspond to the lowest numbered physical resource block
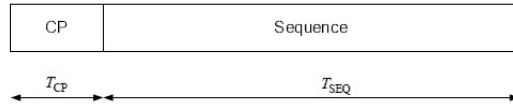
Figure 3.1: Random access preamble format [3, Figure 5.7.1-1].

12

Table 3.1: Random access preamble parameters [3, Table 5.7.1-1].

Preamble format	T_{CP}	T_{SEQ}
0	$3168 \cdot T_s$	$24576 \cdot T_s$
1	$21024 \cdot T_s$	$24576 \cdot T_s$
2	$6240 \cdot T_s$	$2 \cdot 24576 \cdot T_s$
3	$21024 \cdot T_s$	$2 \cdot 24576 \cdot T_s$
4*	$448 \cdot T_s$	$4096 \cdot T_s$

* Frame structure type 2 and special subframe configurations with UpPTS lengths $4384 \cdot T_s$ and $5120 \cdot T_s$ only

and subframe within the radio frame. PRACH resources within the radio frame are indicated by a PRACH resource index, where the indexing is in the order of appearance in Table 3.2 and Table 3.3. For frame structure type 1 with preamble format 0–3, there is at most one random access resource per subframe. Table 3.2 lists the preamble formats according to Table 3.1 and the subframes in which random access preamble transmission is allowed for a given configuration in frame structure type 1. The parameter *prach-ConfigurationIndex* is given by higher layers. The start of the random access preamble shall be aligned with the start of the corresponding uplink subframe at the UE assuming $N_{TA} = 0$, where N_{TA} is defined as timing offset between uplink and downlink radio frames at the UE, expressed in units of T_s. For PRACH configurations 0, 1, 2, 15, 16, 17, 18, 31, 32, 33, 34, 47, 48, 49, 50 and 63 the UE may for handover purposes assume an absolute value of the relative time difference between radio frame i in the current cell and the target cell of less than $153600 \cdot T_s$. The first physical resource block n_{PRB}^{RA} allocated to the PRACH opportunity considered for preamble formats 0, 1, 2 and 3 is defined as $n_{PRB}^{RA} = n_{PRBoffset}^{RA}$, where the parameter *prach-FrequencyOffset* $n_{PRBoffset}^{RA}$, is expressed as a physical resource block number configured by higher layers and fulfilling $0 \leq n_{PRBoffset}^{RA} \leq N_{RB}^{UL} - 6$.

Table 3.2: Frame Structure Type 1 Random Access Configuration for Preamble Formats 0–3 [3, Table 5.7.1-2]

PRACH configuration index	Preamble format	System frame number	Subframe number	PRACH configuration index	Preamble format	System frame number	Subframe number
0	0	Even	1	32	2	Even	1
1	0	Even	4	33	2	Even	4
2	0	Even	7	34	2	Even	7
3	0	Any	1	35	2	Any	1
4	0	Any	4	36	2	Any	4
5	0	Any	7	37	2	Any	7
6	0	Any	1, 6	38	2	Any	1, 6
7	0	Any	2, 7	39	2	Any	2, 7
8	0	Any	3, 8	40	2	Any	3, 8
9	0	Any	1, 4, 7	41	2	Any	1, 4, 7
10	0	Any	2, 5, 8	42	2	Any	2, 5, 8
11	0	Any	3, 6, 9	43	2	Any	3, 6, 9
12	0	Any	0, 2, 4, 6, 8	44	2	Any	0, 2, 4, 6, 8
13	0	Any	1, 3, 5, 7, 9	45	2	Any	1, 3, 5, 7, 9
14	0	Any	0, 1, 2, 3, 4, 5, 6, 7, 8, 9	46	N/A	N/A	N/A
15	0	Even	9	47	2	Even	9
16	1	Even	1	48	3	Even	1
17	1	Even	4	49	3	Even	4
18	1	Even	7	50	3	Even	7
19	1	Any	1	51	3	Any	1
20	1	Any	4	52	3	Any	4
21	1	Any	7	53	3	Any	7
22	1	Any	1, 6	54	3	Any	1, 6
23	1	Any	2 ,7	55	3	Any	2 ,7
24	1	Any	3, 8	56	3	Any	3, 8
25	1	Any	1, 4, 7	57	3	Any	1, 4, 7
26	1	Any	2, 5, 8	58	3	Any	2, 5, 8
27	1	Any	3, 6, 9	59	3	Any	3, 6, 9
28	1	Any	0, 2, 4, 6, 8	60	N/A	N/A	N/A
29	1	Any	1, 3, 5, 7, 9	61	N/A	N/A	N/A
30	N/A	N/A	N/A	62	N/A	N/A	N/A
31	1	Even	9	63	3	Even	9

Table 3.3: Frame Structure Type 2 Random Access Preamble Mapping in Time and Frequency [3, Table 5.7.1-4]

PRACH configuration Index (See Table 3.4)	UL/DL configuration (See Table 2.3)						
	0	1	2	3	4	5	6
0	(0,1,0,2)	(0,1,0,1)	(0,1,0,0)	(0,1,0,2)	(0,1,0,1)	(0,1,0,0)	(0,1,0,2)
1	(0,2,0,2)	(0,2,0,1)	(0,2,0,0)	(0,2,0,2)	(0,2,0,1)	(0,2,0,0)	(0,2,0,2)
2	(0,1,1,2)	(0,1,1,1)	(0,1,1,0)	(0,1,0,1)	(0,1,0,0)	N/A	(0,1,1,1)
3	(0,0,0,2)	(0,0,0,1)	(0,0,0,0)	(0,0,0,2)	(0,0,0,1)	(0,0,0,0)	(0,0,0,2)
4	(0,0,1,2)	(0,0,1,1)	(0,0,1,0)	(0,0,1,1)	(0,0,0,0)	N/A	(0,0,1,1)
5	(0,0,0,1)	(0,0,0,0)	N/A	(0,0,0,0)	N/A	N/A	(0,0,0,1)
6	(0,0,0,2) (0,0,1,2)	(0,0,0,1) (0,0,1,1)	(0,0,0,0) (0,0,1,0)	(0,0,0,1) (0,0,0,2)	(0,0,0,0) (0,0,0,1)	(0,0,0,0) (1,0,0,0)	(0,0,0,2) (0,0,1,1)
7	(0,0,0,1) (0,0,1,1)	(0,0,0,0) (0,0,1,0)	N/A	(0,0,0,0) (0,0,0,2)	N/A	N/A	(0,0,0,1) (0,0,1,0)
8	(0,0,0,0) (0,0,1,0)	N/A	N/A	(0,0,0,0) (0,0,0,1)	N/A	N/A	(0,0,0,0) (0,0,1,1)
9	(0,0,0,1) (0,0,0,2) (0,0,1,2)	(0,0,0,0) (0,0,0,1) (0,0,1,1)	(0,0,0,0) (0,0,1,0) (1,0,0,0)	(0,0,0,0) (0,0,0,1) (0,0,0,2)	(0,0,0,0) (0,0,0,1) (1,0,0,1)	(0,0,0,0) (1,0,0,0) (2,0,0,0)	(0,0,0,1) (0,0,0,2) (0,0,1,1)
10	(0,0,0,0) (0,0,1,0) (0,0,1,1)	(0,0,0,0) (0,0,0,1) (0,0,1,1)	(0,0,0,0) (0,0,1,0) (1,0,1,0)	N/A	(0,0,0,0) (0,0,0,1) (1,0,0,0)	N/A	(0,0,0,0) (0,0,0,2) (0,0,1,0)
11	N/A	(0,0,0,0) (0,0,0,1) (0,0,1,0)	N/A	N/A	N/A	N/A	(0,0,0,1) (0,0,1,0) (0,0,1,1)
12	(0,0,0,1) (0,0,0,2) (0,0,1,1) (0,0,1,2)	(0,0,0,0) (0,0,0,1) (0,0,1,0) (0,0,1,1)	(0,0,0,0) (0,0,1,0) (1,0,0,0) (1,0,1,0)	(0,0,0,0) (0,0,0,1) (0,0,0,2) (1,0,0,2)	(0,0,0,0) (0,0,0,1) (1,0,0,0) (1,0,0,1)	(0,0,0,0) (1,0,0,0) (2,0,0,0) (3,0,0,0)	(0,0,0,1) (0,0,0,2) (0,0,1,0) (0,0,1,1)
13	(0,0,0,0) (0,0,0,2) (0,0,1,0) (0,0,1,2)	N/A	N/A	(0,0,0,0) (0,0,0,1) (0,0,0,2) (1,0,0,1)	N/A	N/A	(0,0,0,0) (0,0,0,1) (0,0,0,2) (0,0,1,1)
14	(0,0,0,0) (0,0,0,1) (0,0,1,0) (0,0,1,1)	N/A	N/A	(0,0,0,0) (0,0,0,1) (0,0,0,2) (1,0,0,0)	N/A	N/A	(0,0,0,0) (0,0,0,2) (0,0,1,0) (0,0,1,1)

15	(0,0,0,0) (0,0,0,1) (0,0,0,2) (0,0,1,1) (0,0,1,2)	(0,0,0,0) (0,0,0,1) (0,0,1,0) (0,0,1,1) (1,0,0,1)	(0,0,0,0) (0,0,1,0) (1,0,0,0) (1,0,1,0) (2,0,0,0)	(0,0,0,0) (0,0,0,1) (0,0,0,2) (1,0,0,1) (1,0,0,2)	(0,0,0,0) (0,0,0,1) (1,0,0,0) (1,0,0,1) (2,0,0,1)	(0,0,0,0) (1,0,0,0) (2,0,0,0) (3,0,0,0) (4,0,0,0)	(0,0,0,0) (0,0,0,1) (0,0,0,2) (0,0,1,0) (0,0,1,1)
16	(0,0,0,1) (0,0,0,2) (0,0,1,0) (0,0,1,1) (0,0,1,2)	(0,0,0,0) (0,0,0,1) (0,0,1,0) (0,0,1,1) (1,0,1,1)	(0,0,0,0) (0,0,1,0) (1,0,0,0) (1,0,1,0) (2,0,1,0)	(0,0,0,0) (0,0,0,1) (0,0,0,2) (1,0,0,0) (1,0,0,2)	(0,0,0,0) (0,0,0,1) (1,0,0,0) (1,0,0,1) (2,0,0,0)	N/A	N/A
17	(0,0,0,0) (0,0,0,1) (0,0,0,2) (0,0,1,0) (0,0,1,2)	(0,0,0,0) (0,0,0,1) (0,0,1,0) (0,0,1,1) (1,0,0,0)	N/A	(0,0,0,0) (0,0,0,1) (0,0,0,2) (1,0,0,0) (1,0,0,1)	N/A	N/A	N/A
18	(0,0,0,0) (0,0,0,1) (0,0,0,2) (0,0,1,0) (0,0,1,1) (0,0,1,2)	(0,0,0,0) (0,0,0,1) (0,0,1,0) (0,0,1,1) (1,0,0,1) (1,0,1,1)	(0,0,0,0) (0,0,1,0) (1,0,0,0) (1,0,1,0) (2,0,0,0) (2,0,1,0)	(0,0,0,0) (0,0,0,1) (0,0,0,2) (1,0,0,0) (1,0,0,1) (1,0,0,2)	(0,0,0,0) (0,0,0,1) (1,0,0,0) (1,0,0,1) (2,0,0,0) (2,0,0,1)	(0,0,0,0) (1,0,0,0) (2,0,0,0) (3,0,0,0) (4,0,0,0) (5,0,0,0)	(0,0,0,0) (0,0,0,1) (0,0,0,2) (0,0,1,0) (0,0,1,1) (1,0,0,2)
19	N/A	(0,0,0,0) (0,0,0,1) (0,0,1,0) (0,0,1,1) (1,0,0,0) (1,0,1,0)	N/A	N/A	N/A	N/A	(0,0,0,0) (0,0,0,1) (0,0,0,2) (0,0,1,0) (0,0,1,1) (1,0,1,1)
20 / 30	(0,1,0,1)	(0,1,0,0)	N/A	(0,1,0,1)	(0,1,0,0)	N/A	(0,1,0,1)
21 / 31	(0,2,0,1)	(0,2,0,0)	N/A	(0,2,0,1)	(0,2,0,0)	N/A	(0,2,0,1)
22 / 32	(0,1,1,1)	(0,1,1,0)	N/A	N/A	N/A	N/A	(0,1,1,0)
23 / 33	(0,0,0,1)	(0,0,0,0)	N/A	(0,0,0,1)	(0,0,0,0)	N/A	(0,0,0,1)
24 / 34	(0,0,1,1)	(0,0,1,0)	N/A	N/A	N/A	N/A	(0,0,1,0)
25 / 35	(0,0,0,1) (0,0,1,1)	(0,0,0,0) (0,0,1,0)	N/A	(0,0,0,1) (1,0,0,1)	(0,0,0,0) (1,0,0,0)	N/A	(0,0,0,1) (0,0,1,0)
26 / 36	(0,0,0,1) (0,0,1,1) (1,0,0,1)	(0,0,0,0) (0,0,1,0) (1,0,0,0)	N/A	(0,0,0,1) (1,0,0,1) (2,0,0,1)	(0,0,0,0) (1,0,0,0) (2,0,0,0)	N/A	(0,0,0,1) (0,0,1,0) (1,0,0,1)
27 / 37	(0,0,0,1) (0,0,1,1) (1,0,0,1) (1,0,1,1)	(0,0,0,0) (0,0,1,0) (1,0,0,0) (1,0,1,0)	N/A	(0,0,0,1) (1,0,0,1) (2,0,0,1) (3,0,0,1)	(0,0,0,0) (1,0,0,0) (2,0,0,0) (3,0,0,0)	N/A	(0,0,0,1) (0,0,1,0) (1,0,0,1) (1,0,1,0)

28 / 38	(0,0,0,1) (0,0,1,1) (1,0,0,1) (1,0,1,1) (2,0,0,1)	(0,0,0,0) (0,0,1,0) (1,0,0,0) (1,0,1,0) (2,0,0,0)	N/A	(0,0,0,1) (1,0,0,1) (2,0,0,1) (3,0,0,1) (4,0,0,1)	(0,0,0,0) (1,0,0,0) (2,0,0,0) (3,0,0,0) (4,0,0,0)	N/A	(0,0,0,1) (0,0,1,0) (1,0,0,1) (1,0,1,0) (2,0,0,1)
29 / 39	(0,0,0,1) (0,0,1,1) (1,0,0,1) (1,0,1,1) (2,0,0,1) (2,0,1,1)	(0,0,0,0) (0,0,1,0) (1,0,0,0) (1,0,1,0) (2,0,0,0) (2,0,1,0)	N/A	(0,0,0,1) (1,0,0,1) (2,0,0,1) (3,0,0,1) (4,0,0,1) (5,0,0,1)	(0,0,0,0) (1,0,0,0) (2,0,0,0) (3,0,0,0) (4,0,0,0) (5,0,0,0)	N/A	(0,0,0,1) (0,0,1,0) (1,0,0,1) (1,0,1,0) (2,0,0,1) (2,0,1,0)
40	(0,1,0,0)	N/A	N/A	(0,1,0,0)	N/A	N/A	(0,1,0,0)
41	(0,2,0,0)	N/A	N/A	(0,2,0,0)	N/A	N/A	(0,2,0,0)
42	(0,1,1,0)	N/A	N/A	N/A	N/A	N/A	N/A
43	(0,0,0,0)	N/A	N/A	(0,0,0,0)	N/A	N/A	(0,0,0,0)
44	(0,0,1,0)	N/A	N/A	N/A	N/A	N/A	N/A
45	(0,0,0,0) (0,0,1,0)	N/A	N/A	(0,0,0,0) (1,0,0,0)	N/A	N/A	(0,0,0,0) (1,0,0,0)
46	(0,0,0,0) (0,0,1,0) (1,0,0,0)	N/A	N/A	(0,0,0,0) (1,0,0,0) (2,0,0,0)	N/A	N/A	(0,0,0,0) (1,0,0,0) (2,0,0,0)
47	(0,0,0,0) (0,0,1,0) (1,0,0,0) (1,0,1,0)	N/A	N/A	(0,0,0,0) (1,0,0,0) (2,0,0,0) (3,0,0,0)	N/A	N/A	(0,0,0,0) (1,0,0,0) (2,0,0,0) (3,0,0,0)
48	(0,1,0,*)	(0,1,0,*)	(0,1,0,*)	(0,1,0,*)	(0,1,0,*)	(0,1,0,*)	(0,1,0,*)
49	(0,2,0,*)	(0,2,0,*)	(0,2,0,*)	(0,2,0,*)	(0,2,0,*)	(0,2,0,*)	(0,2,0,*)
50	(0,1,1,*)	(0,1,1,*)	(0,1,1,*)	N/A	N/A	N/A	(0,1,1,*)
51	(0,0,0,*)	(0,0,0,*)	(0,0,0,*)	(0,0,0,*)	(0,0,0,*)	(0,0,0,*)	(0,0,0,*)
52	(0,0,1,*)	(0,0,1,*)	(0,0,1,*)	N/A	N/A	N/A	(0,0,1,*)
53	(0,0,0,*) (0,0,1,*)	(0,0,0,*) (0,0,1,*)	(0,0,0,*) (0,0,1,*)	(0,0,0,*) (1,0,0,*)	(0,0,0,*) (1,0,0,*)	(0,0,0,*) (1,0,0,*)	(0,0,0,*) (0,0,1,*)
54	(0,0,0,*) (0,0,1,*) (1,0,0,*)	(0,0,0,*) (0,0,1,*) (1,0,0,*)	(0,0,0,*) (0,0,1,*) (1,0,0,*)	(0,0,0,*) (1,0,0,*) (2,0,0,*)	(0,0,0,*) (1,0,0,*) (2,0,0,*)	(0,0,0,*) (1,0,0,*) (2,0,0,*)	(0,0,0,*) (0,0,1,*) (1,0,0,*)
55	(0,0,0,*) (0,0,1,*) (1,0,0,*) (1,0,1,*)	(0,0,0,*) (0,0,1,*) (1,0,0,*) (1,0,1,*)	(0,0,0,*) (0,0,1,*) (1,0,0,*) (1,0,1,*)	(0,0,0,*) (1,0,0,*) (2,0,0,*) (3,0,0,*)	(0,0,0,*) (1,0,0,*) (2,0,0,*) (3,0,0,*)	(0,0,0,*) (1,0,0,*) (2,0,0,*) (3,0,0,*)	(0,0,0,*) (0,0,1,*) (1,0,0,*) (1,0,1,*)

56	(0,0,0,*) (0,0,1,*) (1,0,0,*) (1,0,1,*) (2,0,0,*)	(0,0,0,*) (0,0,1,*) (1,0,0,*) (1,0,1,*) (2,0,0,*)	(0,0,0,*) (0,0,1,*) (1,0,0,*) (1,0,1,*) (2,0,0,*)	(0,0,0,*) (1,0,0,*) (2,0,0,*) (3,0,0,*) (4,0,0,*)	(0,0,0,*) (1,0,0,*) (2,0,0,*) (3,0,0,*) (4,0,0,*)	(0,0,0,*) (1,0,0,*) (2,0,0,*) (3,0,0,*) (4,0,0,*)	(0,0,0,*) (0,0,1,*) (1,0,0,*) (1,0,1,*) (2,0,0,*)
57	(0,0,0,*) (0,0,1,*) (1,0,0,*) (1,0,1,*) (2,0,0,*) (2,0,1,*)	(0,0,0,*) (0,0,1,*) (1,0,0,*) (1,0,1,*) (2,0,0,*) (2,0,1,*)	(0,0,0,*) (0,0,1,*) (1,0,0,*) (1,0,1,*) (2,0,0,*) (2,0,1,*)	(0,0,0,*) (1,0,0,*) (2,0,0,*) (3,0,0,*) (4,0,0,*) (5,0,0,*)	(0,0,0,*) (1,0,0,*) (2,0,0,*) (3,0,0,*) (4,0,0,*) (5,0,0,*)	(0,0,0,*) (1,0,0,*) (2,0,0,*) (3,0,0,*) (4,0,0,*) (5,0,0,*)	(0,0,0,*) (0,0,1,*) (1,0,0,*) (1,0,1,*) (2,0,0,*) (2,0,1,*)
58	N/A	N/A	N/A	N/A	N/A	N/A	N/A
59	N/A	N/A	N/A	N/A	N/A	N/A	N/A
60	N/A	N/A	N/A	N/A	N/A	N/A	N/A
61	N/A	N/A	N/A	N/A	N/A	N/A	N/A
62	N/A	N/A	N/A	N/A	N/A	N/A	N/A
63	N/A	N/A	N/A	N/A	N/A	N/A	N/A

For frame structure type 2 with preamble formats 0-4, there might be multiple random access resources in an UL subframe (or UpPTS for preamble format 4) depending on the UL/DL configuration (see Table 2.3). Table 3.4 lists PRACH configurations allowed for frame structure type 2 where the configuration index corresponds to a certain combination of preamble format, PRACH density value, D_{RA} and version index, r_{RA}. The parameter *prach-ConfigurationIndex* is given by higher layers. For frame structure type 2 with PRACH configuration 0, 1, 2, 20, 21, 22, 30, 31, 32, 40, 41, 42, 48, 49, 50, or with PRACH configuration 51, 53, 54, 55, 56, 57 in UL/DL configuration 3, 4, 5, the UE may for handover purposes assume an absolute value of the relative time difference between radio frame i in the current cell and the target cell is less than $153600 \cdot T_s$.

Table 3.3 lists the mapping to physical resources for the different random access opportunities needed for a certain PRACH density value, D_{RA}. Each quadruple of the format

Table 3.4: Frame Structure Type 2 Random Access Configurations for Preamble Formats 0-4 [3, Table 5.7.1-3].

PRACH configuration Index	Preamble Format	Density Per 10 ms D_{RA}	Version r_{RA}	PRACH configuration Index	Preamble Format	Density Per 10 ms D_{RA}	Version r_{RA}
0	0	0.5	0	32	2	0.5	2
1	0	0.5	1	33	2	1	0
2	0	0.5	2	34	2	1	1
3	0	1	0	35	2	2	0
4	0	1	1	36	2	3	0
5	0	1	2	37	2	4	0
6	0	2	0	38	2	5	0
7	0	2	1	39	2	6	0
8	0	2	2	40	3	0.5	0
9	0	3	0	41	3	0.5	1
10	0	3	1	42	3	0.5	2
11	0	3	2	43	3	1	0
12	0	4	0	44	3	1	1
13	0	4	1	45	3	2	0
14	0	4	2	46	3	3	0
15	0	5	0	47	3	4	0
16	0	5	1	48	4	0.5	0
17	0	5	2	49	4	0.5	1
18	0	6	0	50	4	0.5	2
19	0	6	1	51	4	1	0
20	1	0.5	0	52	4	1	1
21	1	0.5	1	53	4	2	0
22	1	0.5	2	54	4	3	0
23	1	1	0	55	4	4	0
24	1	1	1	56	4	5	0
25	1	2	0	57	4	6	0
26	1	3	0	58	N/A	N/A	N/A
27	1	4	0	59	N/A	N/A	N/A
28	1	5	0	60	N/A	N/A	N/A
29	1	6	0	61	N/A	N/A	N/A
30	2	0.5	0	62	N/A	N/A	N/A
31	2	0.5	1	63	N/A	N/A	N/A

$(f_{RA}, t_{RA}^{(0)}, t_{RA}^{(1)}, t_{RA}^{(2)})$ indicates the location of a specific random access resource, where f_{RA} is a frequency resource index within the considered time instance, $t_{RA}^{(0)} = 0, 1, 2$ indicates whether the resource is reoccurring in all radio frames, in even radio frames, or in odd radio frames, respectively, $t_{RA}^{(1)} = 0, 1$ indicates whether the random access resource is located in first half frame or in second half frame, respectively, and where $t_{RA}^{(2)}$ is the uplink subframe number where the preamble starts, counting from 0 at the first uplink subframe between 2 consecutive downlink-to-uplink switch points, with the exception of preamble format 4 where $t_{RA}^{(2)}$ is denoted as (*). The start of the random access preamble formats 0–3 shall be aligned with the start of the corresponding uplink subframe at the UE assuming $N_{TA} = 0$ and the random access preamble format 4 shall start $4832 \cdot T_s$ before the end of the UpPTS at the UE, where the UpPTS is referenced to the UE's uplink frame timing assuming $N_{TA} = 0$.

The random access opportunities for each PRACH configuration shall be allocated in time first and then in frequency if and only if time multiplexing is not sufficient to hold all opportunities of a PRACH configuration needed for a certain density value D_{RA} without overlap in time. For preamble format 0–3, the frequency multiplexing shall be done according to

$$n_{PRB}^{RA} = \begin{cases} n_{PRBoffset}^{RA} + 6 \left\lfloor \frac{f_{RA}}{2} \right\rfloor, & \text{if } f_{RA} \bmod 2 = 0, \\ N_{RB}^{UL} - 6 - n_{PRBoffset}^{RA} - 6 \left\lfloor \frac{f_{RA}}{2} \right\rfloor, & \text{otherwise,} \end{cases} \quad (3.1)$$

where N_{RB}^{UL} is the number of uplink resource blocks, n_{PRB}^{RA} is the first physical resource block allocated to the PRACH opportunity considered and where the parameter *prach-Frequencyoffset*, $n_{PRBoffset}^{RA}$, is the first physical resource block available for PRACH expressed as a physical resource block number configured by higher layers and fulfilling $0 \le n_{PRBoffset}^{RA} \le N_{RB}^{UL} - 6$.

For preamble format 4, the frequency multiplexing shall be done according to

$$n_{PRB}^{RA} = \begin{cases} 6f_{RA}, & \text{if } \left((n_f \bmod 2) \times (2 - N_{SP}) + t_{RA}^{(1))} \right) \bmod 2 = 0, \\ N_{RB}^{UL} - 6(f_{RA} + 1), & \text{otherwise,} \end{cases} \quad (3.2)$$

where n_f is the system frame number and where N_{SP} is the number of DL to UL switch points

within the radio frame. Each random access preamble occupies a bandwidth corresponding to 6 consecutive resource blocks for both frame structures.

3.2 Preamble Sequence Generation

The contents of this section are mainly taken from [3].

The random access preambles are generated from Zadoff-Chu sequences with zero correlation zone, from one or several root Zadoff-Chu sequences. The network configures the set of preamble sequences the UE is allowed to use. There are 64 preambles available in each cell. The set of 64 preamble sequences in a cell is found by including first, in the order of increasing cyclic shift, all the available cyclic shifts of a root Zadoff-Chu sequence with the logical index *RACH_ROOT_SEQUENCE*, where *RACH_ROOT_SEQUENCE* is broadcasted as part of the system information. Additional preamble sequences, in case 64 preambles cannot be generated from a single root Zadoff-Chu sequence, are obtained from the root sequences with consecutive logical indexes until all the 64 sequences are found. The logical root sequence order is cyclic: the logical index 0 is consecutive to 837. The relation between a logical root sequence index and physical root sequence index u is given by Tables 3.5 and 3.6 for preamble formats 0–3 and 4, respectively.

Table 3.5: Root Zadoff-Chu Sequence Order for Preamble Formats 0–3 [3, Table 5.7.2-4]

Logical root sequence number	Physical root sequence number u (in increasing order of the corresponding logical sequence number)
0–23	129, 710, 140, 699, 120, 719, 210, 629, 168, 671, 84, 755, 105, 734, 93, 746, 70, 769, 60, 779, 2, 837, 1, 838
24–29	56, 783, 112, 727, 148, 691
30–35	80, 759, 42, 797, 40, 799
36–41	35, 804, 73, 766, 146, 693
42–51	31, 808, 28, 811, 30, 809, 27, 812, 29, 810
52–63	24, 815, 48, 791, 68, 771, 74, 765, 178, 661, 136, 703
64–75	86, 753, 78, 761, 43, 796, 39, 800, 20, 819, 21, 818

76–89	95, 744, 202, 637, 190, 649, 181, 658, 137, 702, 125, 714, 151, 688
90–115	217, 622, 128, 711, 142, 697, 122, 717, 203, 636, 118, 721, 110, 729, 89, 750, 103, 736, 61, 778, 55, 784, 15, 824, 14, 825
116–135	12, 827, 23, 816, 34, 805, 37, 802, 46, 793, 207, 632, 179, 660, 145, 694, 130, 709, 223, 616
136–167	228, 611, 227, 612, 132, 707, 133, 706, 143, 696, 135, 704, 161, 678, 201, 638, 173, 666, 106, 733, 83, 756, 91, 748, 66, 773, 53, 786, 10, 829, 9, 830
168–203	7, 832, 8, 831, 16, 823, 47, 792, 64, 775, 57, 782, 104, 735, 101, 738, 108, 731, 208, 631, 184, 655, 197, 642, 191, 648, 121, 718, 141, 698, 149, 690, 216, 623, 218, 621
204–263	152, 687, 144, 695, 134, 705, 138, 701, 199, 640, 162, 677, 176, 663, 119, 720, 158, 681, 164, 675, 174, 665, 171, 668, 170, 669, 87, 752, 169, 670, 88, 751, 107, 732, 81, 758, 82, 757, 100, 739, 98, 741, 71, 768, 59, 780, 65, 774, 50, 789, 49, 790, 26, 813, 17, 822, 13, 826, 6, 833
264–327	5, 834, 33, 806, 51, 788, 75, 764, 99, 740, 96, 743, 97, 742, 166, 673, 172, 667, 175, 664, 187, 652, 163, 676, 185, 654, 200, 639, 114, 725, 189, 650, 115, 724, 194, 645, 195, 644, 192, 647, 182, 657, 157, 682, 156, 683, 211, 628, 154, 685, 123, 716, 139, 700, 212, 627, 153, 686, 213, 626, 215, 624, 150, 689
328–383	225, 614, 224, 615, 221, 618, 220, 619, 127, 712, 147, 692, 124, 715, 193, 646, 205, 634, 206, 633, 116, 723, 160, 679, 186, 653, 167, 672, 79, 760, 85, 754, 77, 762, 92, 747, 58, 781, 62, 777, 69, 770, 54, 785, 36, 803, 32, 807, 25, 814, 18, 821, 11, 828, 4, 835
384–455	3, 836, 19, 820, 22, 817, 41, 798, 38, 801, 44, 795, 52, 787, 45, 794, 63, 776, 67, 772, 72, 767, 76, 763, 94, 745, 102, 737, 90, 749, 109, 730, 165, 674, 111, 728, 209, 630, 204, 635, 117, 722, 188, 651, 159, 680, 198, 641, 113, 726, 183, 656, 180, 659, 177, 662, 196, 643, 155, 684, 214, 625, 126, 713, 131, 708, 219, 620, 222, 617, 226, 613
456–513	230, 609, 232, 607, 262, 577, 252, 587, 418, 421, 416, 423, 413, 426, 411, 428, 376, 463, 395, 444, 283, 556, 285, 554, 379, 460, 390, 449, 363, 476, 384, 455, 388, 451, 386, 453, 361, 478, 387, 452, 360, 479, 310, 529, 354, 485, 328, 511, 315, 524, 337, 502, 349, 490, 335, 504, 324, 515
514–561	323, 516, 320, 519, 334, 505, 359, 480, 295, 544, 385, 454, 292, 547, 291, 548, 381, 458, 399, 440, 380, 459, 397, 442, 369, 470, 377, 462, 410, 429, 407, 432, 281, 558, 414, 425, 247, 592, 277, 562, 271, 568, 272, 567, 264, 575, 259, 580
562–629	237, 602, 239, 600, 244, 595, 243, 596, 275, 564, 278, 561, 250, 589, 246, 593, 417, 422, 248, 591, 394, 445, 393, 446, 370, 469, 365, 474, 300, 539, 299, 540, 364, 475, 362, 477, 298, 541, 312, 527, 313, 526, 314, 525, 353, 486, 352, 487, 343, 496, 327, 512, 350, 489, 326, 513, 319, 520, 332, 507, 333, 506, 348, 491, 347, 492, 322, 517

630–659	330, 509, 338, 501, 341, 498, 340, 499, 342, 497, 301, 538, 366, 473, 401, 438, 371, 468, 408, 431, 375, 464, 249, 590, 269, 570, 238, 601, 234, 605
660–707	257, 582, 273, 566, 255, 584, 254, 585, 245, 594, 251, 588, 412, 427, 372, 467, 282, 557, 403, 436, 396, 443, 392, 447, 391, 448, 382, 457, 389, 450, 294, 545, 297, 542, 311, 528, 344, 495, 345, 494, 318, 521, 331, 508, 325, 514, 321, 518
708–729	346, 493, 339, 500, 351, 488, 306, 533, 289, 550, 400, 439, 378, 461, 374, 465, 415, 424, 270, 569, 241, 598
730–751	231, 608, 260, 579, 268, 571, 276, 563, 409, 430, 398, 441, 290, 549, 304, 535, 308, 531, 358, 481, 316, 523
752–765	293, 546, 288, 551, 284, 555, 368, 471, 253, 586, 256, 583, 263, 576
766–777	242, 597, 274, 565, 402, 437, 383, 456, 357, 482, 329, 510
778–789	317, 522, 307, 532, 286, 553, 287, 552, 266, 573, 261, 578
790–795	236, 603, 303, 536, 356, 483
796–803	355, 484, 405, 434, 404, 435, 406, 433
804–809	235, 604, 267, 572, 302, 537
810–815	309, 530, 265, 574, 233, 606
816–819	367, 472, 296, 543
820–837	336, 503, 305, 534, 373, 466, 280, 559, 279, 560, 419, 420, 240, 599, 258, 581, 229, 610

Table 3.6: Root Zadoff-Chu Sequence Order for Preamble Format 4 [3, Table 5.7.2-5]

Logical root sequence number	Physical root sequence number u (in increasing order of the corresponding logical sequence number)																			
0–19	1	138	2	137	3	136	4	135	5	134	6	133	7	132	8	131	9	130	10	129
20–39	11	128	12	127	13	126	14	125	15	124	16	123	17	122	18	121	19	120	20	119
40–59	21	118	22	117	23	116	24	115	25	114	26	113	27	112	28	111	29	110	30	109
60–79	31	108	32	107	33	106	34	105	35	104	36	103	37	102	38	101	39	100	40	99
80–99	41	98	42	97	43	96	44	95	45	94	46	93	47	92	48	91	49	90	50	89
100–119	51	88	52	87	53	86	54	85	55	84	56	83	57	82	58	81	59	80	60	79
120–137	61	78	62	77	63	76	64	75	65	74	66	73	67	72	68	71	69	70	-	-
138–837	N/A																			

Table 3.7: Random Access Preamble Sequence Length [3, Table 5.7.2-1]

Preamble format	N_{ZC}
0–3	839
4	139

The uth root Zadoff-Chu sequence is defined by

$$x_u(n) = e^{-j\frac{\pi un(n+1))}{N_{ZC}}}, \quad 0 \le n \le N_{ZC} - 1,$$ (3.3)

where the length N_{ZC} of the Zadoff-Chu sequence is given by Table 3.7. From the uth root Zadoff-Chu sequence, random access preambles with zero correlation zones of length $N_{CS} - 1$are defined by cyclic shifts according to

$$x_{u,v}(n) = x_u\left((n + C_v) \bmod N_{ZC}\right)$$ (3.4)

where the cyclic shift is given by

$$C_v = \begin{cases} vN_{CS}, & v = 0, 1, ..., \lfloor N_{ZC}/N_{CS} \rfloor - 1, N_{CS} \ne 0, \\ 0, & N_{CS} = 0, \\ d_{start} \lfloor v/n_{shift}^{RA} \rfloor + \left(v \bmod n_{shift}^{RA}\right) N_{CS}, & v = 0, 1, ..., n_{shift}^{RA} n_{group}^{RA} + \bar{n}_{shift}^{RA} - 1, \end{cases}$$ (3.5)

where the first two lines in the equation are for unrestricted sets and the last line is for restricted sets, and N_{CS} is given by Tables 3.8 and 3.9 for preamble formats 0–3 and 4, respectively, where the parameter *zeroCorrelationZoneConfig* is provided by higher layers. The parameter *High-speed-flag* provided by higher layers determines if unrestricted set or restricted set shall be used.

The variable d_u is the cyclic shift corresponding to a Doppler shift of magnitude $1/T_{SEQ}$ and is given by

$$d_u = \begin{cases} p, & 0 \le p < N_{ZC}/2, \\ N_{ZC} - p, & \text{otherwise,} \end{cases}$$ (3.6)

where p is the smallest non-negative integer that fulfils $(pu) \bmod N_{ZC} = 1$. The parameters for restricted sets of cyclic shifts depend on d_u. For $N_{CS} \le d_u < N_{ZC}/3$, the parameters are

Table 3.8: N_{CS} for Preamble Generation (Preamble Formats 0–3) [3, Table 5.7.2-2]

$zeroCorrelationZoneConfig$	N_{CS} value	
	Unrestricted set	Restricted set
0	0	15
1	13	18
2	15	22
3	18	26
4	22	32
5	26	38
6	32	46
7	38	55
8	46	68
9	59	82
10	76	100
11	93	128
12	119	158
13	167	202
14	279	237
15	419	-

given by

$$
\begin{aligned}
n_{shift}^{RA} &= \lfloor d_u/N_{CS} \rfloor, \\
d_{start} &= 2d_u + n_{shift}^{RA} N_{CS}, \\
n_{group}^{RA} &= \lfloor N_{ZC}/d_{start} \rfloor, \\
\bar{n}_{shift}^{RA} &= \max\left(\lfloor \left(N_{ZC} - 2d_u - n_{group}^{RA} d_{start}\right)/N_{CS} \rfloor, 0\right).
\end{aligned}
\tag{3.7}
$$

For $N_{ZC}/3 \le d_u \le (N_{ZC} - N_{CS})/2$, the parameters are given by

$$
\begin{aligned}
n_{shift}^{RA} &= \lfloor (N_{CS} - 2d_u)/N_{CS} \rfloor, \\
d_{start} &= N_{ZC} - 2d_u + n_{shift}^{RA} N_{CS},, \\
n_{group}^{RA} &= \lfloor d_u/d_{start} \rfloor, \\
\bar{n}_{shift}^{RA} &= \min\left(\max\left(\lfloor \left(d_u - n_{group}^{RA} d_{start}\right)/N_{CS} \rfloor, 0\right), n_{shift}^{RA}\right).
\end{aligned}
\tag{3.8}
$$

For all other values of d_u, there are no cyclic shifts in the restricted set.

Table 3.9: N_{CS} for Preamble Generation (Preamble Format 4) [3, Table 5.7.2-3]

$zeroCorrelationZoneConfig$	N_{CS} value
0	2
1	4
2	6
3	8
4	10
5	12
6	15
7	N/A
8	N/A
9	N/A
10	N/A
11	N/A
12	N/A
13	N/A
14	N/A
15	N/A

3.3 Baseband Signal Generation

The contents of this section are mainly taken from [3].

The time-continuous random access signal $s(t)$ is defined by

$$s(t) = \beta_{PRACH} \sum_{k=0}^{N_{ZC}-1} \sum_{n=0}^{N_{ZC}-1} x_{u,v}(n) \cdot e^{-j\frac{2\pi nk}{N_{ZC}}} \cdot e^{j2\pi(k+\varphi+K(k_0+1/2))\Delta f_{RA}(t-T_{CP})} \quad (3.9)$$

where $0 \leq t < T_{SEQ} + T_{CP}$, β_{PRACH} is an amplitude scaling factor, and $k_0 = n_{PRB}^{RA} N_{sc}^{RB} - N_{RB}^{UL} N_{sc}^{RB}/2$. The location in the frequency domain is controlled by the parameter n_{PRB}^{RA} as derived from section 3.1. The factor $K = \Delta f / \Delta f_{RA}$ accounts for the difference in subcarrier spacing between the random access preamble and uplink data transmission. The variable Δf_{RA}, the subcarrier spacing for the random access preamble, and the variable φ, a fixed offset determining the frequency-domain location of the random access preamble within the physical resource blocks, are both given by Table 3.10.

Table 3.10: Random Access Baseband Parameters [3, Table 5.7.3-1]

Preamble format	Δf_{RA}	φ
0–3	1250 Hz	7
4	7500 Hz	2

Chapter 4

Random Access Signals Detection for LTE-A

In this chapter, first we will introduce the system structure and the problem formulation, and then we will describe the GLRT detector considered in the thesis.

4.1　System Model

The transmission structure is shown in Figure 4.1. Because the discrete Fourier transform (DFT) precoding of a ZC sequence converts to another ZC sequence with a different root index [1], unlike the transmission of user signals in SC-FDMA, DFT precoding of the random access preamble is unneeded. Therefore, we adopt a direct mapping scheme where DFT-precoding is removed. Random access transmission uses six consecutive resource blocks, which equals to 1.08 MHz, and is transmitted over B available bandwidth. That is, the system totally uses $N = B/\Delta f_{RA}$ subcarriers for transmission. For UE k, N_{ZC} points of Zadoff-Chu sequence with root index u_k and cyclic shift C_{v_k} denoted by $\mathbf{x}_{u_k,v_k} \triangleq [x_{u_k,v_k}(0)\ x_{u_k,v_k}(1) \cdots x_{u_k,v_k}(N_{ZC} - 1)]^T$ are directly mapped to the input of the N–point IDFT where the location in the frequency domain is defined in section 3.3. Let $\mathbf{c}_k$ denote the input of the IDFT as
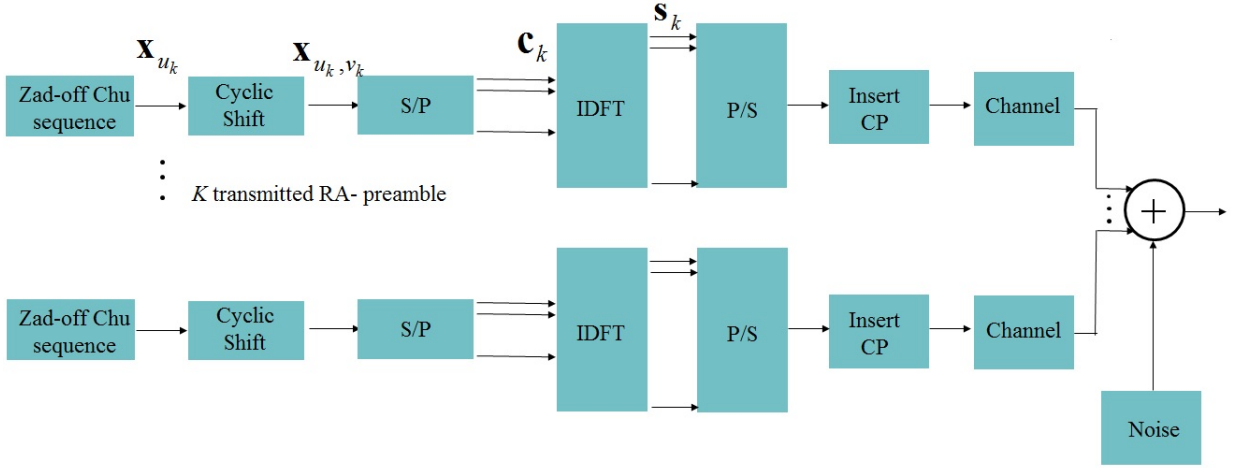
Figure 4.1: Transmission system structure.

$$\mathbf{c}_k\left(i\right) = \begin{cases} \mathbf{x}_{u_k,v_k}\left(i - \phi\right), & \phi \le i \le \phi + N_{ZC} - 1, \\ 0, & \text{otherwsie}, \end{cases} \tag{4.1}$$

where $0 \le i \le N-1$ and $\phi = \varphi + \frac{\Delta f}{\Delta f_{RA}}\left(k_0 + \frac{1}{2}\right)$ denotes the starting position in the frequency domain.

A transmitted time-domain RA-preamble without CP $\mathbf{s}_k$ is IDFT of $\mathbf{c}_k$ given as

$$\mathbf{s}_k \triangleq \left[s_k(0)\ s_k(1)\cdots s_k(N-1)\right]^T = \frac{1}{\sqrt{N}}\mathbf{F}^H\mathbf{c}_k \tag{4.2}$$

where $\mathbf{F} \in \mathbb{C}^{N \times N}$ is the normalized DFT matrix defined as

$$\mathbf{F} \triangleq \frac{1}{\sqrt{N}} \begin{bmatrix} \omega_N^{0\cdot 0} & \omega_N^{0\cdot 1} & \cdots & \omega_N^{0\cdot(N-1)} \\ \omega_N^{1\cdot 0} & \omega_N^{1\cdot 1} & \cdots & \omega_N^{1\cdot(N-1)} \\ \vdots & \vdots & \ddots & \vdots \\ \omega_N^{(N-1)\cdot 0} & \omega_N^{(N-1)\cdot 1} & \cdots & \omega_N^{(N-1)\cdot(N-1)} \end{bmatrix} \tag{4.3}$$

with $\omega_N = e^{-j2\pi/N}$. Inserting CP can be regarded as adding a length of N_{CP} which is indexed as $\left[s_k\left(-N_{CP}\right)\ s_k\left(-N_{CP}+1\right)\cdots s_k\left(-1\right)\right]^T$ with $s_k\left(i\right) = s_k\left(i + N\right), -N_{CP} \le i \le -1$.

We assume RA-preamble is transmitted though a block-stationary multipath channel, which means channel impulse response (CIR) is time-invariant during the symbol period.
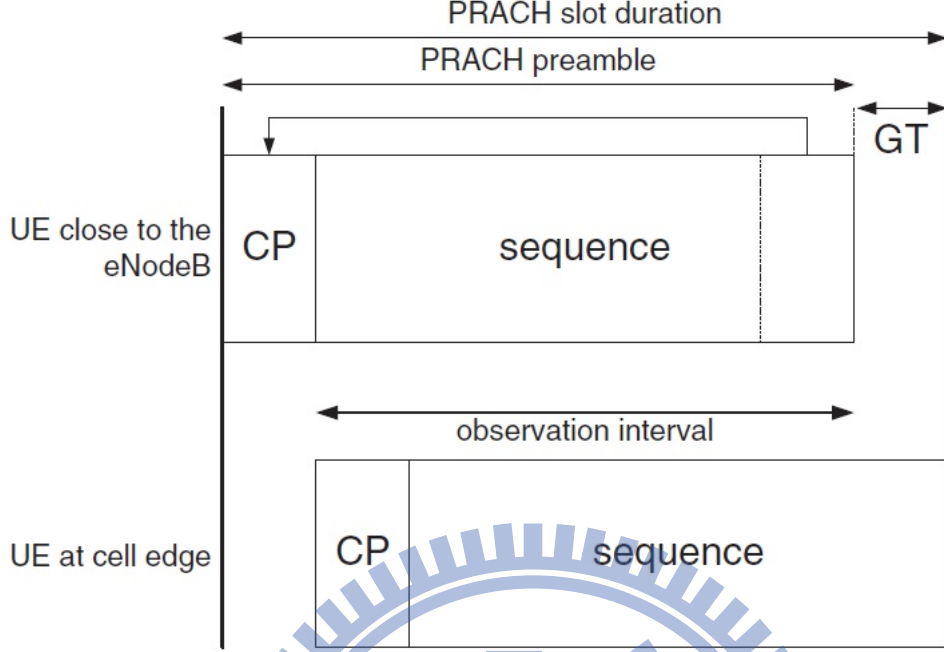
Figure 4.2: PRACH preamble received at the eNB [5, Figure 17.6].

Denote by L the maximum length of CIR and assume $L \geqslant N_{CP} - 1$. Denote the CIR by $\mathbf{h}_k = [h_k(0)\ h_k(1)\cdots h_k(L-1)]^T$. The UE aligns the start of the random access preamble with the start of the corresponding uplink subframe at the UE assuming a timing advance of zero [5]. Figure 4.2 shows two preambles at the eNodeB received with different timings depending on the propagation delay. Denote θ_k by the timing offset and $\theta_k \geq 0$.

Here we formulate the convolution operation in matrix form. So let $\mathbf{S}_k(\theta) \in \mathbb{C}^{N \times N}$ be a Toeplitz matrix containing the transmitted time-domain signal as

$$\mathbf{S}_k(\theta_k) = \begin{bmatrix} s_k(-\theta_k) & s_k(-\theta_k - 1) & \cdots & s_k(-\theta_k - (N-1)) \\ s_k(-\theta_k + 1) & s_k(-\theta_k) & \ddots & \vdots \\ \vdots & \ddots & \ddots & s_k(\theta_k - 1) \\ s_k(-\theta_k + (N-1)) & \cdots & s_k(-\theta_k + 1) & s_k(-\theta_k) \end{bmatrix} \quad (4.4)$$

where $s_k(i) = 0$ for $i < -N_{CP}$. Let ε be the normalized carrier frequency offset (CFO) with respect to the subcarrier spacing Δf_{RA}. Denote the received RA-preambles from all K UEs

after removing CP by vector $\mathbf{y} = [y(0)\ y(1) \cdots y(N-1)]^T$ as

$$\mathbf{y} = \sum_{k=1}^{K} \left(q_k \mathbf{\Gamma}(\varepsilon_k) \mathbf{S}_k(\theta_k) \mathbf{B} \mathbf{h}_k + \mathbf{n} \right) \tag{4.5}$$

where q_k denotes the presence of the RA-preamble as

$$q_k = \begin{cases} 1, & \text{if the RA-preamble is present,} \\ 0, & \text{if the RA-preamble is not present,} \end{cases} \tag{4.6}$$

$$\mathbf{\Gamma}(\varepsilon) = \text{diag}\left(1, e^{j\frac{2\pi}{N}\varepsilon}, e^{j\frac{2\pi}{N}\varepsilon\cdot 2}, \cdots, e^{j\frac{2\pi}{N}\varepsilon\cdot(N-1)} \right) \in \mathbb{C}^{N\times N} \tag{4.7}$$

is the phase rotation matrix induced by CFO, $\mathbf{B}$ is a matrix to append zeros to make it a N vector as

$$\mathbf{B} = \begin{bmatrix} \mathbf{I}_{L\times L} \\ \mathbf{0}_{(N-L)\times L} \end{bmatrix}, \tag{4.8}$$

and $\mathbf{n} = \left[n(0)\ n(1) \cdots n(L-1) \right]^T$ is a vector of complex additive white Gaussian noise (AWGN) with zero mean and unknown power σ_n^2.

We further assume $0 \le \theta \le N_{CP} - (L-1)$. That is, $\mathbf{y}$ only contains steady-state response of the channel to all RA-preambles. As a consequence, we can substitute $\mathbf{S}_k(\theta_k)$ in (4.4) with a circulant matrix

$$\widetilde{\mathbf{S}}_k(\theta) = \begin{bmatrix} s_k(-\theta) & s_k(-\theta+(N-1)) & \cdots & s_k(-\theta+1)) \\ s_k(-\theta+1) & s_k(-\theta) & \ddots & \vdots \\ \vdots & \ddots & \ddots & s_k(\theta+(N-1)) \\ s_k(-\theta+(N-1)) & \cdots & s_k(-\theta+1) & s_k(-\theta) \end{bmatrix} \tag{4.9}$$

and (4.5) can be rewritten as

$$\mathbf{y} = \sum_{k=1}^{K} q_k \mathbf{\Gamma}(\varepsilon_k) \widetilde{\mathbf{S}}_k(\theta_k) \mathbf{B} \mathbf{h}_k + \mathbf{n}. \tag{4.10}$$

We can further rewrite (4.10) as

$$\mathbf{y} = \sum_{k=1}^{K} q_k \mathbf{\Gamma}(\varepsilon_k) \mathbf{F}^H \mathbf{D}_k(\theta_k) \mathbf{F} \mathbf{B} \mathbf{h}_k + \mathbf{n} \tag{4.11}$$

where $\mathbf{D}_k(\theta_k)$ is a diagonal matrix where diagonal entries are the DFT of the first column of $\widetilde{\mathbf{S}}_k(\theta_k)$. Because the first column of $\widetilde{\mathbf{S}}_k(\theta_k)$ is the cyclic shift of $\mathbf{s}_k$ by $-\theta$, its DFT can be expressed as

$$\mathbf{D}_k(\theta_k) = \mathbf{\Gamma}(-\theta_k)\operatorname{diag}(\mathbf{c}_u). \tag{4.12}$$

Note that

$$\mathbf{D}_k(\theta_k)^H \mathbf{D}_k(\theta_k) = \operatorname{diag}^H(\mathbf{c}_u)\mathbf{\Gamma}^H(-\theta_k)\mathbf{\Gamma}(-\theta_k)\operatorname{diag}(\mathbf{c}_u) = \operatorname{diag}^H(\mathbf{c}_u)\operatorname{diag}(\mathbf{c}_u) = \mathbf{C} \tag{4.13}$$

where $\mathbf{C} = \operatorname{diag}(0, 0, \cdots, 0, 1, 1, \cdots, 1, 0, 0, \cdots, 0)$ with the 1s locating at element indices from ϕ to $\phi + N_{ZC} - 1$ along the diagonal and depends on neither θ nor k. We will use this fact in subsequent derivation.

4.2 Problem Formulation

4.2.1 Multiple hypothesis testing

Considering that multiple RA-preambles may be sent and received at the same time, we can formulate the problem as a multiple hypothesis testing problem. Each RA preamble has two possibilities—sent or not sent. Therefore, there are totally 2^K possible combinations of the condition for the preambles. We need to decide which one is true among the 2^K hypotheses. Assuming the noise is AWGN, We can write the multiple hypothesis testing problem using minimum distance criterion as

$$\min_{q_k, \varepsilon_k, \theta_k, \mathbf{h}_k, \forall k} \left\| \mathbf{y} - \sum_{k=1}^{K} q_k \mathbf{\Gamma}(\varepsilon_k)\mathbf{F}^H \mathbf{D}_k(\theta_k)\mathbf{FBh}_k \right\|_2^2. \tag{4.14}$$

Once we solve the set $\{q_k\}$ in the last equation, we will know what combination of RA-preambles are sent. We can rewrite (4.14) as

$$\min_{q_k, \varepsilon_k, \theta_k, \mathbf{h}_k, \forall k} \left\| \mathbf{y} - \left[q_1 \mathbf{\Gamma}(\varepsilon_1)\mathbf{F}^H \mathbf{D}_1(\theta_1)\mathbf{FB} \quad \cdots \quad q_K \mathbf{\Gamma}(\varepsilon_K)\mathbf{F}^H \mathbf{D}_K(\theta_K)\mathbf{FB} \right] \begin{bmatrix} \mathbf{h}_1 \\ \vdots \\ \mathbf{h}_K \end{bmatrix} \right\|_2^2. \tag{4.15}$$

Keeping $q_k, \varepsilon_k, \theta_k$ fixed, the least square (LS) solution of $\mathbf{h} \triangleq \begin{bmatrix} \mathbf{h}_1 & \mathbf{h}_2 & \cdots & \mathbf{h}_K \end{bmatrix}^T$ is given by

$$
\widehat{\mathbf{h}} = \left[\begin{bmatrix} q_1 \mathbf{B}^H \mathbf{F}^H \mathbf{D}_1^H (\theta_1) \mathbf{F} \mathbf{\Gamma}^H (\varepsilon_1) \\ \vdots \\ q_K \mathbf{B}^H \mathbf{F}^H \mathbf{D}_K^H (\theta_K) \mathbf{F} \mathbf{\Gamma}^H (\varepsilon_K) \end{bmatrix} \begin{bmatrix} q_1 \mathbf{\Gamma}(\varepsilon_1) \mathbf{F}^H \mathbf{D}_1 (\theta_1) \mathbf{F} \mathbf{B} & \cdots & q_K \mathbf{\Gamma}(\varepsilon_K) \mathbf{F}^H \mathbf{D}_K (\theta_K) \mathbf{F} \mathbf{B} \end{bmatrix} \right]^\dagger
$$
$$
\begin{bmatrix} q_1 \mathbf{B}^H \mathbf{F}^H \mathbf{D}_1^H (\theta_1) \mathbf{F} \mathbf{\Gamma}^H (\varepsilon_1) \\ \vdots \\ q_K \mathbf{B}^H \mathbf{F}^H \mathbf{D}_K^H (\theta_K) \mathbf{F} \mathbf{\Gamma}^H (\varepsilon_K) \end{bmatrix} \mathbf{y}
$$

$$(4.16)$$

where superscript $\dagger$ denotes Moore-Penrose pseudoinverse. A one-shot solution of the problem (See Appendix A) is found to have too high a computation complexity for implementation. Therefore, we consider the single-user detection strategy in the next subsection.

4.2.2 Binary hypothesis testing

In the single-user detection strategy, each RA-preamble is detected individually. That is, we decide which one of the following hypothesis is true: H_0, the RA-preamble $\mathbf{s}_k$ is not present in the observation $\mathbf{y}$; H_1, the RA-preamble $\mathbf{s}_k$ is present in the observation $\mathbf{y}$. For $\mathbf{s}_i$ with $i \neq k$, because it is not orthogonal to $\mathbf{s}_k$, if they are generated from ZC-sequences with different root indices, there will be multiple-access intereference (MAI), which will aggravate the detection performance. Although the individual detection strategy is suboptimal, it has the advantage of having a simple composite binary testing formulation. For RA-preamble $\mathbf{s}_k$, the problem can be written as

$$
\begin{cases} H_0: & \mathbf{y} = \mathbf{n}, \\ H_1: & \mathbf{y} = \mathbf{\Gamma}(\varepsilon_k) \mathbf{F}^H \mathbf{D}_k (\theta_k) \mathbf{F} \mathbf{B} \mathbf{h}_k + \mathbf{n}, \end{cases} \tag{4.17}
$$

where $\mathbf{n} = \begin{bmatrix} n(0) \, n(1) \cdots n(L-1) \end{bmatrix}^T$ is a vector of complex AWGN with zero mean and unknown power $\sigma^2 = \sigma_n^2 + \sigma_{MAI}^2$ with σ_{MAI}^2 being the average MAI power.

33

4.3 Random Access Techniques Based on GLRT

After we formulate our problem as one of binary hypothesis testing, we employ GLRT to decide whether the preamble is present or not. The GLRT is derived from the binary hypothesis testing assumption. Denote by p_i the probability density function (pdf) of $\mathbf{y}$ under the hypothesis H_i for $i = 0, 1$. Then the GLRT can be expressed as: Decide H_1 if

$$\frac{p_1\left(\mathbf{y}; \widehat{\varepsilon}_k, \widehat{\theta}_k, \widehat{\mathbf{h}}_k, \widehat{\sigma}^2_{H_1}\right)}{p_0\left(\mathbf{y}; \widehat{\sigma}^2_{H_0}\right)} > \lambda \tag{4.18}$$

where $\left(\widehat{\varepsilon}_k, \widehat{\theta}_k, \widehat{\mathbf{h}}_k\right)$ is the ML estimate of $(\varepsilon_k, \theta_k, \mathbf{h}_k)$ and $\widehat{\sigma}^2_{H_i}$ is the ML estimate of σ^2 conditioned on H_i for $i = 0, 1$ and λ is a threshold by adjusting which to a suitable value can attain a certain false alarm probability p_{fa} or detection probability p_d. From (4.17), we can write our pdf of $\mathbf{y}$ under H_i for $i = 0, 1$ as

$$p_1\left(\mathbf{y}; \varepsilon_k, \theta_k, \mathbf{h}_k, \sigma^2\right) = \frac{1}{(2\pi\sigma^2)^{\frac{N}{2}}} e^{\frac{-1}{2\sigma^2} \left\| \mathbf{y} - \mathbf{\Gamma}(\varepsilon_k) \mathbf{F}^H \mathbf{D}_k(\theta_k) \mathbf{F} \mathbf{B} \mathbf{h}_k \right\|^2_2} \tag{4.19}$$

and

$$p_0\left(\mathbf{y}; \sigma^2\right) = \frac{1}{(2\pi\sigma^2)^{\frac{N}{2}}} e^{\frac{-1}{2\sigma^2} \|\mathbf{y}\|^2_2}. \tag{4.20}$$

For H_0, the ML estimate $\widehat{\sigma}^2_{H_0}$ is found by solving $\max_{\sigma^2} p_0\left(\mathbf{y}; \sigma^2\right)$. Maximizing over σ^2, we get

$$\widehat{\sigma}^2_{H_0} = \frac{\|\mathbf{y}\|^2_2}{N/2}. \tag{4.21}$$

Substituting back into the pdf, we have

$$p_0\left(\mathbf{y}; \widehat{\sigma}^2_{H_0}\right) = \left(\frac{N/2}{\pi e \|\mathbf{y}\|^2_2}\right)^{N/2}. \tag{4.22}$$

For H_1, the ML estimates $\left(\widehat{\varepsilon}_k, \widehat{\theta}_k, \widehat{\mathbf{h}}_k, \widehat{\sigma}^2_{H_1}\right)$ are found by solving $\max_{\varepsilon_k, \theta_k, \mathbf{h}_k, \sigma^2} p_1\left(\mathbf{y}; \varepsilon_k, \theta_k, \mathbf{h}_k, \sigma^2\right)$,

for which we get

$$
\begin{aligned}
\max_{\varepsilon_k,\theta_k,\mathbf{h}_k,\sigma^2} p_1\left(\mathbf{y};\varepsilon_k,\theta_k,\mathbf{h}_k,\sigma^2\right) &= \max_{\varepsilon_k,\theta_k,\mathbf{h}_k,\sigma^2} \frac{1}{(2\pi\sigma^2)^{\frac{N}{2}}} e^{\frac{-1}{2\sigma^2}\left\|\mathbf{y}-\boldsymbol{\Gamma}(\varepsilon_k)\mathbf{F}^H\mathbf{D}_k(\theta_k)\mathbf{F}\mathbf{B}\mathbf{h}_k\right\|_2^2} \\
&= \max_{\varepsilon_k,\theta_k,\mathbf{h}_k,\sigma^2} \frac{1}{(2\pi\sigma^2)^{\frac{N}{2}}} e^{\frac{-1}{2\sigma^2}\left\|\mathbf{y}-\boldsymbol{\Gamma}(\varepsilon_k)\mathbf{F}^H\mathbf{D}_k(\theta_k)\mathbf{F}\mathbf{B}\mathbf{h}_k\right\|_2^2} \\
&= \max_{\sigma^2} \frac{1}{(2\pi\sigma^2)^{\frac{N}{2}}} e^{\frac{-1}{2\sigma^2}\min_{\varepsilon_k,\theta_k,\mathbf{h}_k}\left\|\mathbf{y}-\boldsymbol{\Gamma}(\varepsilon_k)\mathbf{F}^H\mathbf{D}_k(\theta_k)\mathbf{F}\mathbf{B}\mathbf{h}_k\right\|_2^2}.
\end{aligned} \tag{4.23}
$$

Maximizing over σ^2, we get

$$
\widehat{\sigma}_{H_1}^2 = \frac{\displaystyle\min_{\varepsilon_k,\theta_k,\mathbf{h}_k}\left\|\mathbf{y}-\boldsymbol{\Gamma}(\varepsilon_k)\mathbf{F}^H\mathbf{D}_k\left(\theta_k\right)\mathbf{F}\mathbf{B}\mathbf{h}_k\right\|_2^2}{N/2}. \tag{4.24}
$$

Substituting back into (4.25), we obtain

$$
\max_{\varepsilon_k,\theta_k,\mathbf{h}_k} p_1\left(\mathbf{y};\varepsilon_k,\theta_k,\mathbf{h}_k,\widehat{\sigma}_{H_1}^2\right) = \left(\frac{N/2}{\pi e\,\displaystyle\min_{\varepsilon_k,\theta_k,\mathbf{h}_k}\left\|\mathbf{y}-\boldsymbol{\Gamma}(\varepsilon_k)\mathbf{F}^H\mathbf{D}_k\left(\theta_k\right)\mathbf{F}\mathbf{B}\mathbf{h}_k\right\|_2^2}\right)^{N/2}. \tag{4.25}
$$

Further,

$$
\min_{\varepsilon_k,\theta_k,\mathbf{h}_k}\left\|\mathbf{y}-\boldsymbol{\Gamma}(\varepsilon_k)\mathbf{F}^H\mathbf{D}_k\left(\theta_k\right)\mathbf{F}\mathbf{B}\mathbf{h}_k\right\|_2^2 = \min_{\varepsilon_k,\theta_k}\min_{\varepsilon_k,\theta_k|\mathbf{h}_k}\left\|\mathbf{y}-\boldsymbol{\Gamma}(\varepsilon_k)\mathbf{F}^H\mathbf{D}_k\left(\theta_k\right)\mathbf{F}\mathbf{B}\mathbf{h}_k\right\|_2^2. \tag{4.26}
$$

The inner minimization can be solved by the LS method whose solution is

$$
\begin{aligned}
\widehat{\mathbf{h}}_k &= \left[\mathbf{B}^H\mathbf{F}^H\mathbf{D}_k^H\left(\theta_k\right)\mathbf{F}\boldsymbol{\Gamma}^H(\varepsilon_k)\boldsymbol{\Gamma}(\varepsilon_k)\mathbf{F}^H\mathbf{D}_k\left(\theta_k\right)\mathbf{F}\mathbf{B}\right]^{\dagger}\boldsymbol{\Gamma}(\varepsilon_k)\mathbf{F}^H\mathbf{D}_k\left(\theta_k\right)\mathbf{F}\mathbf{B}\mathbf{y} \\
&= \left[\mathbf{B}^H\mathbf{F}^H\mathbf{C}\mathbf{F}\mathbf{B}\right]^{\dagger}\mathbf{B}^H\mathbf{F}^H\mathbf{D}_k^H\left(\theta_k\right)\mathbf{F}\boldsymbol{\Gamma}^H(\varepsilon_k)\mathbf{y}.
\end{aligned} \tag{4.27}
$$

Then,

$$
\begin{aligned}
&\min_{\varepsilon_k,\theta_k}\min_{\mathbf{h}_k|\varepsilon_k,\theta_k}\left\|\mathbf{y}-\boldsymbol{\Gamma}(\varepsilon_k)\mathbf{F}^H\mathbf{D}_k\left(\theta_k\right)\mathbf{F}\mathbf{B}\mathbf{h}_k\right\|_2^2 \\
&\quad = \min_{\varepsilon_k,\theta_k}\left\|\mathbf{y}-\boldsymbol{\Gamma}(\varepsilon_k)\mathbf{F}^H\mathbf{D}_k\left(\theta_k\right)\mathbf{F}\mathbf{B}\left[\mathbf{B}^H\mathbf{F}^H\mathbf{C}\mathbf{F}\mathbf{B}\right]^{\dagger}\mathbf{B}^H\mathbf{F}^H\mathbf{D}_k^H\left(\theta_k\right)\mathbf{F}\boldsymbol{\Gamma}^H(\varepsilon_k)\mathbf{y}\right\|_2^2. \tag{4.28}
\end{aligned}
$$

Unfortunately, the last equation cannot be solved efficiently, for we cannot find a closed-form solution. We need to search for every possible values of θ and ε_k, which is impractical to implement because it takes too much computation. To proceed, we temporarily relax the

35

length constraint on $\mathbf{h}_k$. That is, we define $\mathbf{B}' = \mathbf{I}_{N \times N}$ and let $\mathbf{h}'_k$ be an $N \times 1$ vector whose entries can be any value to replace $\mathbf{B}\mathbf{h}_k$. Using the new definition, (4.27) becomes simplified to

$$
\begin{aligned}
\widehat{\mathbf{h}}'_k &= \left[\mathbf{F}^H \mathbf{C} \mathbf{F}\right]^\dagger \mathbf{F}^H \mathbf{D}_k^H \left(\theta_k\right) \mathbf{F}\mathbf{\Gamma}^H(\varepsilon_k)\mathbf{y} \\
&= \mathbf{F}^H \mathbf{D}_k^H \left(\theta_k\right) \mathbf{F}\mathbf{\Gamma}^H(\varepsilon_k)\mathbf{y}.
\end{aligned}
\tag{4.29}
$$

Substituting $\widehat{\mathbf{h}}'_k$ back, we have

$$
\begin{aligned}
\min_{\varepsilon_k, \theta_k} \min_{\mathbf{h}_k | \varepsilon_k, \theta_k} & \left\| \mathbf{y} - \mathbf{\Gamma}(\varepsilon_k)\mathbf{F}^H \mathbf{D}_k \left(\theta_k\right) \mathbf{F}\mathbf{I}\mathbf{h}_k \right\|_2^2 \\
&= \min_{\varepsilon_k, \theta_k} \left\| \mathbf{y} - \mathbf{\Gamma}(\varepsilon_k)\mathbf{F}^H \mathbf{D}_k \left(\theta_k\right) \mathbf{F}\mathbf{I}\mathbf{F}^H \mathbf{D}_k^H \left(\theta_k\right) \mathbf{F}\mathbf{\Gamma}^H(\varepsilon_k)\mathbf{y} \right\|_2^2 \\
&= \min_{\varepsilon_k, \theta_k} \left\| \mathbf{y} - \mathbf{\Gamma}(\varepsilon_k)\mathbf{F}^H \mathbf{C}\mathbf{F}\mathbf{\Gamma}^H(\varepsilon_k)\mathbf{y} \right\|_2^2.
\end{aligned}
\tag{4.30}
$$

We find that now the minimization depends on ε_k only, which allows us to get an maximum likelihood estimation (MLE) of ε_k first under the condition of no CIR length constraint. Therefore, we will first get $\widehat{\varepsilon}_k$ by using this assumption. Then we go back to the original formulation to solve for the timing offsets and do RA-preamble detection.

4.3.1 Estimation of CFO

The MLE of CFO is found by solving

$$
\begin{aligned}
\widehat{\varepsilon}_k &= \operatorname*{argmin}_{\varepsilon_k} \left\| \mathbf{y} - \mathbf{\Gamma}(\varepsilon_k)\mathbf{F}^H \mathbf{C}\mathbf{F}\mathbf{\Gamma}^H(\varepsilon_k)\mathbf{y} \right\|_2^2 \\
&= \operatorname*{argmax}_{\varepsilon_k} \left\| \mathbf{y}\mathbf{\Gamma}(\varepsilon_k)\mathbf{F}^H \mathbf{C}\mathbf{F}\mathbf{\Gamma}^H(\varepsilon_k)\mathbf{y} \right\|_2^2.
\end{aligned}
\tag{4.31}
$$

After expanding the matrices in (4.31), we can rewrite it as

$$
\widehat{\varepsilon}_k = \operatorname*{argmax}_{\varepsilon_k} \mathfrak{R} \left\{ \sum_{k=0}^{N-1} \psi\left(k\right) R_{yy}\left(k\right) \omega_N^{k\varepsilon} \right\}
\tag{4.32}
$$

where $\mathfrak{R}\{\cdot\}$ denotes the real part of its argument, $\psi\left(k\right)$ is the DFT of the diagonal terms of $\mathbf{C}$ and $R_{yy}\left(k\right)$ is the temporal autocorrelation of $y(m)$ given as

$$
R_{yy}\left(k\right) = \sum_{m=\max\{-k,0\}}^{\min\{N-1, N-1-k\}} y^*\left(m\right) y\left(m+k\right).
\tag{4.33}
$$

The maximization target in (4.32) is a high-order polynomial function of ε_k which has no closed-form solution. We need to use a line search method to solve it. However the summation in (4.32) can be treated as a Fourier transform of the sequence $\psi(k) R_{yy}(k)$. Hence, we can apply a high-order fast Fourier transform (FFT) to a zero-padded version of the sequence and find the maximum point of its real part. Note that, the accuracy of this estimation will depend on the size of the FFT used. However, we found that the optimization in (4.32) looks like a sinusodial function with a period of nearly one subcarrier depending on CIR. That it, only the fractional CFO (FCFO) can be estimated reliably. Due to the influence of the noise, it is very probable to get a wrong estimation of the integer CFO (ICFO). Therefore, ICFO needs to be estimated in a later step. The procedure can be summarized as: a) apply no length constraints on $\mathbf{h}_k$ and use (4.32) to estimate FCFO, and b) go back to (4.27) to estimate ICFO and θ_k.

4.3.2 Estimation of ICFO, timing offset and channel response

After getting the estimate of FCFO, we still have ICFO and timing offset to estimate. After compensating FCFO, the minimization becomes

$$\min_{\varepsilon_{k_I}, \theta_k} \left\| \widetilde{\mathbf{y}} - \mathbf{\Gamma}(\varepsilon_{k_I}) \mathbf{F}^H \mathbf{D}_k(\theta_k) \mathbf{F} \mathbf{B} \left[\mathbf{B}^H \mathbf{F}^H \mathbf{C} \mathbf{F} \mathbf{B} \right]^\dagger \mathbf{B}^H \mathbf{F}^H \mathbf{D}_k^H(\theta_k) \mathbf{F} \mathbf{\Gamma}^H(\varepsilon_{k_I}) \widetilde{\mathbf{y}} \right\|_2^2 \qquad (4.34)$$

where $\widetilde{\mathbf{y}}$ is the received signal after compensating FCFO, defined as

$$\widetilde{\mathbf{y}} = \mathbf{\Gamma}(-\widehat{\varepsilon}_{k_F}) \mathbf{y}. \qquad (4.35)$$

The Moore-Penrose pseudoinverse in (4.34) is too complicated to implement. Thus, we find a simple approximation by observing the structure of $\mathbf{B}^H \mathbf{F}^H \mathbf{C} \mathbf{F} \mathbf{B}$. Focusing on the $\left[\mathbf{B}^H \mathbf{F}^H \mathbf{C} \mathbf{F} \mathbf{B} \right]^\dagger \mathbf{B}^H \mathbf{F}^H \mathbf{D}_k$ term, because of the structure of the $\mathbf{C}$ and $\mathbf{D}_k$, we have

$$\left[\mathbf{B}^H \mathbf{F}^H \mathbf{C} \mathbf{F} \mathbf{B} \right]^\dagger \mathbf{B}^H \mathbf{F}^H \mathbf{D}_k = \left[\mathbf{B}^H \mathbf{F}^H \mathbf{C}^H \mathbf{C} \mathbf{F} \mathbf{B} \right]^\dagger \mathbf{B}^H \mathbf{F}^H \mathbf{C}^H \mathbf{D}_k. \qquad (4.36)$$

37
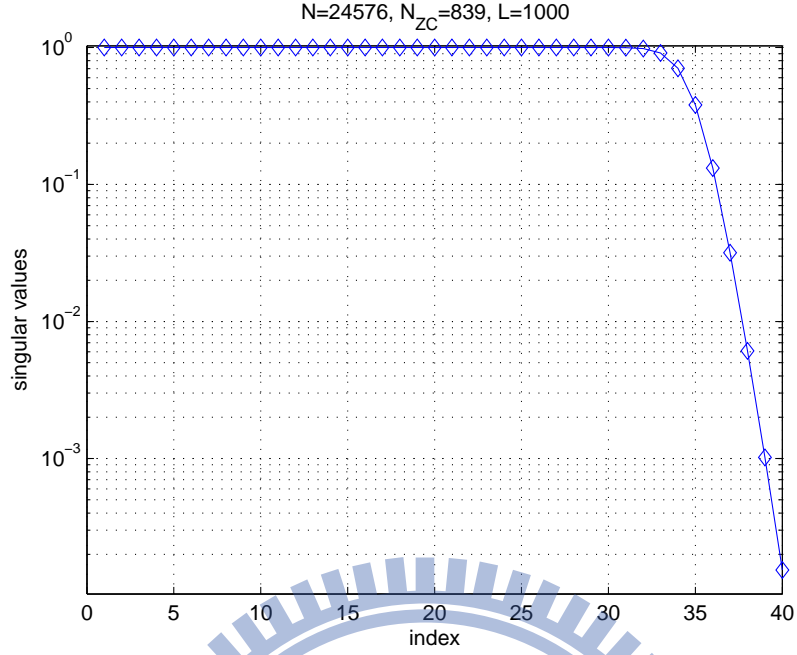
Figure 4.3: Singular values.

The singular value decomposition (SVD) of $\mathbf{CFB}$ can be expressed as

$$\mathbf{CFB} = \mathbf{U\Sigma V}^H. \tag{4.37}$$

Then,

$$
\begin{aligned}
\left[\mathbf{B}^H\mathbf{F}^H\mathbf{C}^H\mathbf{CFB}\right]^\dagger \mathbf{B}^H\mathbf{F}^H\mathbf{C}^H &= \left[\mathbf{V\Sigma}^H\mathbf{U}^H\mathbf{U\Sigma V}^H\right]^\dagger \mathbf{V\Sigma}^H\mathbf{U}^H \\
&= \left[\mathbf{V\Sigma}^H\mathbf{\Sigma V}^H\right]^\dagger \mathbf{V\Sigma}^H\mathbf{U}^H \\
&= \mathbf{V}\left[\mathbf{\Sigma}^H\mathbf{\Sigma}\right]^\dagger \mathbf{V}^H\mathbf{V\Sigma}^H\mathbf{U}^H \\
&= \mathbf{V}\left[\mathbf{\Sigma}^H\mathbf{\Sigma}\right]^\dagger \mathbf{\Sigma}^H\mathbf{U}^H.
\end{aligned}
\tag{4.38}
$$

Observing the singular values in $\mathbf{\Sigma}^H\mathbf{\Sigma}$ in Figure 4.3, we can approximate the singular values as a rectangular function, where the number of 1s can be approximated as $\frac{N_{ZC}}{N}L$. Therefore,

$$\mathbf{V}\left[\mathbf{\Sigma}^H\mathbf{\Sigma}\right]^\dagger \mathbf{\Sigma}^H\mathbf{U}^H \approx \mathbf{V\Sigma}^H\mathbf{U}^H = \mathbf{B}^H\mathbf{F}^H\mathbf{C}^H. \tag{4.39}$$

38

As a result, (4.34) can be approximated as

$$\min_{\varepsilon_{k_I},\theta_k} \left\| \widetilde{\mathbf{y}} - \boldsymbol{\Gamma}(\varepsilon_{k_I})\mathbf{F}^H\mathbf{D}_k\left(\theta_k\right)\mathbf{F}\mathbf{B}\left[\mathbf{B}^H\mathbf{F}^H\mathbf{C}\mathbf{F}\mathbf{B}\right]^\dagger \mathbf{B}^H\mathbf{F}^H\mathbf{D}_k^H\left(\theta_k\right)\mathbf{F}\boldsymbol{\Gamma}^H(\varepsilon_{k_I})\widetilde{\mathbf{y}} \right\|_2^2$$

$$\approx \min_{\varepsilon_{k_I},\theta_k} \left\| \widetilde{\mathbf{y}} - \boldsymbol{\Gamma}(\varepsilon_{k_I})\mathbf{F}^H\mathbf{D}_k\left(\theta_k\right)\mathbf{F}\mathbf{B}\mathbf{B}^H\mathbf{F}^H\mathbf{D}_k^H\left(\theta_k\right)\mathbf{F}\boldsymbol{\Gamma}^H(\varepsilon_{k_I})\widetilde{\mathbf{y}} \right\|_2^2. \qquad (4.40)$$

Notice that $\widehat{\mathbf{h}}_k \approx \mathbf{B}^H\mathbf{F}^H\mathbf{D}_k^H\left(\theta_k\right)\mathbf{F}\boldsymbol{\Gamma}^H(\varepsilon_{k_I})\widetilde{\mathbf{y}}$, where $\widehat{\mathbf{h}}_k$ can be simply approximated by taking the first L taps of the no–length–constraint channel estimate $\widehat{\mathbf{h}}_k'$. We expand the last expression as

$$\min_{\varepsilon_{k_I},\theta_k} \left\| \widetilde{\mathbf{y}} - \boldsymbol{\Gamma}(\varepsilon_{k_I})\mathbf{F}^H\mathbf{D}_k\left(\theta_k\right)\mathbf{F}\mathbf{B}\mathbf{B}^H\mathbf{F}^H\mathbf{D}_k^H\left(\theta_k\right)\mathbf{F}\boldsymbol{\Gamma}^H(\varepsilon_{k_I})\widetilde{\mathbf{y}} \right\|_2^2$$

$$= \min_{\varepsilon_{k_I},\theta_k} \widetilde{\mathbf{y}}^H\widetilde{\mathbf{y}} - 2\widetilde{\mathbf{y}}^H\boldsymbol{\Gamma}(\varepsilon_{k_I})\mathbf{F}^H\mathbf{D}_k\left(\theta_k\right)\mathbf{F}\mathbf{B}\mathbf{B}^H\mathbf{F}^H\mathbf{D}_k^H\left(\theta_k\right)\mathbf{F}\boldsymbol{\Gamma}^H(\varepsilon_{k_I})\widetilde{\mathbf{y}}$$

$$+\widetilde{\mathbf{y}}^H\boldsymbol{\Gamma}(\varepsilon_{k_I})\mathbf{F}^H\mathbf{D}_k\left(\theta_k\right)\mathbf{F}\mathbf{B}\mathbf{B}^H\mathbf{F}^H\mathbf{C}\mathbf{F}\mathbf{B}\mathbf{B}^H\mathbf{F}^H\mathbf{D}_k^H\left(\theta_k\right)\mathbf{F}\boldsymbol{\Gamma}^H(\varepsilon_{k_I})\widetilde{\mathbf{y}}.$$

$$(4.41)$$

Again, because of the structure of the $\mathbf{C}$ and $\mathbf{D}_k\left(\theta_k\right)$, the last expression can be rewritten as:

$$\min_{\varepsilon_{k_I},\theta_k} \widetilde{\mathbf{y}}^H\widetilde{\mathbf{y}} - 2\widetilde{\mathbf{y}}^H\boldsymbol{\Gamma}(\varepsilon_{k_I})\mathbf{F}^H\mathbf{D}_k\left(\theta_k\right)\mathbf{C}\mathbf{F}\mathbf{B}\mathbf{B}^H\mathbf{F}^H\mathbf{C}^H\mathbf{D}_k^H\left(\theta_k\right)\mathbf{F}\boldsymbol{\Gamma}^H(\varepsilon_{k_I})\widetilde{\mathbf{y}}$$

$$+ \ \widetilde{\mathbf{y}}^H\boldsymbol{\Gamma}(\varepsilon_{k_I})\mathbf{F}^H\mathbf{D}_k\left(\theta_k\right)\mathbf{C}\mathbf{F}\mathbf{B}\mathbf{B}^H\mathbf{F}^H\mathbf{C}^H\mathbf{C}\mathbf{F}\mathbf{B}\mathbf{B}^H\mathbf{F}^H\mathbf{C}^H\mathbf{D}_k^H\left(\theta_k\right)\mathbf{F}\boldsymbol{\Gamma}^H(\varepsilon_{k_I})\widetilde{\mathbf{y}}. \quad (4.42)$$

Note that $\mathbf{C}\mathbf{F}\mathbf{B}\mathbf{B}^H\mathbf{F}^H\mathbf{C}^H = \mathbf{U}\boldsymbol{\Sigma}\mathbf{V}^H\mathbf{V}\boldsymbol{\Sigma}^H\mathbf{U}^H = \mathbf{U}\boldsymbol{\Sigma}\boldsymbol{\Sigma}^H\mathbf{U}^H$ and $\mathbf{C}\mathbf{F}\mathbf{B}\mathbf{B}^H\mathbf{F}^H\mathbf{C}^H\mathbf{C}\mathbf{F}\mathbf{B}\mathbf{B}^H\mathbf{F}^H\mathbf{C}^H = \mathbf{U}\boldsymbol{\Sigma}\boldsymbol{\Sigma}^H\boldsymbol{\Sigma}\boldsymbol{\Sigma}^H\mathbf{U}^H$. Because of the properties of the singular values of $\boldsymbol{\Sigma}\boldsymbol{\Sigma}^H$ in Figure 4.3, we can approximate $\mathbf{C}\mathbf{F}\mathbf{B}\mathbf{B}^H\mathbf{F}^H\mathbf{C}^H\mathbf{C}\mathbf{F}\mathbf{B}\mathbf{B}^H\mathbf{F}^H\mathbf{C}^H$ as $\mathbf{C}\mathbf{F}\mathbf{B}\mathbf{B}^H\mathbf{F}^H\mathbf{C}^H$. Using the approximation above, (4.41) becomes

$$\min_{\varepsilon_{k_I},\theta_k} \widetilde{\mathbf{y}}^H\widetilde{\mathbf{y}} - 2\widetilde{\mathbf{y}}^H\boldsymbol{\Gamma}(\varepsilon_{k_I})\mathbf{F}^H\mathbf{D}_k\left(\theta_k\right)\mathbf{F}\mathbf{B}\mathbf{B}^H\mathbf{F}^H\mathbf{D}_k^H\left(\theta_k\right)\mathbf{F}\boldsymbol{\Gamma}^H(\varepsilon_{k_I})\widetilde{\mathbf{y}}$$

$$+\widetilde{\mathbf{y}}^H\boldsymbol{\Gamma}(\varepsilon_{k_I})\mathbf{F}^H\mathbf{D}_k\left(\theta_k\right)\mathbf{F}\mathbf{B}\mathbf{B}^H\mathbf{F}^H\mathbf{C}\mathbf{F}\mathbf{B}\mathbf{B}^H\mathbf{F}^H\mathbf{D}_k^H\left(\theta_k\right)\mathbf{F}\boldsymbol{\Gamma}^H(\varepsilon_{k_I})\widetilde{\mathbf{y}}$$

$$\approx \min_{\varepsilon_{k_I},\theta_k} \widetilde{\mathbf{y}}^H\widetilde{\mathbf{y}} - \widetilde{\mathbf{y}}^H\boldsymbol{\Gamma}(\varepsilon_{k_I})\mathbf{F}^H\mathbf{D}_k\left(\theta_k\right)\mathbf{F}\mathbf{B}\mathbf{B}^H\mathbf{F}^H\mathbf{D}_k^H\left(\theta_k\right)\mathbf{F}\boldsymbol{\Gamma}^H(\varepsilon_{k_I})\widetilde{\mathbf{y}}$$

$$= \min_{\varepsilon_{k_I},\theta_k} \|\mathbf{y}\|_2^2 - \left\| \mathbf{B}^H\mathbf{F}^H\mathbf{D}_k^H\left(\theta_k\right)\mathbf{F}\boldsymbol{\Gamma}^H(\varepsilon_{k_I})\widetilde{\mathbf{y}} \right\|_2^2. \qquad (4.43)$$

which is equivalent to solving

$$\max_{\varepsilon_{k_I}, \theta_k} \left\| \mathbf{B}^H \mathbf{F}^H \mathbf{D}_k^H \left(\theta_k \right) \mathbf{F} \mathbf{\Gamma}^H (\varepsilon_{k_I}) \widetilde{\mathbf{y}} \right\|_2^2 = \max_{\varepsilon_{k_I}, \theta_k} \left\| \widehat{\mathbf{h}}_k \right\|_2^2. \tag{4.44}$$

We can interpret the last equation as finding the combinations of ε_{k_I} and θ that yield the biggest energy in the first L taps of the no-length-constraint channel estimate $\widehat{\mathbf{h}}'_k$. And since the different values of θ will result in different cyclic shifts of $\widehat{\mathbf{h}}'_k$, computation can be simplified when finding θ.

4.3.3 GLRT

After obtaining all the ML estimates for H_0 and H_1, GLRT is eventually reduced to

$$\frac{\max_{\varepsilon_{k_I}, \theta_k} p_1 \left(\mathbf{y}; \varepsilon_{k_I}, \theta_k, \widehat{\mathbf{h}}_k, \widehat{\varepsilon}_{k_F}, \widehat{\sigma}_{H_1}^2 \right)}{p_0 \left(\mathbf{y}; \widehat{\sigma}_{H_0}^2 \right)} = \left(\frac{\|\mathbf{y}\|_2^2}{\|\mathbf{y}\|_2^2 - \max_{\varepsilon_{k_I}, \theta_k} \left\| \mathbf{B}^H \mathbf{F}^H \mathbf{D}_k^H \left(\theta_k \right) \mathbf{F} \mathbf{\Gamma}^H (\varepsilon_{k_I}) \widetilde{\mathbf{y}} \right\|_2^2} \right)^{N/2} \overset{H_1}{\underset{}{\gtrless}} \lambda, \tag{4.45}$$

which is equivalent to

$$\frac{\max_{\varepsilon_{k_I}, \theta_k} \left\| \mathbf{B}^H \mathbf{F}^H \mathbf{D}_k^H \left(\theta_k \right) \mathbf{F} \mathbf{\Gamma}^H (\varepsilon_{k_I}) \widetilde{\mathbf{y}} \right\|_2^2}{\|\mathbf{y}\|_2^2} \overset{H_1}{\underset{}{\gtrless}} \gamma \tag{4.46}$$

where $\gamma = 1 - \lambda^{-1}$. Based on this GLRT, we can finally decide whether the preamble is present or not.

4.3.4 Remarks

When we set $L = 1$ and not assume no FCFO, the GLRT detector in (4.46) is reduced to

$$\frac{\max_{\theta_k} \left\| \widetilde{h}_k \left(\theta_k \right) \right\|_2^2}{\|\mathbf{y}\|_2^2} \overset{H_1}{\underset{}{\gtrless}} \gamma \tag{4.47}$$

where

$$\widetilde{\mathbf{h}}_k = \mathbf{F}^H \mathrm{diag}^H \left(\mathbf{c}_k \right) \mathbf{F} \mathbf{y}. \tag{4.48}$$

This detector will find the peak location of $\widetilde{\mathbf{h}}_k$ as the timing offset and use its energy as a detection criterion, which is just the conventional detector (CD) discussed in [5]. Our GLRT detector will reduce to CD under the assumption of a flat-fading ($L = 1$) channel.
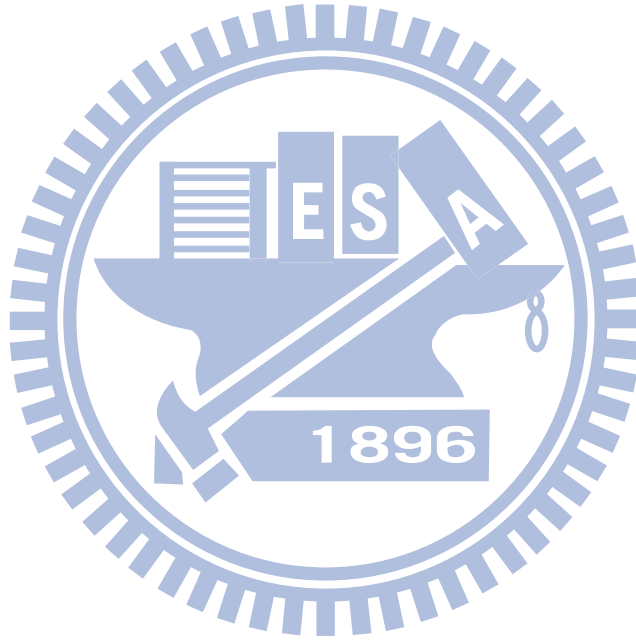
Chapter 5

Simulation Results

In this chapter, we present the simulation results for the proposed GLRT detector for random access in the LTE-A release 10 system. We compare the results of solving FCFO and not solving FCFO. Solving FCFO means our normal assumption (taking FCFO into account) while not solving FCFO means that we assume there is no FCFO in the preamble. Also we will see the results by assuming different CIR length L. We evaluate the performance mainly by observing the correct detection probability P_d and the false alarm probability P_{fa}.

5.1 PRACH Minimum Requirement in TS 36.141

We later will compare our proposed GLRT to PRACH minimum requirement in 3GPP TS 36.141 [9]. In 3GPP 36.141, two channel modes are tested, namely AWGN and ETU70. The definition of wrong timing estimation is different from our previous definition, because TS 36.141 is made for conventional detectors under single-path assumption. The timing in TS 36.141 refers to the estimated strongest path. For AWGN, a timing estimation error occurs if the estimation error of the timing of the strongest path is larger than 1.04 μs. For ETU70, a timing estimation error occurs if the estimation error of the timing of the strongest path is larger than 2.08 μs. The strongest path for the timing estimation error refers to the strongest

Table 5.1: PRACH Detection Test Requirements for Normal Mode [9, Table 8.4.1.5-1]

Number of TX antennas	Number of RX antennas	Propagation conditions	Frequency offset	SNR (dB)				
				Preamble format 0	Preamble format 1	Preamble format 2	Preamble format 3	Preamble format 4
1	2	AWGN	0	−13.9	−13.9	−16.1	−16.2	−6.9
		ETU70	270 Hz	−7.4	−7.2	−9.4	−9.5	0.5
	4	AWGN	0	−16.6	−16.4	−18.7	−18.5	−9.54
		ETU70	270 Hz	−11.5	−11.1	−13.5	−13.3	−4.5

Table 5.2: PRACH Detection Test Requirements for High Speed Mode [9, Table 8.4.1.5-2]

Number of TX antennas	Number of RX antennas	Propagation conditions	Frequency offset	SNR [dB]			
				Preamble format 0	Preamble format 1	Preamble format 2	Preamble format 3
1	2	AWGN	0	−13.8	−13.9	−16.0	−16.3
		ETU70	270 Hz	−6.8	−6.7	−8.7	−8.9
		AWGN	625 Hz	−12.1	−12.0	−14.1	−14.1
		AWGN	1340 Hz	−13.1	−13.2	−15.2	−15.4
	4	AWGN	0	−16.6	−16.3	−18.6	−18.5
		ETU70	270 Hz	−11.2	−10.8	−13.1	−13.1
		AWGN	625 Hz	−14.6	−14.3	−16.5	−16.5
		AWGN	1340 Hz	−15.6	−15.2	−17.5	−17.5

path (i.e., average of the delay of all paths having the same highest gain = 310 ns for ETU) in the power delay profile.

PRACH minimum requirement performance are listed in Tables 5.1 and 5.2. The normal mode test is applicable to all BS. The high speed mode test is applicable to high speed BS. The minimum requirements are as follows: P_{fa} shall not exceed 0.1%, and P_d shall not be below 99% for the SNRs in Tables 5.1 and 5.2.

Since the PRACH (preamble format 0–3: 839×1.25 kHz, burst format 4: 139×7.5 kHz) does not occupy the full bandwidth, a special SNR correction factor is applied which depends

Table 5.3: SNR Correction Factor for PRACH [11, Table 21]

Bandwidth in MHz	Factor in dB	
	Preamble format 0–3	Preamble format 4
1.4	−0.13	−0.15
3	−4.11	−4.13
5	−6.33	−6.35
10	−9.34	−9.36
15	−11.10	−11.13
20	−12.34	−12.37

Table 5.4: System Parameters for LTE-A Random Access

Parameters	values
Carrier freqeuncy	2 GHz
Channel bandwidth	20 MHz
IDFT size	24576
N_{ZC}	839
Preamble format	0
ϕ	5431
Δf_{RA}	1.25 kHz

on the bandwidth and the preamble format in Table 5.3 [11].

5.2 Simulation Conditions

This section introduces the system parameters and the channel models used in our simulation. In chapter 2, we introduced the specification of the LTE-A release 10 PRACH system. The system parameters used in our simulation are listed in Table 5.4. Assume that the cell radius is 1.5 km, that is, the maximum propagation delay θ_{max} is 307 (normalized by the sampling period). The performance of GLRT detector is evaluated in the presence of a single UE with a fixed timing $\theta_1 = 100$. We consider the following channel models: AWGN, SUI, and ETU70.

Table 5.5: Mean Delay and RMS Delay Spread of Each SUI Channel Model

Channel type	Path delay (μs)	Path power (dB)	Mean delay (μs)	RMS delay spread (μs)
SUI1	0, 0.4, 0.9	$0, -15, -20$	0.0208	0.1105
SUI2	0, 0.4, 1.1	$0, -12, -15$	0.0548	0.2029
SUI3	0, 0.4, 0.9	$0, -5, -10$	0.1529	0.2637
SUI4	0, 1.5, 4	$0, -4, -8$	0.7909	1.2566
SUI5	0, 4, 10	$0, -5, -10$	1.5993	2.8418
SUI6	0, 14, 20	$0, -10, -14$	1.9268	5.2397

The SUI models consist of 6 different radio channel models in three terrain categories [8]. The three terrain types in suburban area are:

- A: hilly terrain with moderate-to-heavy tree densities,

- C: flat terrain with light tree densities, and

- B: intermediate path loss condition between A and C.

The correspondence with the so-called SUI channels is as follows:

- C: SUI1, SUI2,

- B: SUI3, SUI4, and

- A: SUI5, SUI6.

In the above, SUI1 and SUI2 are Ricean multipath channels, whereas the other four are Rayleigh multipath channels. The Rayleigh channels are more hostile and exhibit a greater root-mean-square (RMS) delay spread. The SUI2 represents a worst-case link for terrain type C. We employ the all six SUI models in our simulation. The mean delay and RMS delay spread of each model are as shown in Table 5.5.

Table 5.6: Extended Typical Urban Model (ETU)

Tap delay	Relative power
0	-1.0
50	-1.0
120	-1.0
200	-0.0
230	-0.0
500	-0.0
1600	-3.0
2300	-5.0
5000	-7.0

The ETU70 multipath fading propagation condition is defined by a combination of a multi-path delay profile and a maximum Doppler frequency f_D of 70 Hz, where all taps have classical Doppler spectrum. The power delay profile of ETU70 is listed in Table 5.6. The mean delay and RMS delay spread are 0.5612 μs and 0.9909 μs respectively.

5.3 Simulation Results

In our simulation, unless especially specified, for H_0 hypothesis we run the channel realisation 10000 times to find a threshold s.t. $P_{fa} \leq 1\%$ and for H_1 hypothesis, at each SNR point we run channel realization 1000 times to get P_d. Here we define our P_{fa} and P_d as follows:

- P_{fa}: probability of erroneous detection of the preamble when the preamble is not present.

- P_d: probability of detection of the preamble when the preamble is present.

The erroneous detection consists of several error cases: detecting different preamble than the one that was sent, not detecting a preamble at all, or correct preamble detection but with wrong timing estimation. Here we discuss the wrong timing estimation definition.

The conventional detector is to find the strongest path and get its timing and the common definition of wrong timing estimation of conventional detector is that if the estimation error of the strongest path is larger than a predefined period. The strongest path for the timing estimation error refers to the strongest path in the power delay profile. However, in multipath channel, our GLRT detection is to find a $\widehat{\theta}$ s.t. the first L taps of $\widehat{\mathbf{h}}'$ yield the biggest energy. Therefore the function of $\widehat{\theta}$ is not to find the strongest path. We define the wrong timing estimation for our detector if $\widehat{\theta}$ exceeds θ_{max}. We consider two cases for our GLRT detector— solving FCFO and not solving FCFO.

5.3.1   Performance under AWGN channel

First, we consider the AWGN channel. Even if we consider a multipath formulation, it is still interesting to see our GLRT performance under AWGN channel condition. Assume we know the channel model is AWGN and hence set $L = 1$ in GLRT detector. We simulate for $\varepsilon = 0$, and 0.5, which are less than 1. Therefore, we set the ICFO search range to 0. Theoretically, $\widehat{\varepsilon}_F$ should be able to recover the effect of ε and hence has a better P_d performance. Figure 5.1 shows the P_d performance for $\varepsilon = 0$, and 0.5. Note that when $L = 1$ the not solving FCFO case reduces to the conventional detector case. We find that the solving FCFO case underperforms the not solving FCFO case. This is not expected because compensating FCFO should have some performance gain. To investigate, we plot the histograms of $\widehat{\varepsilon}_F$ for SNR= -40, -30, -20, -10, and 0 dB when $\varepsilon = 0$ in Figure 5.2. We find the $\widehat{\varepsilon}_F$ is really bad in the SNR range of $[-40, -20]$ dB. First let us try to see the P_d performance if we assume a perfect estimation of FCFO. This is shown in Figure 5.3. We see the knowing exact $\widehat{\varepsilon}_F$ may significantly outperform the not solving FCFO case.

We might wonder why a bad estimation of FCFO leads to a bad P_d performance. The H_1 hypothesis is simulated 10000 times. Consider the example where $\varepsilon = 0.5$ and suppose

we get $\widehat{\varepsilon}_F = -0.9$. After compensating the (supposed) FCFO, the effective CFO now would be $\varepsilon - \widehat{\varepsilon}_F = 1.4$, while our ICFO search range is 0. That is why the solving FCFO case suprisingly underperforms the not solving FCFO case. We can say that the FCFO estimation error will enlarge the CFO range that needs to be seached for. Therefore, We need to set the ICFO search range to $[-1, 1]$ to get a good P_d performance. In addition, we should assume the FCFO range as $(-0.5, 0.5)$ even if the actual FCFO is in the range of $(-1, 1)$ for the reason that this assumption will make the estimation error of FCFO smaller. We will apply modulo operation to let $\widehat{\varepsilon}_F$ be in the range of $(-0.5, 0.5)$. Now we investigate what is the CFO range that assuming the FCFO range to be $(-0.5, 0.5)$ can detect. We notice that now the biggest estimated CFO error is 0.5 and the largest effective CFO that the ICFO search range $[-1, 1]$ can detect is 1.5 (if it is larger than 1.5, we have to set ICFO search range to $[-2, 2]$ to get a good detection performance). Therefore, the biggest CFO that this detector can work properly is $|\varepsilon| < 1$. Figure 5.4 shows the results when we set the ICFO search range to $[-1, 1]$ and the FCFO range to $(-0.5, 0.5)$.

We apply this kind of ICFO search range and FCFO range in subsequent simulations. We found that with solving FCFO, the P_d performance stays the same for $\varepsilon = 0, 0.25, 0.5$. For the not solving FCFO case, the P_d performance will change with ε, with the worst case happening when $\varepsilon = 0.5$. We can say that although solving FCFO cannot have the best P_d performance but it is guaranteed that we can have a robust P_d performance against ε.

In practice we do not know the channel type beforehand. It is of interest to test the P_d performance when there is a mismatch between the actual CIR length and assumed CIR length L. Figure 5.5 shows the P_d performance under AWGN channel for different values of L. We simulate H_1 10000 timesat each SNR point. Notice that from now on we define the P_d using the original definition (not the TS 36.141 definition). We can see that P_d will not differ much even when $L = 100$ and there is a clear performance drop when $L = 300$. We

can conclude that there is a certain amount of tolerance of the CIR length for this GLRT detector.
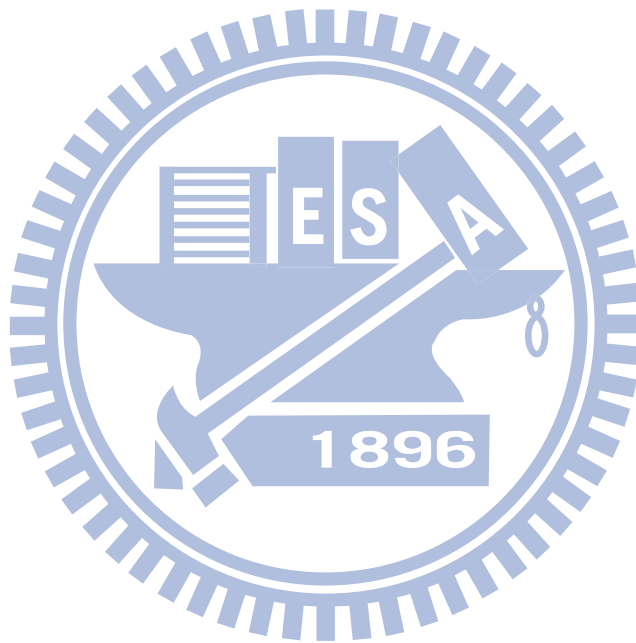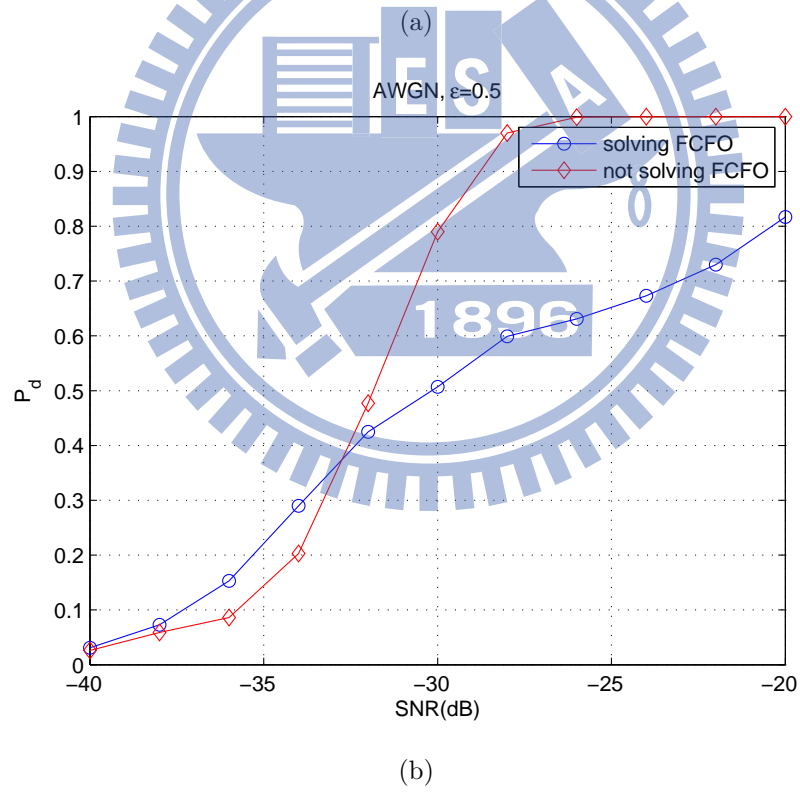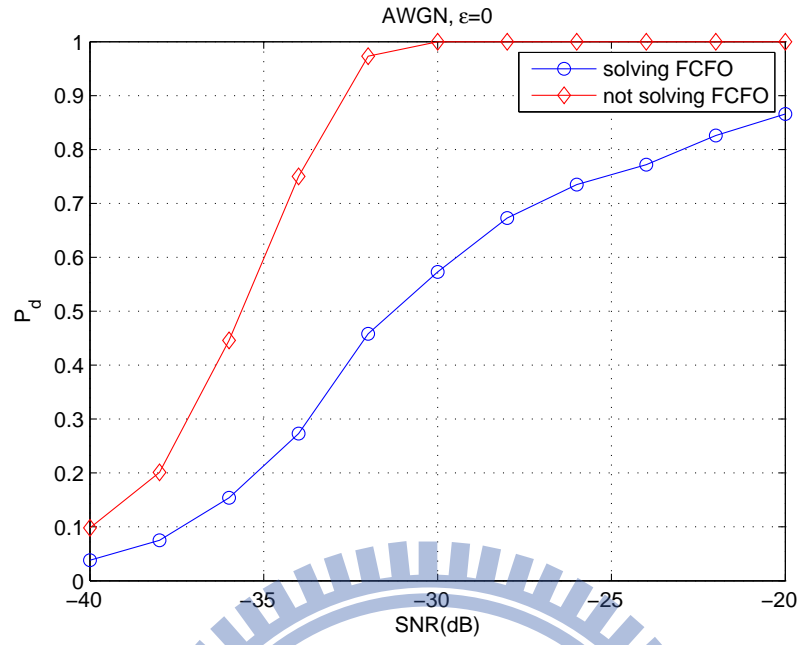
Figure 5.1: P_d performance for solving FCFO and not solving FCFO under AWGN channel for (a) $\varepsilon = 0$ and (b) $\varepsilon = 0.5$.
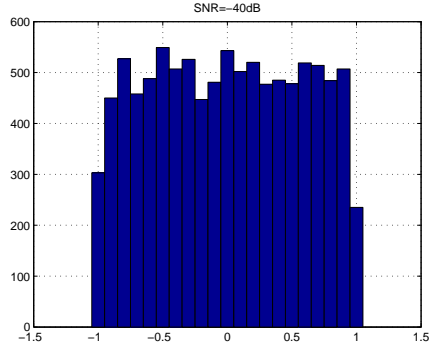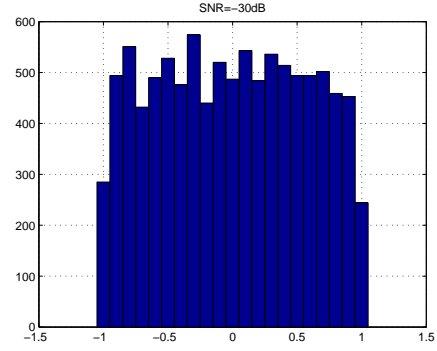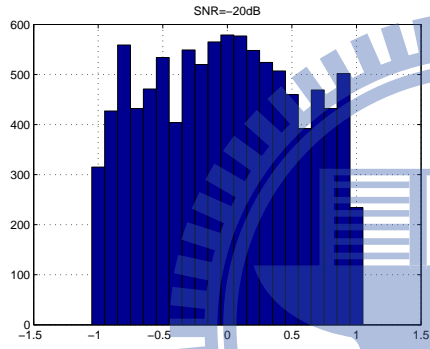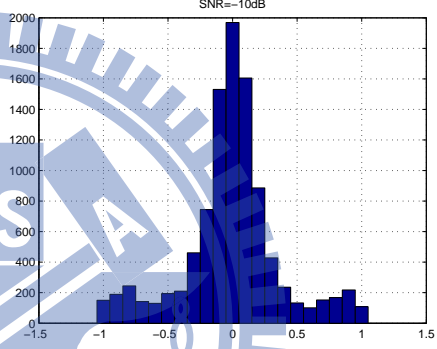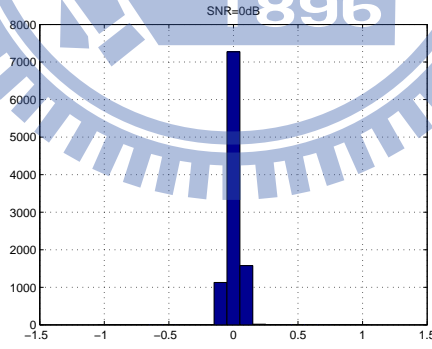
Figure 5.2: Histogram of $\widehat{\varepsilon}_F$ when $\varepsilon = 0$ for SNR = (a) -40 dB, (b) -30 dB, (c) -20 dB, (d) -10 dB, and (e) 0 dB.
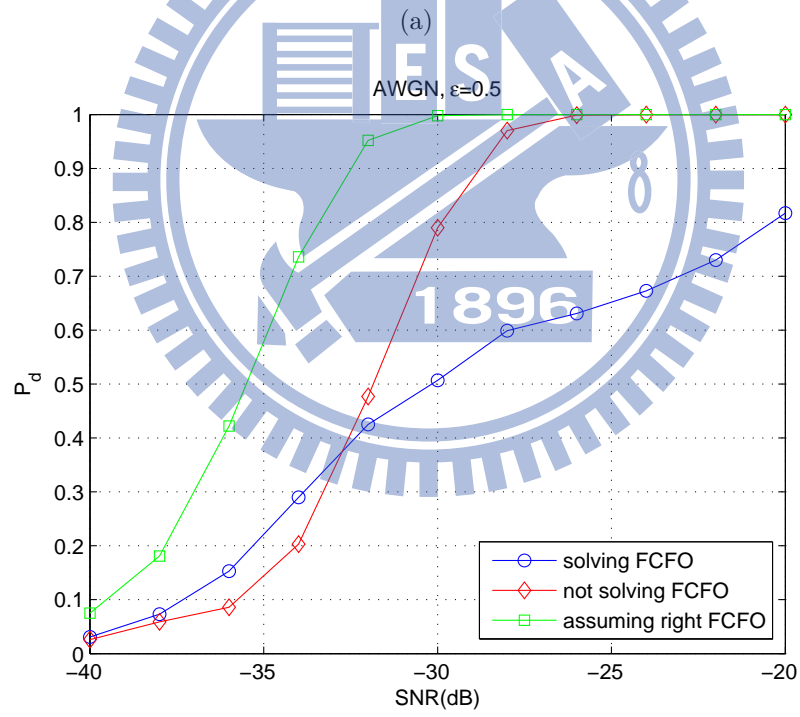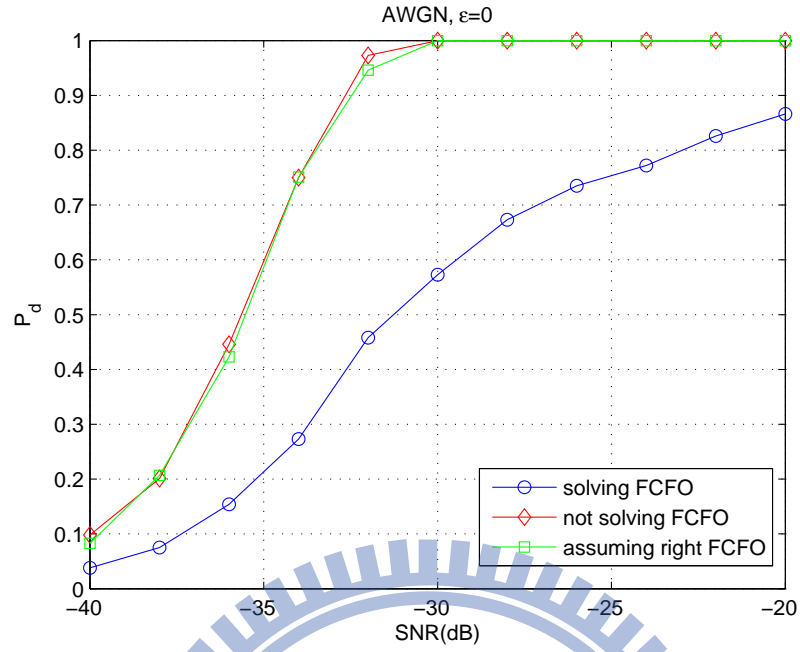
Figure 5.3: P_d performance for solving, not solving FCFO, and assuming a perfect estimation of FCFO under AWGN channel for (a) $\varepsilon = 0$ and (b) $\varepsilon = 0.5$.
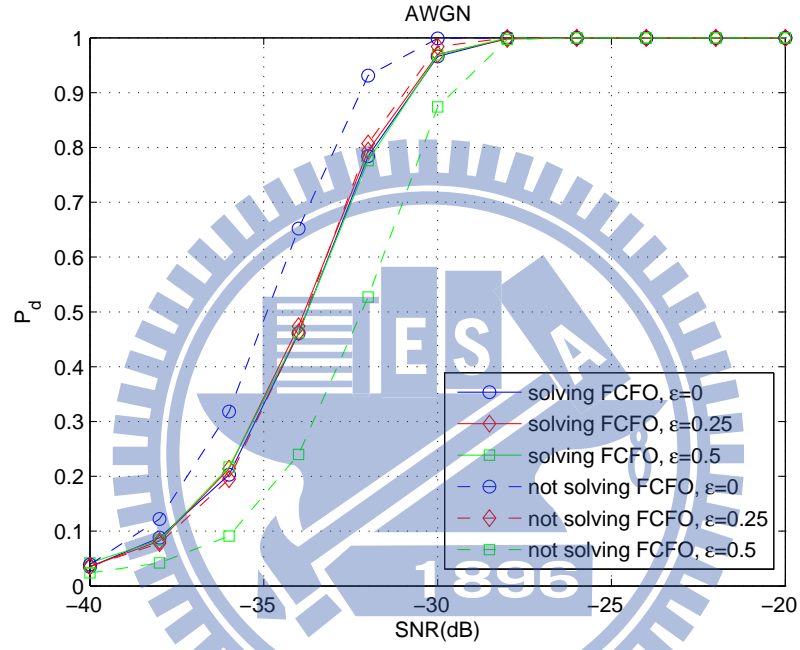
Figure 5.4: P_d performance for solving and not solving FCFO under AWGN channel for different values of ε after adjusting the ICFO search range and FCFO range.

(a)

(b)
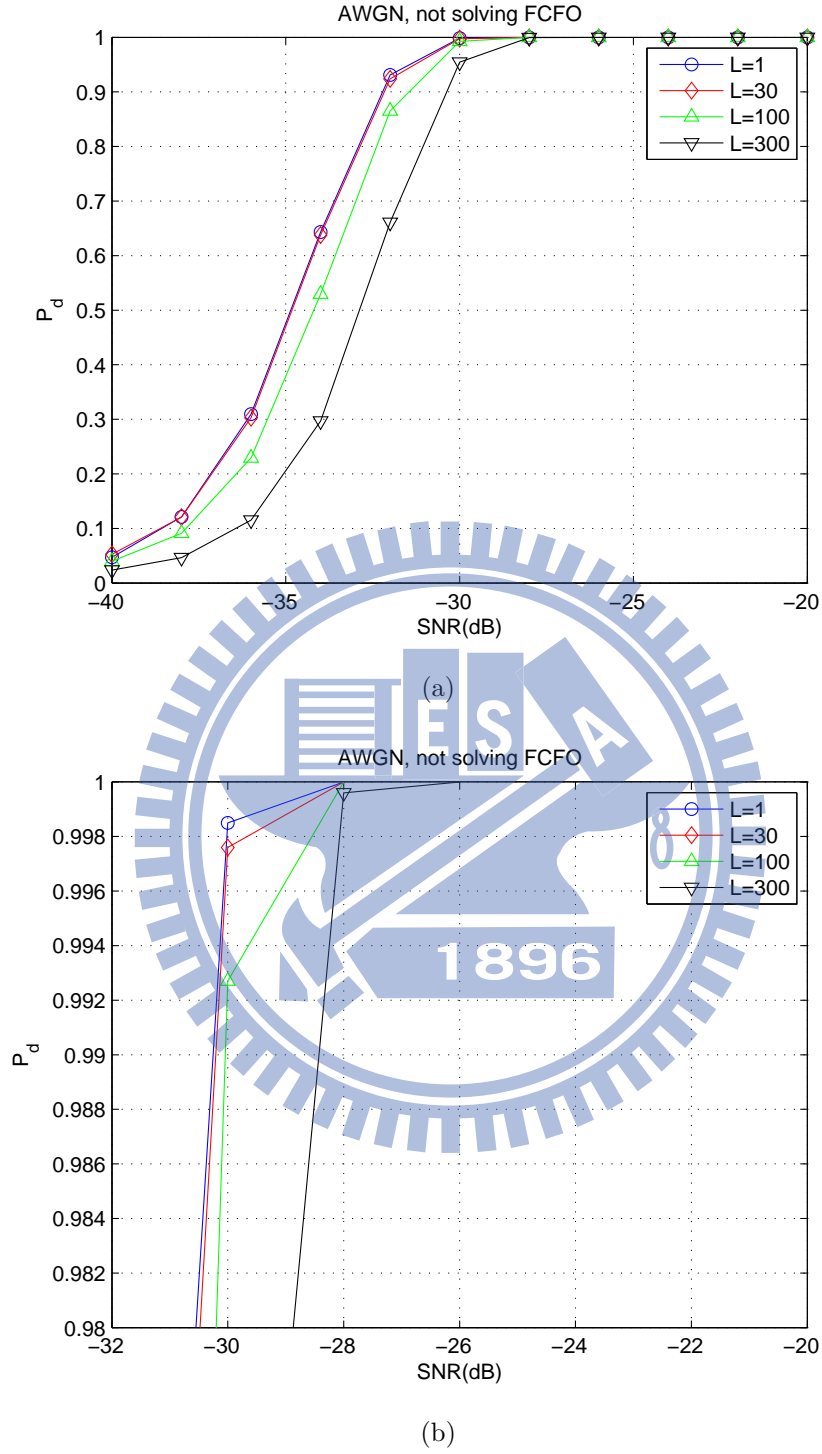
Figure 5.5: P_d performance for not solving FCFO under AWGN channel for $\varepsilon = 0$ with different values of L. (b) is a zoom-in plot of (a).

5.3.2 Performance anaysis against TS 36.141

Now we test our GLRT to see if it satisfies the minimum requirement set forth in the LTE-A specification. Figure 5.6 shows the comparison of P_d performance for the solving FCFO and not solving FCFO cases with different CFO under AWGN channel model. The H_0 is simulated 100000 times to find a threshold such that $P_{fa} \leq 1\%$ and H_1 is simulated 10000 times at each SNR point. Notice that setting ICFO search range to $[-1, 1]$ means the high speed mode and since our detector can only operate properly for high speed mode, here we only generate the results of high speed mode to compare with the TS 36.141. However, Table 5.2 only shows the cases with number of received antennas equal to 2 or 4. Since we only consider the situation with one receiver antenna, in order to compare with the TS 36.141, we assume for preamble format 0 and single antenna the SNR at CFO = 0 is -11.0 dB and the SNR at CFO = 0.5 (625 Hz) is -9.6 dB. Then we apply the SNR correction factor in Table 5.3. Our channel bandwidth is 20 MHz and thus we need to add -12.34 dB to the SNR. Therefore, the SNR after correction is -23.34 dB and -21.94 dB for CFO $= 0$ and CFO $= 0.5$ respectively. Notice that we already set the threshold s.t. $P_{fa} \leq 0.1\%$ to satisfy the minimum requirement. For the solving FCFO case, Figure 5.6(b) shows that the SNR at $P_d = 0.99$ is -28.1 dB for both $\varepsilon = 0$ and 0.5. That is, P_d is definitely greater than 0.99 when SNR$= -23.34$ dB for $\varepsilon = 0$ or SNR$= -21.94$ dB for $\varepsilon = 0.5$. Therefore, our GLRT satisfies the minimum requirement.

Figure 5.7 shows the P_d performance for the solving FCFO case with CFO$= 0.216$ (270 Hz) and different L. The H_0 is simulated 100000 times to find a threshold such that $P_{fa} \leq 1\%$ and H_1 is simulated 10000 times at each SNR point. The ETU RMS delay spread is 30 (normalized by the sampling period and rounded to integer) and the longest path delay is 153 (normalized by the sampling period and rounded to integer). We will compare the results of $L = 1$, $L =$ RMS delay spread, $L = 2$ times RMS delay spread, and $L =$ the longest path.

We assume that SNR for preamble 0 and single antenna is -2.4 dB. After applying the SNR correlation factor, the SNR after correction is -14.74 dB. First, we see the $L = 153$ curve does not attain high P_d even if the SNR is nigh. That is because the function of the GLRT is not to find the strongest path but the strongest L window energy. When we set the L too big, we might face the problem that the timing offset between the L window and the strongest path exceeds the defined value and then causes a bad P_d performance. For the case of $L = 1$, we find that P_d does not go up to 0.99 but it is reasonable since for CFO $= 0.216$ the solving FCFO case underperforms the not solving FCFO case and the minimum requirement is for the conventional detector which does solve for FCFO. When we set $L = 30$ and $L = 60$, we can see that the required SNR is less than -26 dB.

Figure 5.8 shows that the P_d performance for the not solving FCFO case with CFO $= 0.216$ (270 Hz) and different L. The H_0 is simulated 100000 times to find a threshold such that $P_{fa} \leq 1\%$ and H_1 is simulated 10000 times at each SNR point. Again, we see P_d of $L = 153$ does not attain a high P_d. And for $L = 1$, we see that the SNR at $P_d = 0.99$ is -18 dB, which is smaller than -14.74 dB and hence satisfies the minimum requirement. For $L = 30$ and $L = 60$, we see an at least 8 dB performance gain at $P_d = 0.99$. Therefore, from Figures 5.7 and 5.8, we suggest that assuming a proper L can have a big performance gain.

(a)

(b)
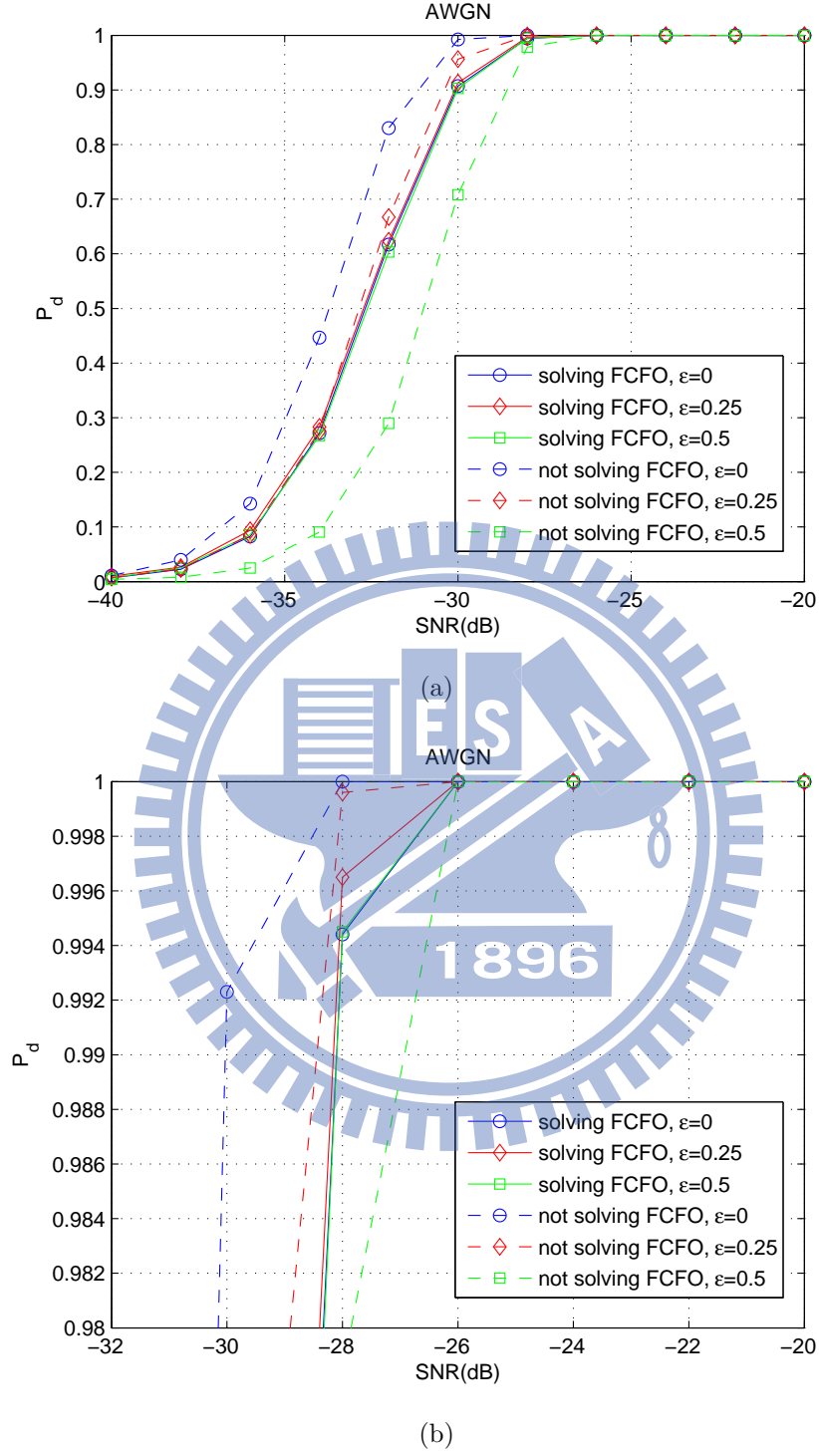
Figure 5.6: P_d performance for solving and not solving FCFO under AWGN channel for different values of ε with P_d under the definition of TS 36.141. (b) is a zoom-in plot of (a).
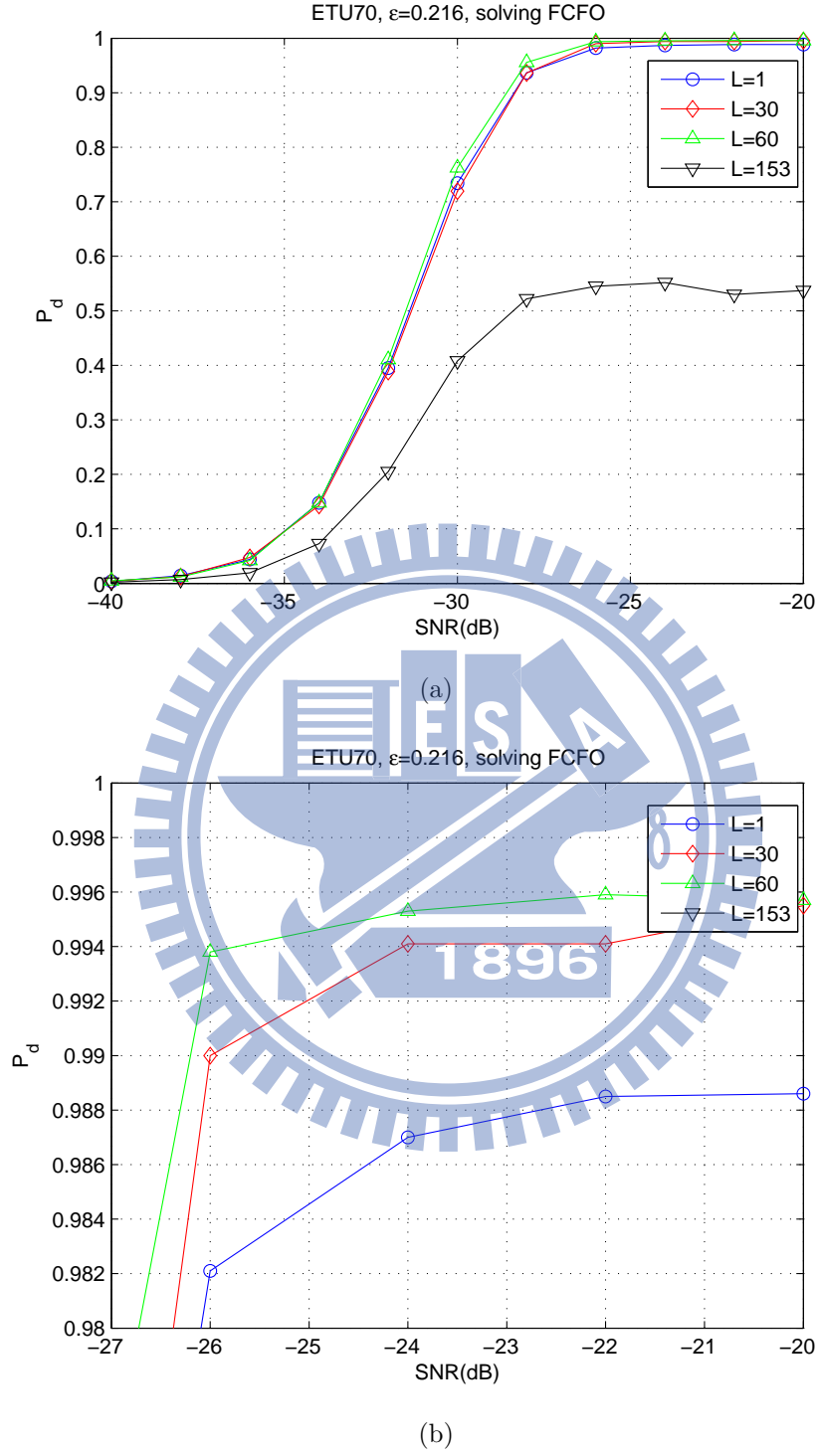
Figure 5.7: P_d performance for solving FCFO under ETU70 channel for $\varepsilon = 0.216$ with P_d under the definition of TS 36.141. (b) is a zoom-in plot of (a).

(a)

(b)
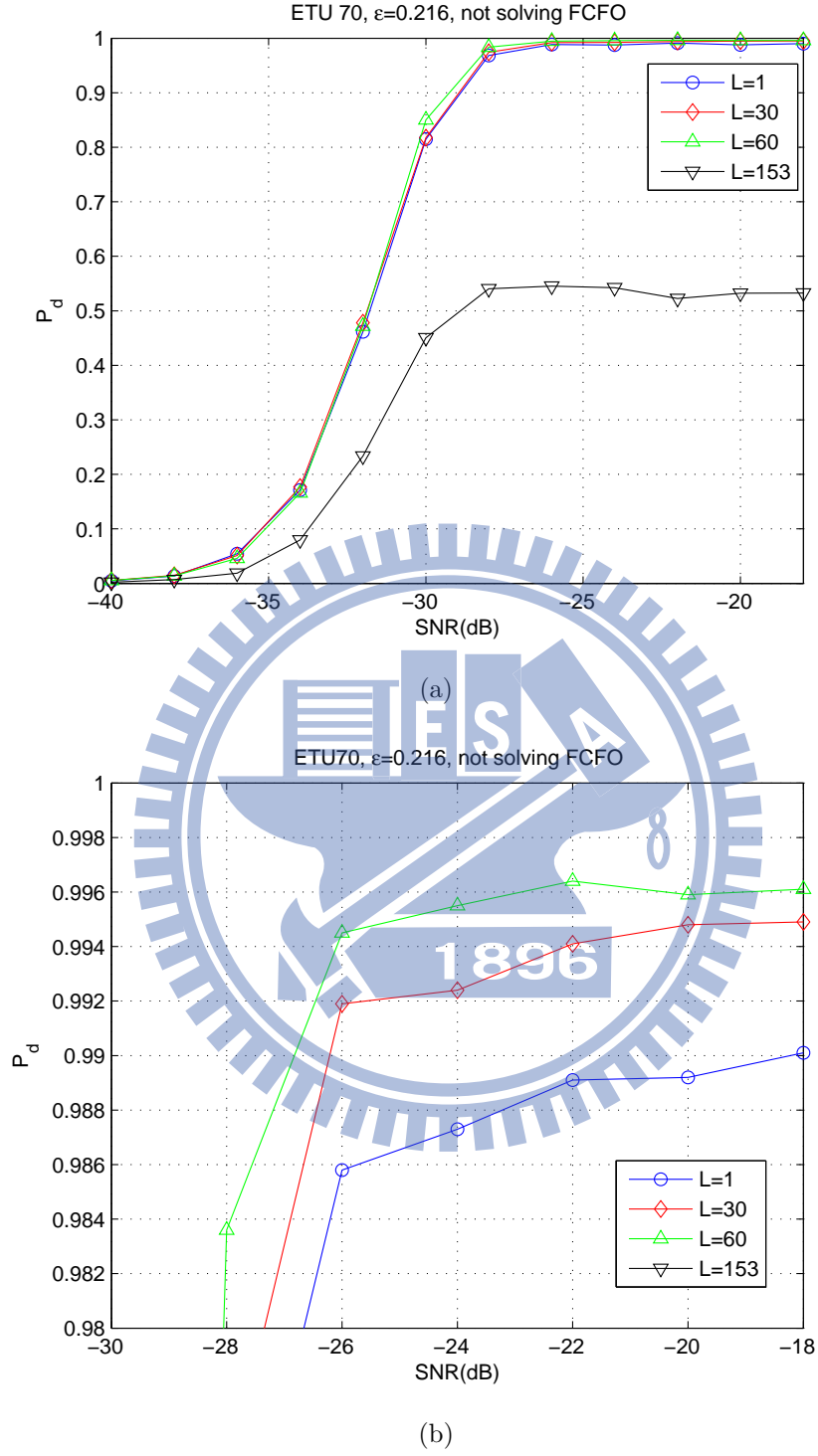
Figure 5.8: P_d performance for not solving FCFO under ETU70 channel for $\varepsilon = 0.216$ with P_d under the definition of TS 36.141. (b) is a zoom-in plot of (a).
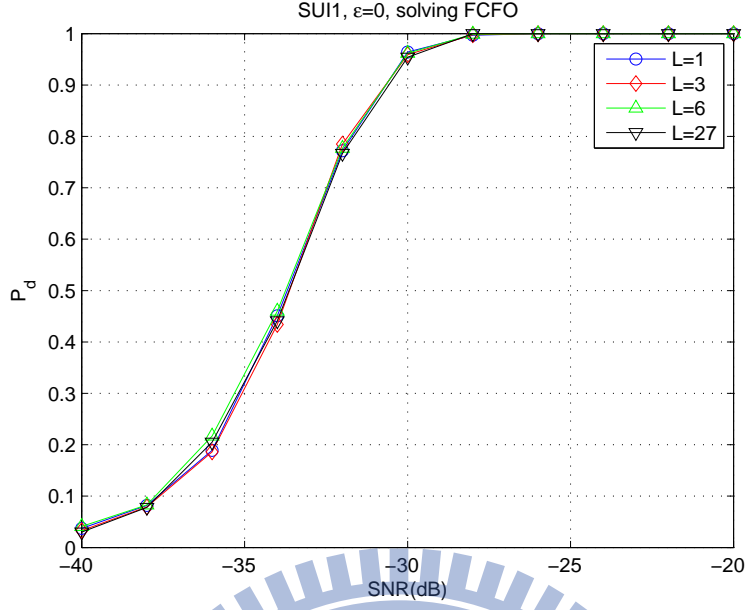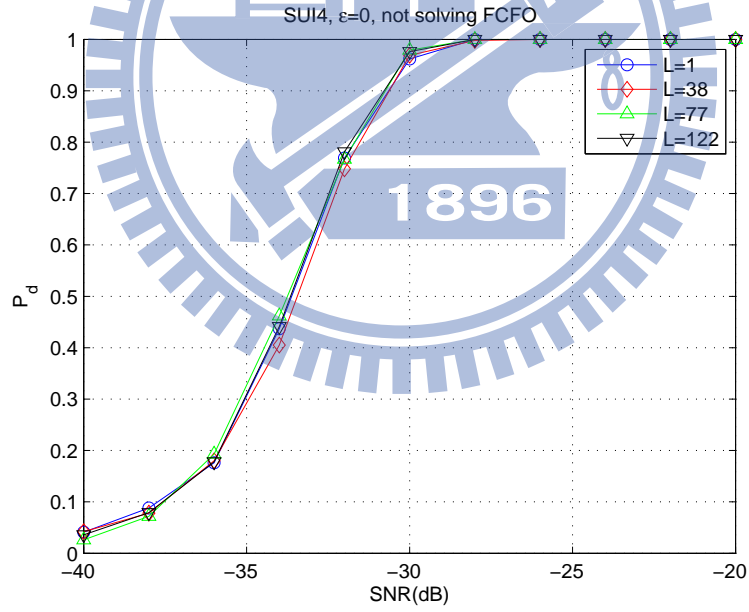
Figure 5.9: P_d performance for solving FCFO under SUI1 channel for $\varepsilon = 0$ with different values of L.

5.3.3 Performance under SUI channel

Now we test the GLRT detector for SUI channels under different CFO and CIR length assumptions. Figures 5.9–5.14 show the P_d performance for the solving FCFO case for different values of L at zero CFO. The four values of L are 1, RMS delay spread (normalized by the sampling period and rounded to integer), 2 times RMS delay spread (normalized by the sampling period and rounded to integer), and the maximum CIR length. For the SUI1–SUI4 channels, we do not see a big difference in performance for different L. For SUI5 and SUI6, however, we find a clear gap for different values of L. For $L = $ maximum CIR length, the P_d underperforms the other cases in the low SNR region and then outperforms the others in the high SNR region. And according to the TS 36.141 minimum performance requirement, what we care is when $P_d = 0.99$. So in these results, we suggest to use $L = $ maximum CIR length.
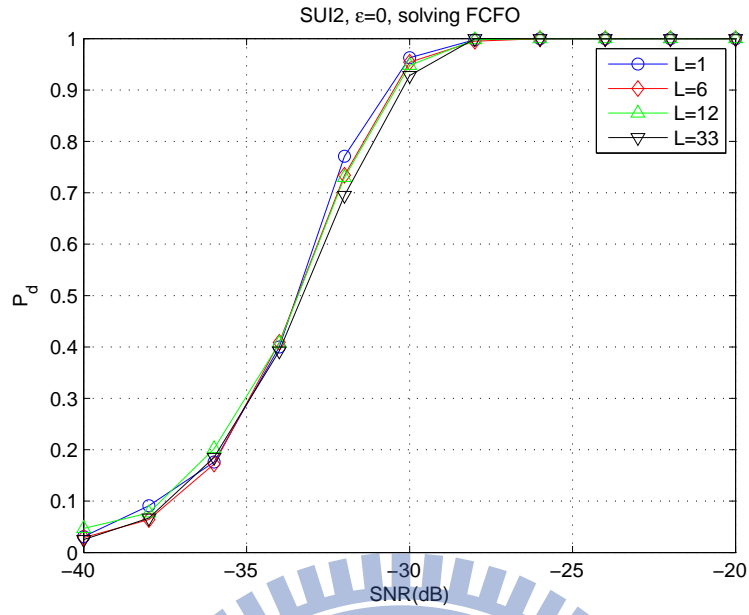
Figure 5.10: P_d performance for solving FCFO under SUI2 channel for $\varepsilon = 0$ with different values of L.
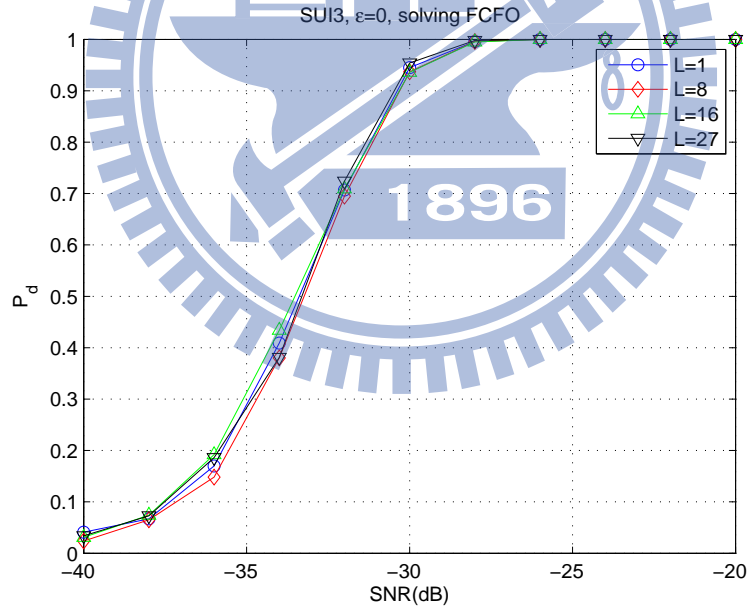
Figure 5.11: P_d performance for solving FCFO under SUI3 channel for $\varepsilon = 0$ with different values of L.
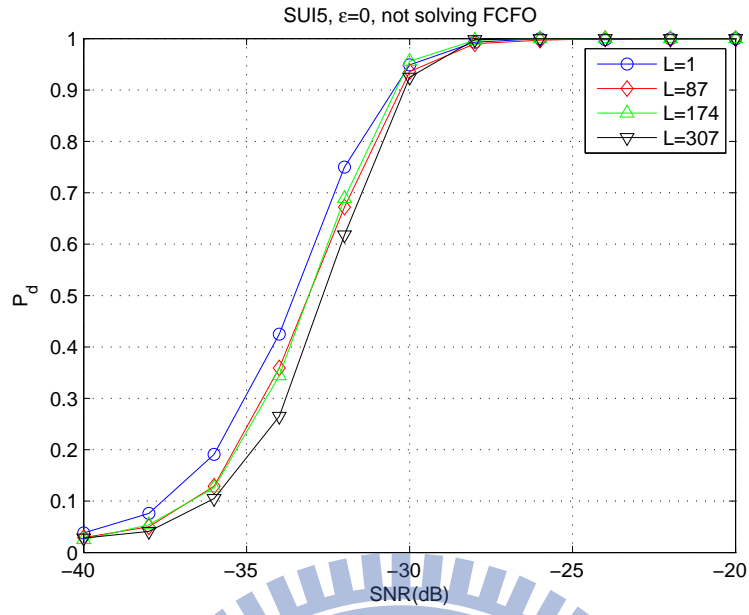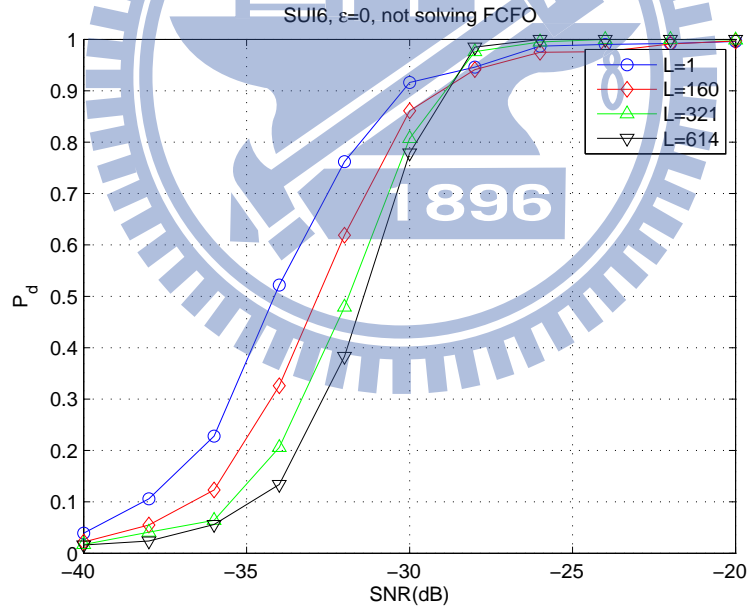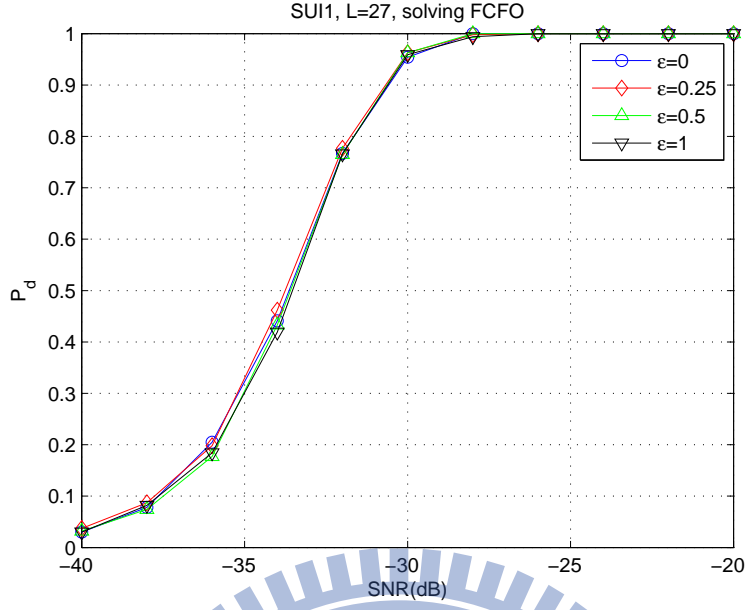
61
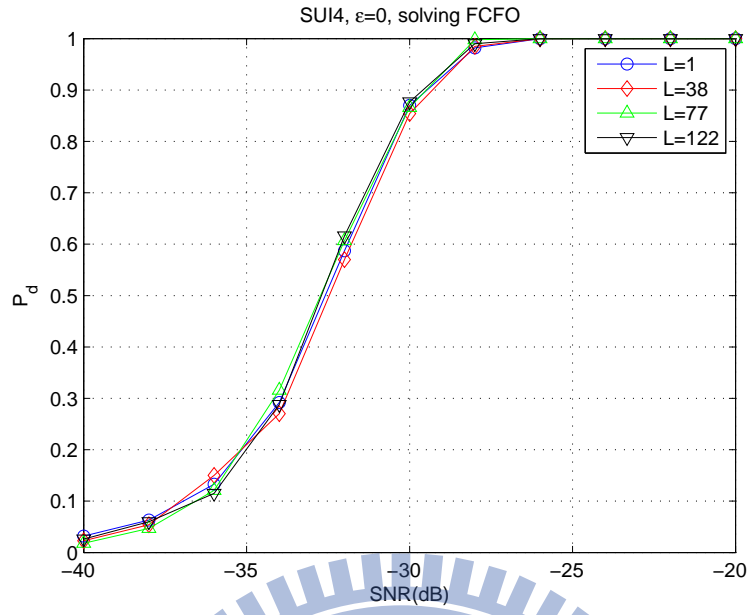
Figure 5.12: P_d performance for solving FCFO under SUI4 channel for $\varepsilon = 0$ with different values of L.
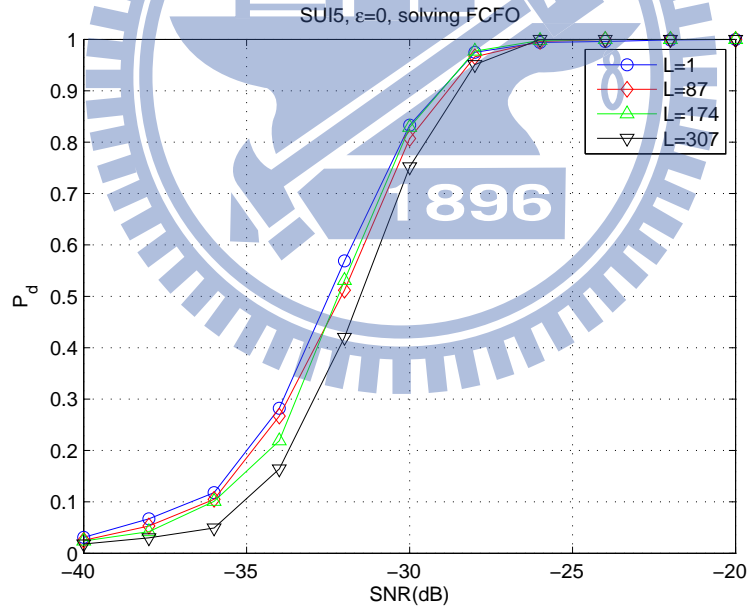
Figure 5.13: P_d performance for solving FCFO under SUI5 channel for $\varepsilon = 0$ with different values of L.
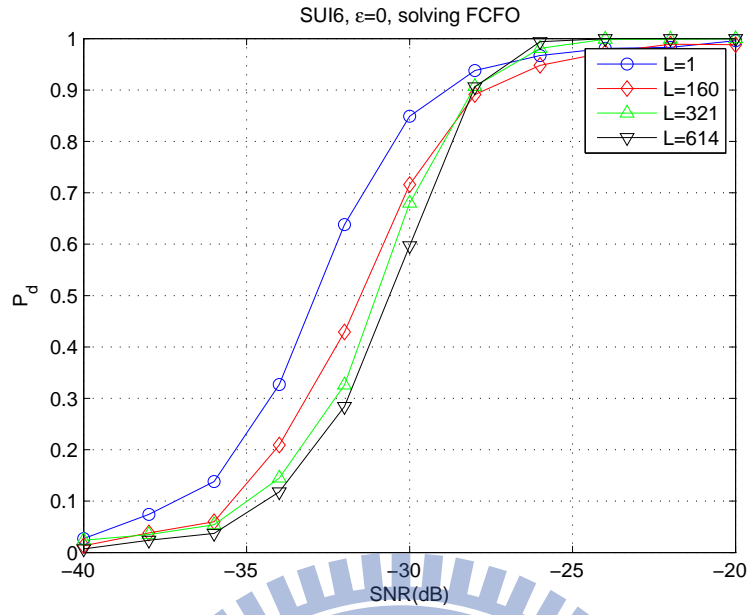
Figure 5.14: P_d performance for solving FCFO under SUI6 channel for $\varepsilon = 0$ with different values of L.

Figures 5.15–5.20 show the not solving FCFO case for different SUI channels. We see the same trend as the solving FCFO case.
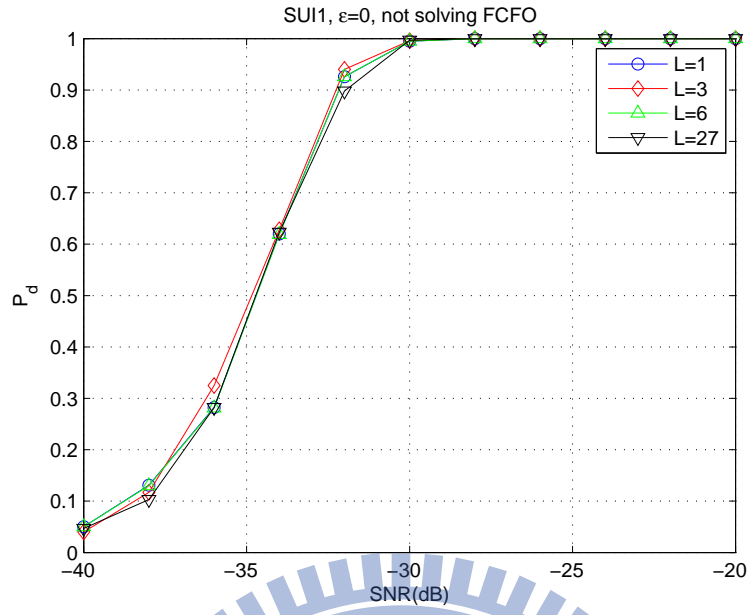
Figure 5.15: P_d performance for not solving FCFO under SUI1 channel for $\varepsilon = 0$ with different values of L.
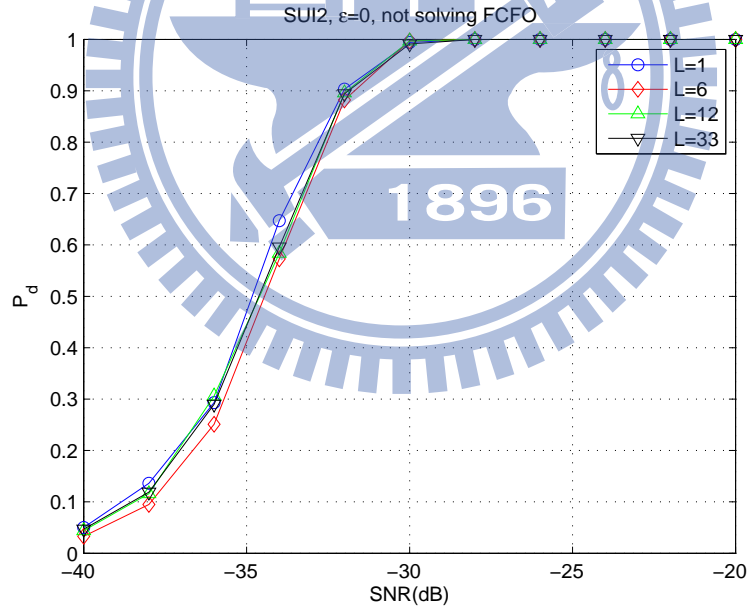
Figure 5.16: P_d performance for not solving FCFO under SUI2 channel for $\varepsilon = 0$ with different values of L.
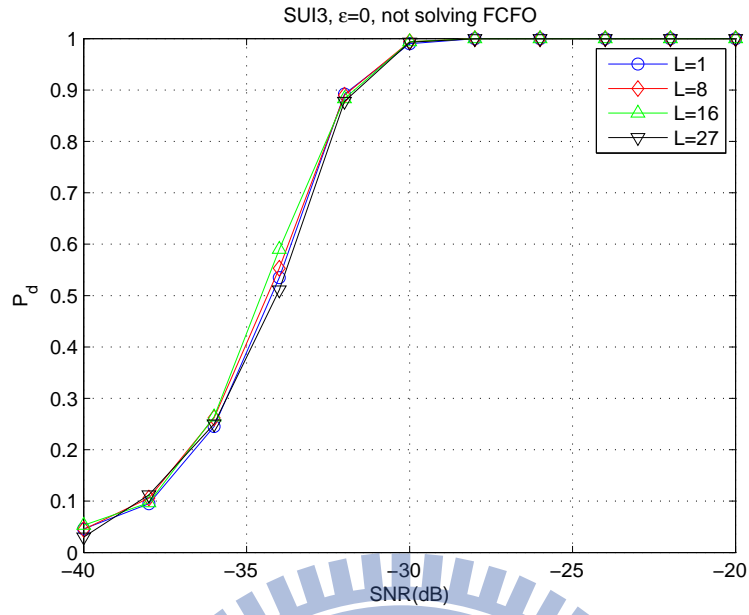
Figure 5.17: P_d performance for not solving FCFO under SUI3 channel for $\varepsilon = 0$ with different values of L.

Figure 5.18: P_d performance for not solving FCFO under SUI4 channel for $\varepsilon = 0$ with different values of L.

65

Figure 5.19: P_d performance for not solving FCFO under SUI5 channel for $\varepsilon = 0$ with different values of L.

Figure 5.20: P_d performance for not solving FCFO under SUI6 channel for $\varepsilon = 0$ with different values of L.

Figure 5.21: P_d performance for solving FCFO under SUI1 channel with $L = 27$ for different values of ε.

Figures 5.21–5.26 show the P_d performance for the solving FCFO case for different CFO values. It is observed that under multipath channels, P_d still exhibits a robust performance, not affected by CFO.

Figures 5.27–5.32 show the P_d performance for the not solving FCFO case for different CFO values. It is observed that under multipath channels, like what we observed in AWGN channel, P_d will vary according to CFO with the worst case happening when CFO $= 0.5$.
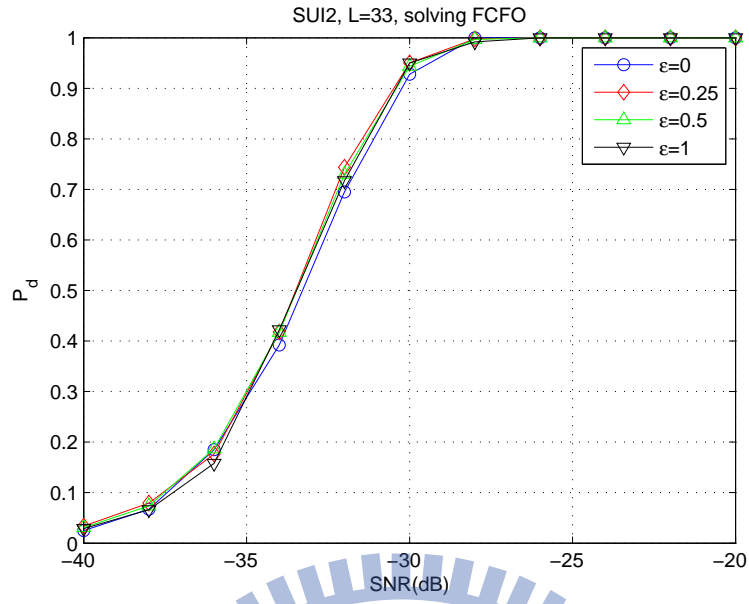
Figure 5.22: P_d performance for solving FCFO under SUI2 channel with $L = 33$ for different values of ε.
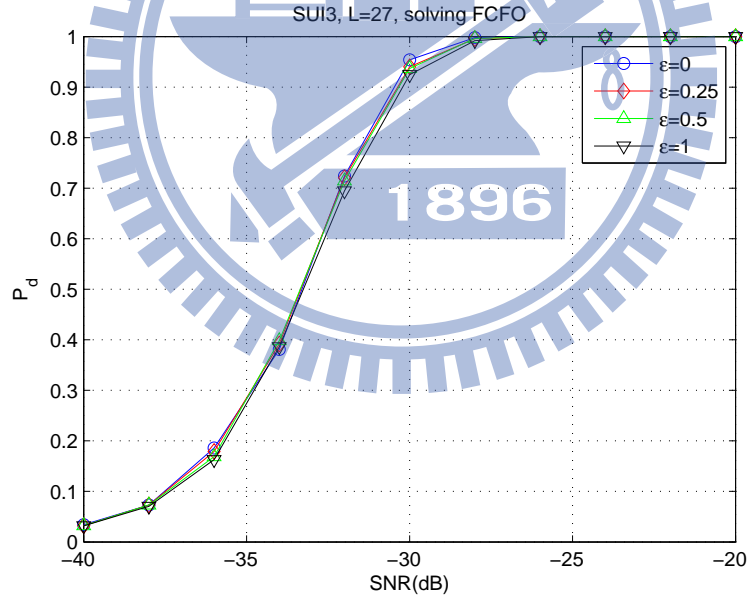
Figure 5.23: P_d performance for solving FCFO under SUI3 channel with $L = 27$ for different values of ε.
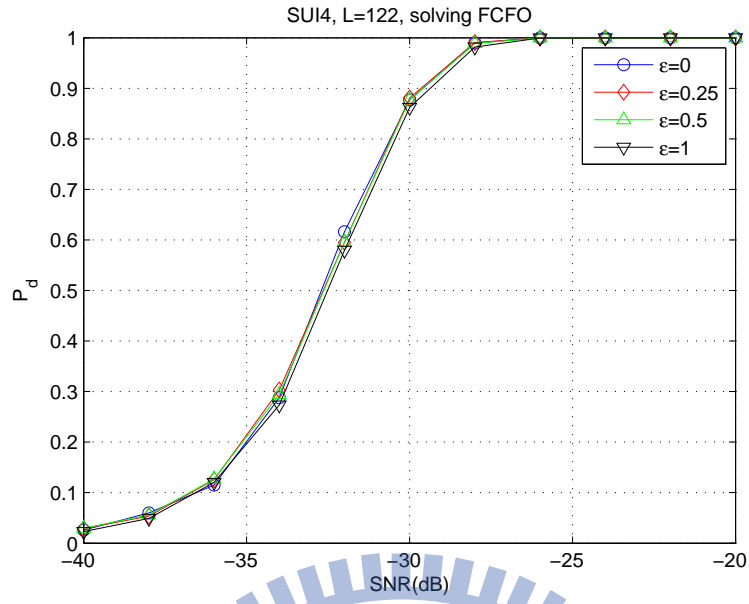
Figure 5.24: P_d performance for solving FCFO under SUI4 channel with $L = 122$ for different values of ε.
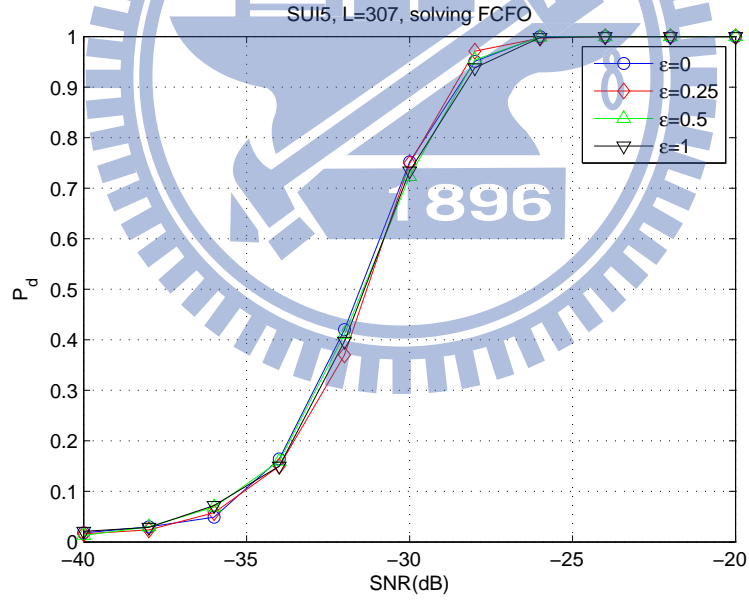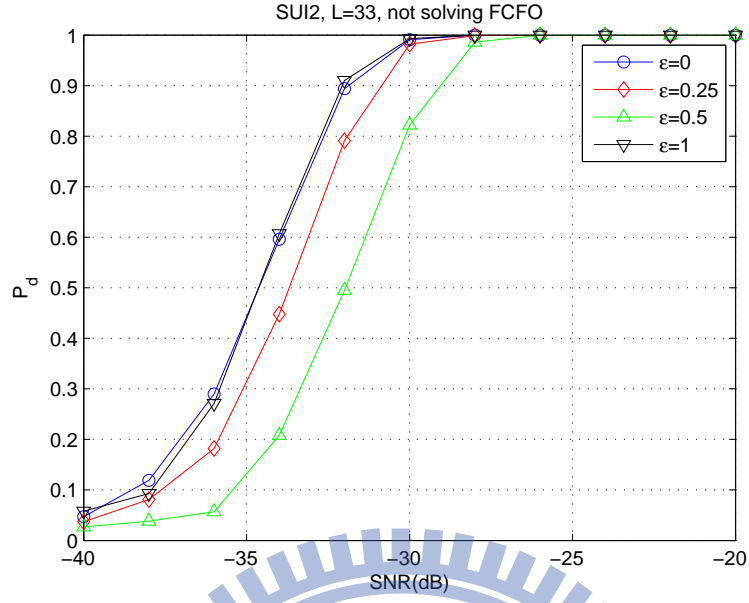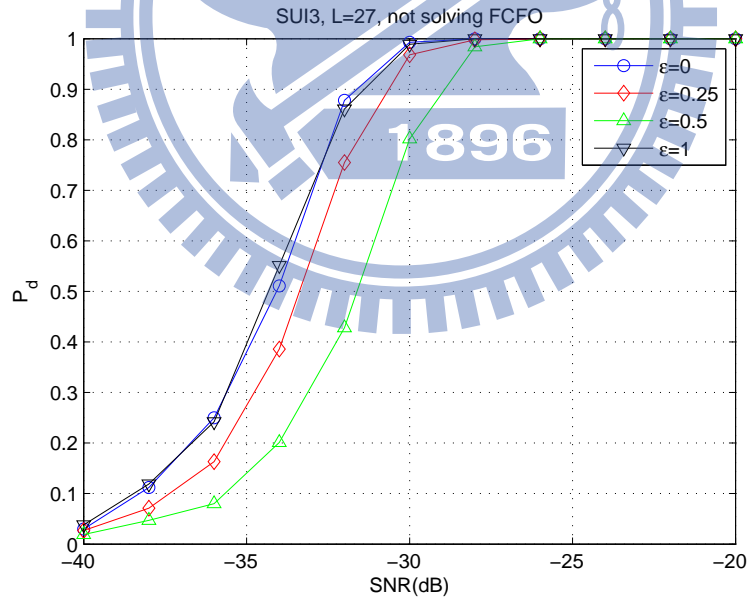

Figure 5.25: P_d performance for solving FCFO under SUI5 channel with $L = 307$ for different values of ε.
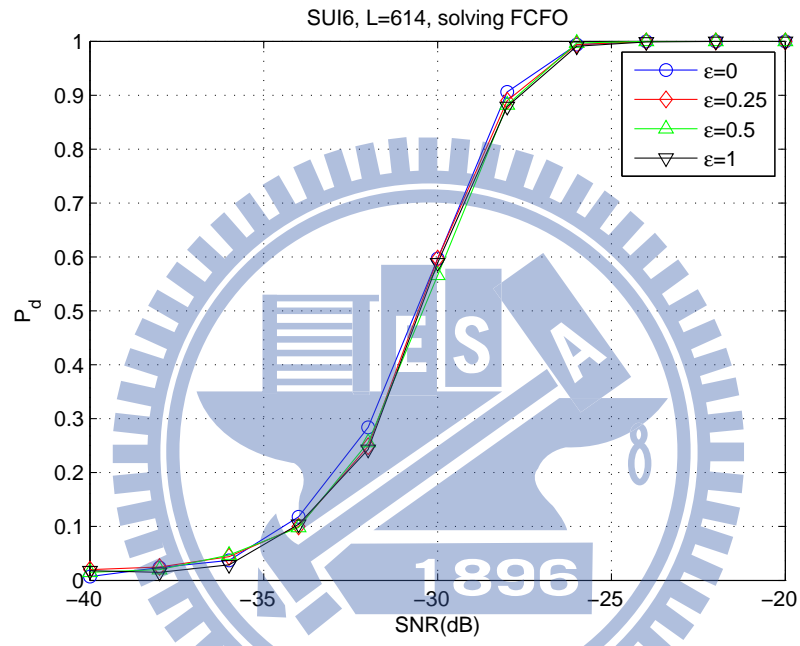
Figure 5.26: P_d performance for solving FCFO under SUI6 channel with $L = 614$ for different values of ε.
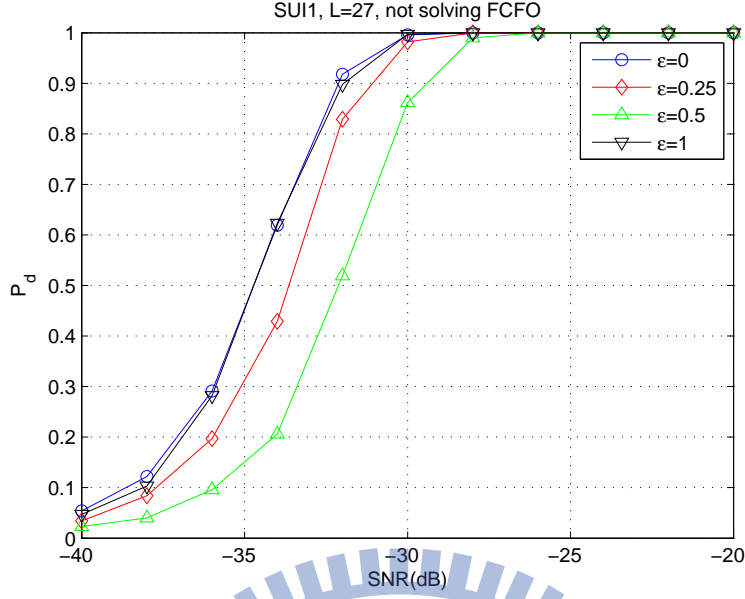
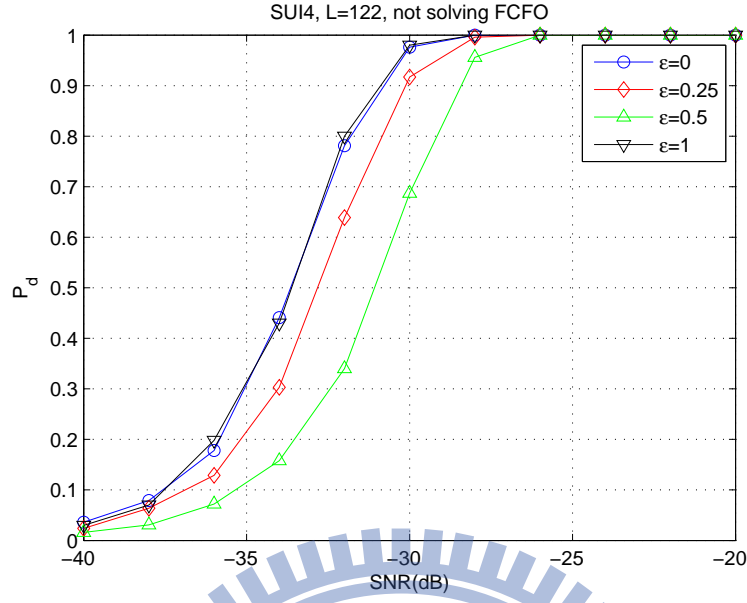Figure 5.27: P_d performance for solving not FCFO under SUI1 channel with $L = 27$ for different values of ε.

Figures 5.33–5.38 show P_{fa} and miss detection probability P_m $(1 - P_d)$ versus threshold for different SUI channel model for SNR $= 10$ dB. We simulate H_0 100000 times and H_1 100000 times. We can see that for L equal to the maximum CIR length, we get a bigger threshold range, for which P_{fa} and P_m are quite small (say around 10^{-3}). And our GLRT detector setting L equal to the maximum CIR length has an advantage of being less sensitive to threshold variation.

Figure 5.28: P_d performance for solving not FCFO under SUI2 channel with $L = 33$ for different values of ε.

Figure 5.29: P_d performance for solving not FCFO under SUI3 channel with $L = 27$ for different values of ε.

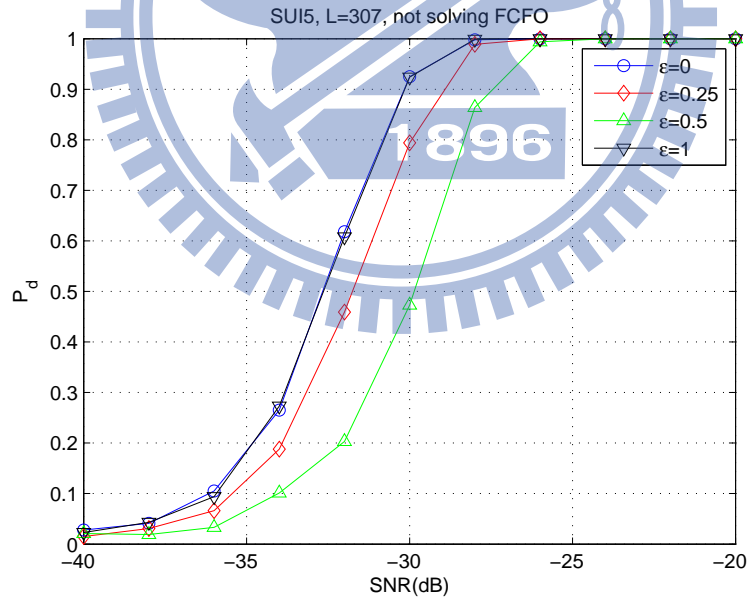Figure 5.30: P_d performance for solving not FCFO under SUI4 channel with $L = 122$ for different values of ε.

Figure 5.31: P_d performance for solving not FCFO under SUI5 channel with $L = 307$ for different values of ε.
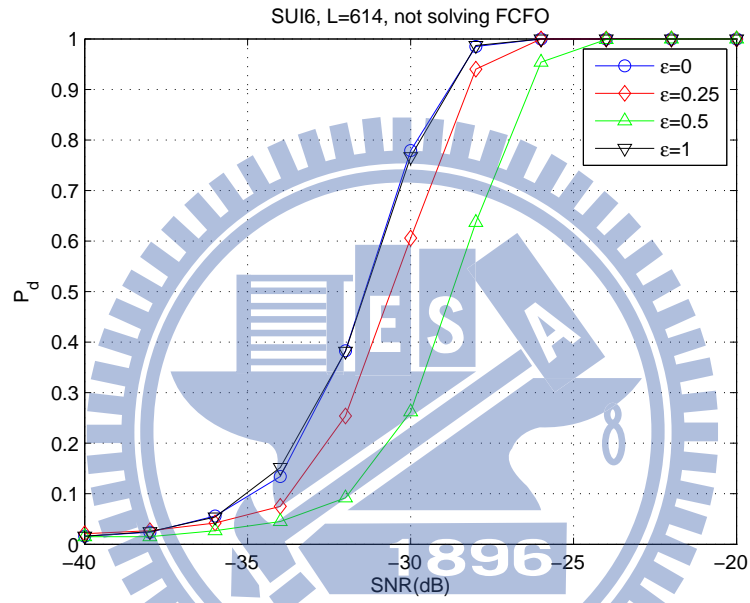
Figure 5.32: P_d performance for solving not FCFO under SUI6 channel with $L = 614$ for different values of ε.
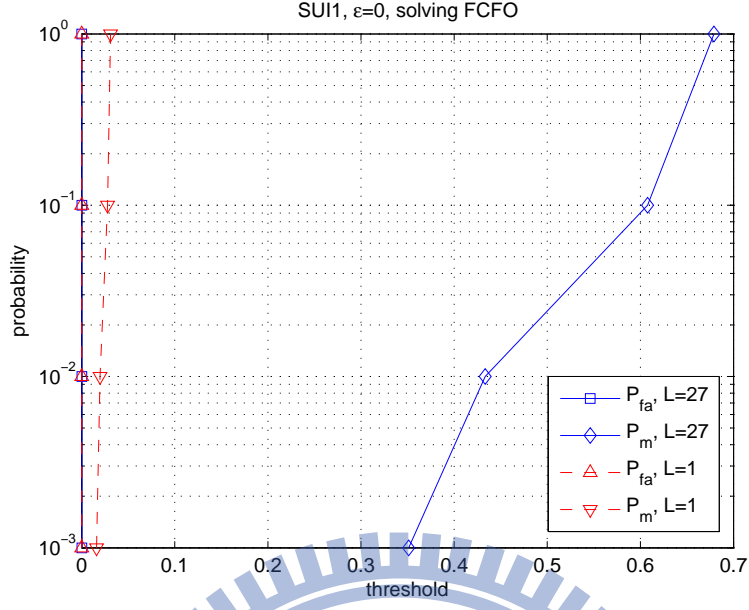
Figure 5.33: P_{fa} and P_m versus threshold under SUI1 channel with $L = 1$ and maximum CIR length for SNR = 10 dB.
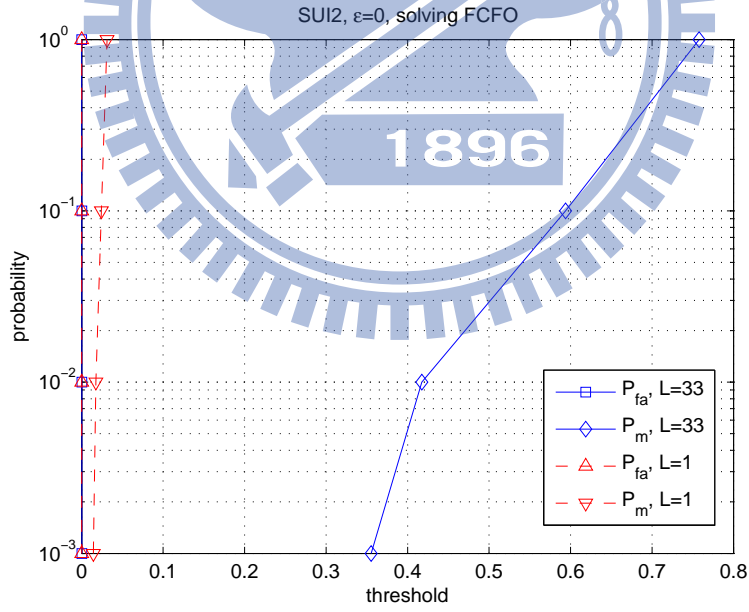

Figure 5.34: P_{fa} and P_m versus threshold under SUI2 channel with $L = 1$ and maximum CIR length for SNR = 10 dB.
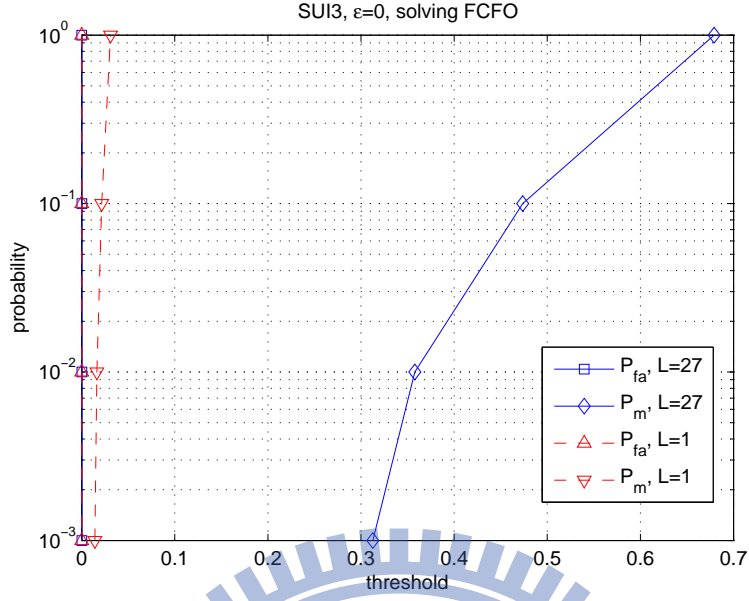
Figure 5.35: P_{fa} and P_m versus threshold under SUI3 channel with $L = 1$ and maximum CIR length for SNR = 10 dB.

Figure 5.36: P_{fa} and P_m versus threshold under SUI4 channel with $L = 1$ and maximum CIR length for SNR = 10 dB.

Figure 5.37: P_{fa} and P_m versus threshold under SUI5 channel with $L = 1$ and maximum CIR length for SNR = 10 dB.
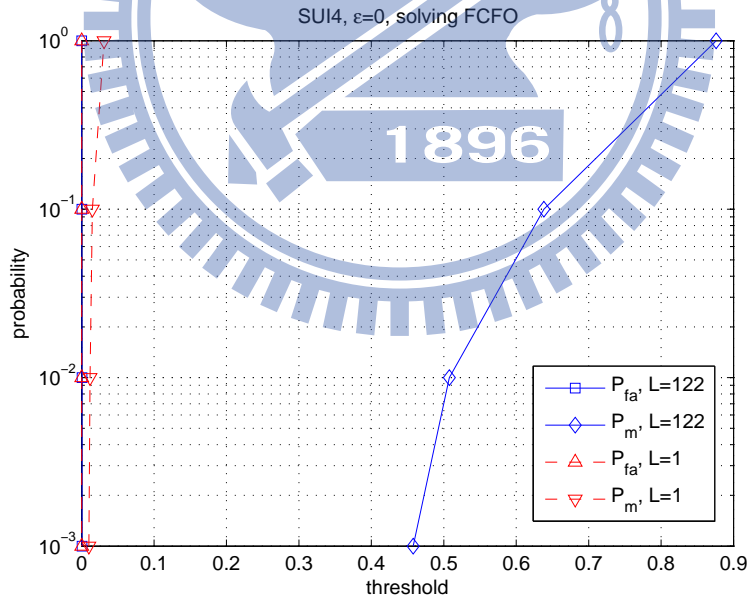

Figure 5.38: P_{fa} and P_m versus threshold under SUI6 channel with $L = 1$ and maximum CIR length for SNR = 10 dB.
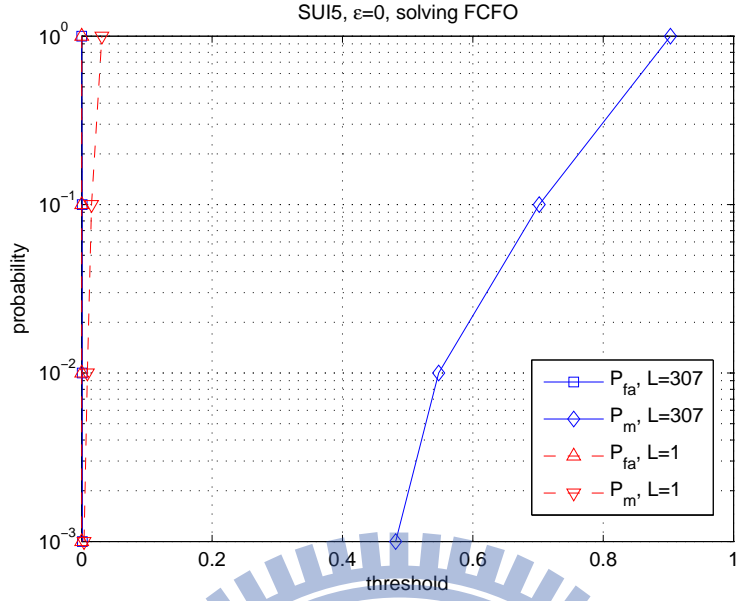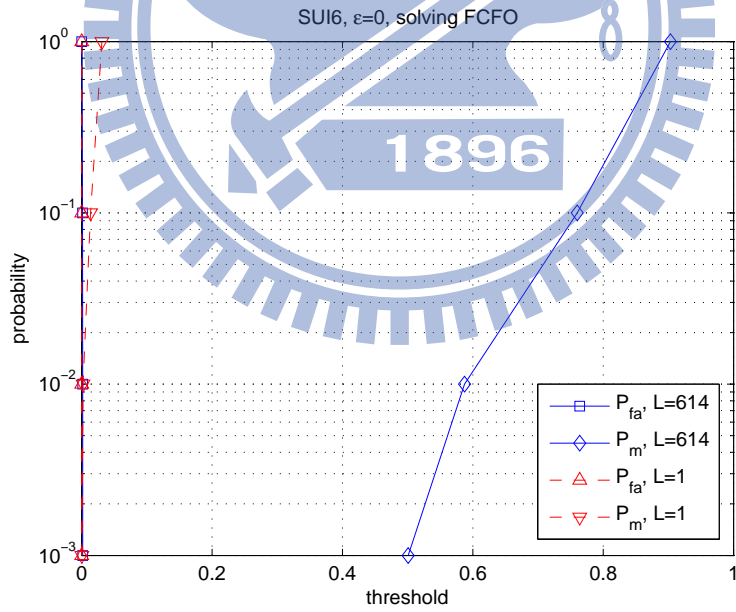
Chapter 6

# Conclusion and Future Work

6.1 Conclusion

In this thesis, we first presented the uplink and random access specification of 3GPP LTE release 10 system and constructed the transmission structure. We originally formulated the multiple preambles detection problem and because of its high computational complexity we adopted a single-user detection strategy. Second, we proposed a GLRT detector which considered the multipath channel model and CFO. In the derivation of the GLRT detector, we made some approximation to reduce the complexity and got a simple form GLRT detector.

In the simulation, we found that because the bad estimation of FCFO increased the range of effective CFO we had to set our ICFO search range larger. First, we found that by solving CFO we could have a robust P_d performance against CFO. Second, we also compared our GLRT detector to the minimum performance required in [9] and found that our detector could have a big performance gain when we set the appropriate L. Third, we found that our GLRT detector could still operate properly evn when we set CIR length smaller or larger than the actual one. Finally, in addition to the performance improvement of multiple path assumption, our GLRT detector allowed us to have a larger range of threshold values for which we could have a desired P_{fa} and P_d performance.

6.2 Future Work

There are several possible extensions for our research:

- Try to propose a better estimation method of FCFO to improve the P_d performance.

- In the case of multiple users existing, try to do some interference cancellation scheme.

- Try to derive theoretical value of P_{fa} and P_d.

- Change Matlab code to C code and try to implement on DSP.
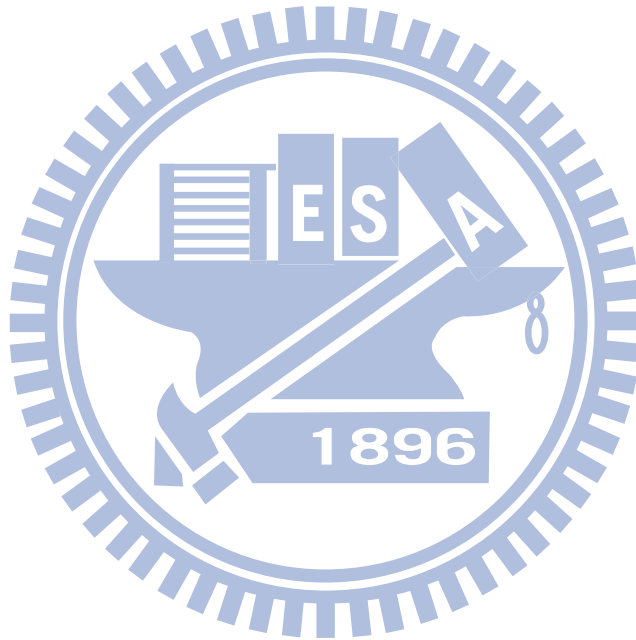
Appendix A

Multiple Hypothesis Testing

In the multiple hypothesis testing formulation, we have found the ML solution for $\mathbf{h}$ as

$$
\widehat{\mathbf{h}} = \left[\begin{bmatrix} q_1 \mathbf{B}^H \mathbf{F}^H \mathbf{D}_1^H(\theta_1) \mathbf{F} \mathbf{\Gamma}^H(\varepsilon_1) \\ \vdots \\ q_K \mathbf{B}^H \mathbf{F}^H \mathbf{D}_K^H(\theta_K) \mathbf{F} \mathbf{\Gamma}^H(\varepsilon_K) \end{bmatrix} \begin{bmatrix} q_1 \mathbf{\Gamma}(\varepsilon_1) \mathbf{F}^H \mathbf{D}_1(\theta_1) \mathbf{F} \mathbf{B} & \cdots & q_K \mathbf{\Gamma}(\varepsilon_K) \mathbf{F}^H \mathbf{D}_K(\theta_K) \mathbf{F} \mathbf{B} \end{bmatrix} \right]^{\dagger}
$$
$$
\begin{bmatrix} q_1 \mathbf{B}^H \mathbf{F}^H \mathbf{D}_1^H(\theta_1) \mathbf{F} \mathbf{\Gamma}^H(\varepsilon_1) \\ \vdots \\ q_K \mathbf{B}^H \mathbf{F}^H \mathbf{D}_K^H(\theta_K) \mathbf{F} \mathbf{\Gamma}^H(\varepsilon_K) \end{bmatrix} \mathbf{y}.
$$

$$(A.1)$$

The product inside the Moore-Penrose pseudoinverse is $KL \times KL$, of which we need to find a way to simplify the computation. Consider the multiplication of two matrices, the product of $q_{i_1} \mathbf{B}^H \mathbf{F}^H \mathbf{D}_{i_1}^H(\theta_{i_1}) \mathbf{F} \mathbf{\Gamma}^H(\varepsilon_{i_1})$ and $q_{i_2} \mathbf{\Gamma}(\varepsilon_{i_2}) \mathbf{F}^H \mathbf{D}_{i_2}(\theta_{i_2}) \mathbf{F} \mathbf{B}$ is a nonzero matrix only when $q_{i_1} = q_{i_2} = 1$. Thus we only consider the case of $q_{i_1} = q_{i_2} = 1$ in the following.

- For $i_1 = i_2$ (corresponding to the diagonal blocks):

$$
q_{i_1} \mathbf{B}^H \mathbf{F}^H \mathbf{D}_{i_1}^H(\theta_{i_1}) \mathbf{F} \mathbf{\Gamma}^H(\varepsilon_{i_1}) q_{i_1} \mathbf{\Gamma}(\varepsilon_{i_1}) \mathbf{F}^H \mathbf{D}_{i_1}(\theta_{i_1}) \mathbf{F} \mathbf{B} = \mathbf{B}^H \mathbf{F}^H \mathbf{C} \mathbf{F} \mathbf{B}. \qquad (A.2)
$$

- For $i_1 \neq i_2$ (corresponding to the off-diagonal blocks):

$$
q_{i_1} \mathbf{B}^H \mathbf{F}^H \mathbf{D}_{i_1}^H(\theta_{i_1}) \mathbf{F} \mathbf{\Gamma}^H(\varepsilon_{i_1}) q_{i_2} \mathbf{\Gamma}(\varepsilon_{i_2}) \mathbf{F}^H \mathbf{D}_{i_2}(\theta_{i_2}) \mathbf{F} \mathbf{B}
$$
$$
= \mathbf{B}^H \mathbf{F}^H \mathbf{D}_{i_1}^H(\theta_{i_1}) \mathbf{F} \mathbf{\Gamma}^H(\varepsilon_{i_1}) \mathbf{\Gamma}(\varepsilon_{i_2}) \mathbf{F}^H \mathbf{D}_{i_2}(\theta_{i_2}) \mathbf{F} \mathbf{B}. \qquad (A.3)
$$

First, let us see the diagonal blocks' structure, which gives

$$
\mathbf{B}^H\mathbf{F}^H\mathbf{CFB} = \mathbf{B}^H\frac{1}{\sqrt{N}}
\begin{bmatrix}
\vdots & \omega_N^{-\phi\cdot 0} & \omega_N^{-(\phi+1)\cdot 0} & \cdots & \omega_N^{-(\phi+N_{ZC}-1)\cdot 0} & \vdots \\
\mathbf{0} & \omega_N^{-\phi\cdot 1} & \omega_N^{-(\phi+1)\cdot 1} & \cdots & \omega_N^{-(\phi+N_{ZC}-1)\cdot 1} & \mathbf{0} \\
\vdots & \vdots & \vdots & \cdots & \vdots & \vdots
\end{bmatrix}
$$

$$
\frac{1}{\sqrt{N}}
\begin{bmatrix}
\cdots & \mathbf{0} & \cdots \\
\omega_N^{\phi\cdot 0} & \omega_N^{\phi\cdot 1} & \cdots \\
\omega_N^{(\phi+1)\cdot 0} & \omega_N^{(\phi+1)\cdot 1} & \cdots \\
\vdots & \vdots & \vdots \\
\omega_N^{(\phi+N_{ZC}-1)\cdot 0} & \omega_N^{(\phi+N_{ZC}-1)\cdot 1} & \cdots \\
\cdots & \mathbf{0} & \cdots
\end{bmatrix}
\mathbf{B}
\tag{A.4}
$$

$$
= \mathbf{B}^H\frac{1}{N}
\begin{bmatrix}
\sum_{t=\phi}^{\phi+N_{ZC}-1}\omega_N^{t\cdot 0} & \sum_{t=\phi}^{\phi+N_{ZC}-1}\omega_N^{t\cdot 1} & \cdots \\
\sum_{t=\phi}^{\phi+N_{ZC}-1}\omega_N^{t\cdot -1} & \sum_{t=\phi}^{\phi+N_{ZC}-1}\omega_N^{t\cdot 0} & \cdots \\
\vdots & \vdots & \ddots
\end{bmatrix}
\mathbf{B}
$$

$$
= \frac{1}{N}
\begin{bmatrix}
\eta(0) & \eta(1) & \cdots & \eta(L-1) \\
\eta(-1) & \eta(0) & \cdots & \eta(L-2) \\
\vdots & \vdots & \ddots & \vdots \\
\eta(-(L-1)) & \eta(-L) & \cdots & \eta(0)
\end{bmatrix}
$$

where

$$
\eta(k) \triangleq \sum_{t=\phi}^{\phi+N_{ZC}-1}\omega_N^{t\cdot k} = \omega_N^{\phi+\frac{N_{ZC}-1}{2}}\frac{\sin\frac{N_{ZC}}{N}k\pi}{\sin\frac{1}{N}k\pi}.
\tag{A.5}
$$

We see that the diagonal blocks actually are very simple, where each term is the same η function evaluated at different argument vales.

Then we consider the off-diagonal blocks $\mathbf{B}^H\mathbf{F}^H\mathbf{D}_{i_1}^H(\theta_{i_1})\mathbf{F}\mathbf{\Gamma}^H(\varepsilon_{i_1})\mathbf{\Gamma}(\varepsilon_{i_2})\mathbf{F}^H\mathbf{D}_{i_2}(\theta_{i_2})\mathbf{FB}$. Focus on $\mathbf{F}\mathbf{\Gamma}^H(\varepsilon_{i_1})\mathbf{\Gamma}(\varepsilon_{i_2})\mathbf{F}^H$ first. Let $\breve{\varepsilon} = \varepsilon_{i_2} - \varepsilon_{i_1}$. Then

$$
\mathbf{\Gamma}^H(\varepsilon_{i_1})\mathbf{\Gamma}(\varepsilon_{i_2}) = \mathrm{diag}\left(\omega_N^{\breve{\varepsilon}\cdot 0}, \omega_N^{\breve{\varepsilon}\cdot 1}, ..., \omega_N^{\breve{\varepsilon}\cdot(N-1)}\right).
\tag{A.6}
$$

Define $\mathbf{A}_{c_1} \triangleq \mathbf{F}\mathbf{\Gamma}^H(\varepsilon_{i_1})\mathbf{\Gamma}(\varepsilon_{i_2})\mathbf{F}^H$. Then

$$
[\mathbf{A}_{c_1}]_{m,n} = \sum_{t=0}^{N-1}\frac{1}{N}\omega_N^{m\cdot t}\omega_N^{-\breve{\varepsilon}\cdot t}\omega_N^{-n\cdot t} = \sum_{t=0}^{N-1}\frac{1}{N}\omega_N^{(m-n-\breve{\varepsilon})\cdot t} = \sum_{t=0}^{N-1}\frac{1}{N}e^{j\frac{2\pi t(n-m+\breve{\varepsilon})}{N}}.
\tag{A.7}
$$

Now we extend to the product of $\mathbf{D}_{i_1}^H(\theta_{i_1})\mathbf{A}_{c_1}\mathbf{D}_{i_2}(\theta_{i_2})$. Assume $\mathbf{A}_{c_2} = \mathbf{D}_{i_1}^H(\theta_{i_1})\mathbf{A}_{c_1}\mathbf{D}_{i_2}(\theta_{i_2})$.

81

Then

$$
[\mathbf{A}_{c_2}]_{m,n} =
\begin{cases}
e^{j\frac{\pi u_{i_1}(m-\phi)(m-\phi+1)}{N_{ZC}}}e^{j\frac{-2\pi\theta_{i_1}m}{N}}\left(\sum_{t=0}^{N-1}\frac{1}{N}e^{j\frac{2\pi t(n-m+\bar{\varepsilon})}{N}}\right) & \\
e^{j\frac{2\pi\theta_{i_2}n}{N}}e^{j\frac{-\pi u_{i_2}(n-\phi)(n-\phi+1)}{N_{ZC}}}, & \text{for } \phi \le m, n \le \phi + N_{ZC} - 1, \\
0, & \text{otherwise.}
\end{cases}
$$

(A.8)

Focus on $\mathbf{F}^{H}\mathbf{A}_{c_2}\mathbf{F}$. Since it is a product of three full matrices, first let us see the product of the diagonal terms of $\mathbf{A}_{c_2}$ multiplied by the other two matrices, that is, the diagonal terms of $\mathbf{F}^{H}\mathbf{A}_{c_2}\mathbf{F}$. They can be expressed as
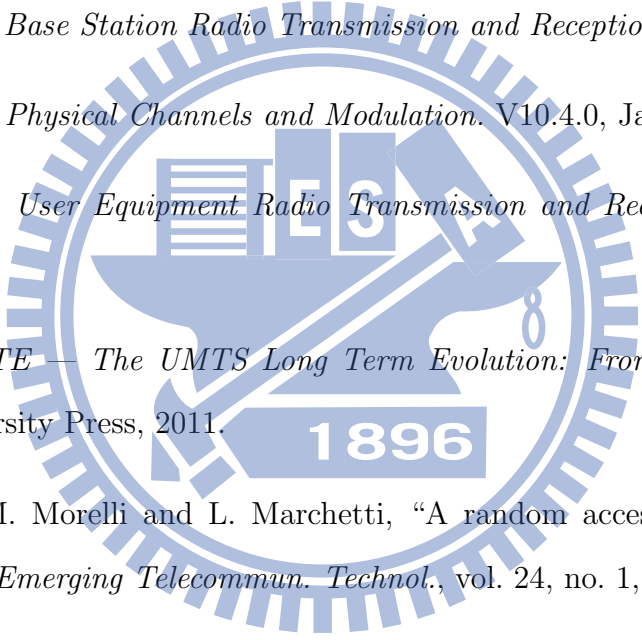
$$
[\mathbf{A}_{c_2}]_{m,m} =
\begin{cases}
e^{j\frac{-\pi(u_{i_2}-u_{i_1})(m-\phi)(m-\phi+1)}{N_{ZC}}}e^{j\frac{-2\pi(\theta_{i_2}-\theta_{i_1})m}{N}}\left(\sum_{t=0}^{N-1}\frac{1}{N}e^{j\frac{2\pi t(n-m+\bar{\varepsilon})}{N}}\right), & \text{for } \phi \le m \le \phi + N_{ZC} - 1, \\
0, & \text{otherwise.}
\end{cases}
$$

(A.9)

Then we have

$$
\left[\mathbf{F}^{H}\mathbf{A}_{c_2}\mathbf{F}\right]_{m+k,m} =
\begin{cases}
\sum_{m=\phi}^{\phi+N_{ZC}-1}e^{j\frac{-\pi(u_{i_2}-u_{i_1})(m-\phi)(m-\phi+1)}{N_{ZC}}}e^{j\frac{-2\pi(\theta_{i_2}-\theta_{i_1})m}{N}} & \\
\left(\sum_{t=0}^{N-1}\omega_N^{(m-n-\varepsilon)\cdot t}\right)e^{-j\frac{2\pi mk}{N}}, & \text{for } \phi \le m, n \le \phi + N_{ZC} - 1, \\
0, & \text{otherwise.}
\end{cases}
$$

(A.10)

We can interpret the last equation as DFT of $e^{j\frac{-\pi(u_{i_2}-u_{i_1})(m-\phi)(m-\phi+1)}{N_{ZC}}}e^{j\frac{-2\pi(\theta_{i_2}-\theta_{i_1})m}{N}}$ $\left(\sum_{t=0}^{N-1}\omega_N^{(m-n-\varepsilon)\cdot t}\right)$. Because of the m^2 term in the exponent, the DFT operation becomes troublesome. It appears that there might be a closed-form expression for the DFT of a finite chirp [10]. In fact, this is not true, and the terms inside the DFT operation are not in the form of a finite chirp. Even when we only consider the product of the diagonal terms of $\mathbf{A}_{c_2}$ multiplied by the other two matrices, it still takes a lot of computation. Therefore, we give up solving the multiple hypothesis testing this way.

Bibliography

[1] Farooq Khan, *LTE for 4G Mobile Broadband: Air Interface Technologies and Performance.* Cambridge University Press, 2009.

[2] 3GPP TS 36.104, *Base Station Radio Transmission and Reception.* V10.4.0, Jan. 2012.

[3] 3GPP TS 36.211, *Physical Channels and Modulation.* V10.4.0, Jan. 2012.

[4] 3GPP TS 36.101, *User Equipment Radio Transmission and Reception.* V10.4.0, Jan. 2012.

[5] Stefania Sesia, *LTE — The UMTS Long Term Evolution: From Theory to Practice.* Cambridge University Press, 2011.

[6] L. Sanguinetti, M. Morelli and L. Marchetti, "A random access algorithm for LTE systems," *Trans. Emerging Telecommun. Technol.*, vol. 24, no. 1, pp. 49–58, Jan. 2013.

[7] P. Wang, K. Lu, D. Lin, and P. Ting, "Quasi-maximum likelihood initial downlink synchrnoization for IEEE 802.16m," *in Int. Workshop Signal Proc. Adv. Wireless Comm.*, June 2011, pp. 521–525.

[8] V. Erceg *et al.*, "Channel models for fixed wireless applications," IEEE 802.16.3c-01/29r4, July 2001.

[9] 3GPP TS 36.141, *Base Station Conformance Testing.* V10.4.0, Jan. 2012.

[10] A. Brodzik, "On the Fourier transform of finite chirps," *IEEE Signal Processing Lett.*, vol 13, no 9, pp. 541–544, Sep. 2006.

[11] Rohde&Schewarz, *LTE Base Station Performance Tests According to TS 36.141 Application Note*, July 2010.

[12] L. Sanguinetti, and M. Morelli, "An initial ranging scheme for the IEEE 802.16 OFDMA uplink," *IEEE Trans. Wireless Commun.*, vol. 11, no. 9, pp. 3204–3215, Sep. 2012.

[13] A. Freire-Irigoyen, R. Torrea-Duran, S. Pollin, Li Min, E. Lopez, and L. Van der Perre, "Energy efficient PRACH detector algorithm in SDR for LTE femtocells," in *18th IEEE Symposium on Communications and Vehicular Technology*, Bebelux, Nov. 2011, pp. 1–5.

[14] Hsiao-Ying Chan,"Study in initial ranging for IEEE 802.16m" M.S. thesis, Department of Electronics Engineering and Institute of Electronics, National Chiao Tung University, Hsinchu, Taiwan, R.O.C., Nov. 2011.

[15] http://en.wikipedia.org/wiki/3GPP Long Term Evolution